UNIVERSITY OF CALIFORNIA, SAN DIEGO

Non-Foster Circuit Loaded Periodic Structures for Broadband Fast and Slow Wave Propagation

A Dissertation submitted in partial satisfaction of the
requirements for the degree
Doctor of Philosophy

in

Electrical Engineering (Electronic Circuits and Systems)

by

Jiang Long

Committee in charge:

    Professor Daniel F. Sievenpiper, Chair
    Professor James F. Buckwalter
    Professor Gert Cauwenberghs
    Professor Eric E. Fullerton
    Professor Vitaliy Lomakin

2015

The Dissertation of Jiang Long is approved, and it is acceptable in quality and form for publication on microfilm and electronically:

_____

_____

_____

_____
Chair

University of California, San Diego

2015

DEDICATION

To my parents Mr. Ningsheng Long, Ms. Yiwei Sun,

and my beloved wife Lan Liu.

TABLE OF CONTENTS

LIST OF FIGURES

viii

LIST OF TABLES

LIST OF ABBREVIATIONS

AMC	Artificial magnetic conductor
BJT	Bipolar junction transistor
CRLH	Composite right and left handed
EM	Electromagnetic
ESA	Electrically small antenna
FBW	fractional bandwidth
HIS	High impedance surface
MLine	Microstrip line
MTM	Metamaterial
MTS	Metasurface
NIC	Negative impedance converter
OCS	Open circuit stable
Op-amp	Operational amplifier
PCB	Printed circuit board
RCS	Radar cross section
RF	Radio frequency
SCS	Short circuit stable
SRR	Split ring resonator
TEM	Transverse electromagnetic
TL	Transmission line
TM	Transverse magnetic
UHF	Ultra high frequency

ACKNOWLEDGEMENTS

First and foremost, I would like to thank my advisor, Prof. Daniel Sievenpiper, for his excellent and constant guidance and support throughout my research and graduate study. As a pioneer in the fields of metamaterials and metasurfaces, he is focused not only on the current hot topic, but is always looking to the future. This has enlightened me about the nature of research and has guided me on my journey through challenging works. I would not have achieved as much progress as I have without his persistent encouragements and professional advices.

Next, I would like to express my sincere appreciation to my dissertation committee members, Prof. James Buckwalter, Prof. Gert Cauwenberghs, Prof. Eric. Fullerton, and Prof. Vitaliy Lomakin, for their valuable comments and suggestions.

I have been doing research for the Applied Electromagnetics (AEM) Group for five years, and most ideas and solutions are consolidated in group meetings and through numerous discussions. Therefore, I must thank all the AEM group students, post docs, and visiting scholars for sharing their knowledge with me and for participating in discussions and collaboration.

My five-year PhD life has also introduced me to many friends: Jun Li, Dongjin Song, Yu Xiang, Yuncong Chen, Enming Luo. I cannot list all of them, but their help and our friendships will stay in my heart forever. The PhD life would have been unfulfilling without them.

Nothing can truly express my deepest heartfelt gratitude for my parents—Ms. Yi-wei Sun and Mr. Ningsheng Long—and the 30 years they have cared for me with selfless love. I also want to show my biggest gratitude to my wife, Dr. Lan Liu. We have experienced PhD study together, which has been full of challenges. I cannot imagine the life

without her company and encouragements. I am happy she has received her PhD degree and is fulfilling her dream, and I am sure she will be just as happy for me.

The material in this dissertation is based on the following papers which are either published, or submitted for publication. In Chapter 2, the circuit design example in Sec. 2.4 is based on part of the published paper: J. Long, M. Jacob, D. Sievenpiper, "Broadband Fast-Wave Propagation in a Non-Foster Circuit Loaded Waveguide," *IEEE Trans. Microw. Theory Techn.*, vol. 62, pp. 789-798, 2014. Chapter 3 is based on the reprint of the published papers: J. Long, M. Jacob, D. Sievenpiper, "Broadband Fast-Wave Propagation in a Non-Foster Circuit Loaded Waveguide," *IEEE Trans. Microw. Theory Techn.*, vol. 62, pp. 789-798, 2014; J. Long, D. Sievenpiper, "Stable multiple non-Foster circuits loaded waveguide for broadband non-dispersive fast-wave propagation," *Electronics Lett.*, pp. 1708-1710, 2014. Chapter 4 is based on the material that is to be submitted: J. Long, D. Sievenpiper, "The Observation of Dispersionless Superluminal Propagation and its Limitation in a Non-Foster Loaded Waveguide," in preparation for submission. Chapter 5 is based on the submitted and published papers: J. Long, and D. Sievenpiper, "Low-profile and Low-dispersion Artificial Impedance Surface in the UHF Band Based on Non-Foster Circuit Loading," submitted to *IEEE Trans. Antenna Propag.*; J. Long, and D. Sievenpiper, "Dispersion-reduced high impedance surface loaded with non-Foster impedances," in *Proc. IEEE Antennas Propag. Soc. Int. Symp. (APSURSI)*, Vancouver, Canada, 2015.

The dissertation author was the primary author of the work in these chapters, and co-authors have approved the use of the material for this dissertation.

Jiang Long

La Jolla, CA

December, 2015

VITA

2003-2007	B. S. in Electrical Engineering (Electronic and Information Engineering), Zhejiang University, China
2007-2010	M. S. in Electrical Engineering (Electronics Science and Technology), Zhejiang University, China
2007	Ph. D. in Electrical Engineering (Electronic Circuits Systems), University of California, San Diego

PUBLICATIONS

Journal Articles

J. Long, D. Sievenpiper, "Low-profile and Low-dispersion Artificial Impedance Surface in the UHF Band Based on Non-Foster Circuit Loading", submitted to *IEEE Trans. Antenna Propag.*

J. Long, D. Sievenpiper, "The Observation of Dispersionless Superluminal Propagation and its Limitation in a Non-Foster Loaded Waveguide", in preparation.

Z. Luo, X. Chen, **J. Long**, R. Quarfoth, D. Sievenpiper, "Self-focusing of electromagnetic surface waves on a nonlinear impedance surface", *Appl. Phys. Lett.*, vol. 106, 21102, 2015.

Z. Luo, X. Chen, **J. Long**, R. Quarfoth, D, Sievenpiper, "Nonlinear Power-Dependent Impedance Surface," *IEEE Trans. Antenna Propag.*, vol. 63, pp. 1736-1745, 2015.

J. Long, M. Jacob, D. Sievenpiper, "Broadband Fast-Wave Propagation in a Non-Foster Circuit Loaded Waveguide," *IEEE Trans. Microw. Theory Techn.*, vol. 62, pp. 789-798, 2014.

J. Long, D. Sievenpiper, "A Compact Broadband Dual Polarized Patch Antenna for Satellite Communication/Navigation Applications," *IEEE Antenna Wireless Propag. Lett.*, vol. 14, pp. 273-276, 2014.

J. Long, D. Sievenpiper, "Stable multiple non-Foster circuits loaded waveguide for broadband non-dispersive fast-wave propagation," *Electronics Lett.*, pp. 1708-1710, 2014.

M. Jacob, **J. Long**, D. Sievenpiper, "Non-Foster Loaded Parasitic Array for Broadband Steerable Patterns," *IEEE Trans. Antenna Propag.*, vol. 62, pp. 6081-6090, 2014.

F. Gao, F. Zhang, **J. Long**, M. Jacob, D. Sievenpiper, "Non-dispersive tunable reflection phase shifter based on non-Foster circuits," *Electronics Lett.*, pp. 1616-1618, 2014.

D. Sievenpiper, D. Dawson, M. Jacob, T. Kanar, S. Kim, **J. Long**, R. Quarfoth, "Experimental Validation of Performance Limits and Design Guidelines for Small Antennas," *IEEE Trans. Antennas Propag.*, vol. 60, pp. 8-19, 2012.

Conference papers

J. Long, D. Sievenpiper, "Dispersion-Reduced High Impedance Surface Loaded with Non-Foster Impedances," in *Proc. IEEE Int. Symp. Antennas Propag. Soc. (APSURSI)*, Vancouver, Canada, 2015

M. Jacob, **J. Long**, D. Sievenpiper, "Nonlinear Effects of Non-Foster Matching Networks," in *Proc. IEEE Int. Symp. Antennas Propag. Soc. (APSURSI)*, Vancouver, Canada, 2015

J. Long, D. Sievenpiper, "Negative Capacitor and Its Applications in RF/Microwave Circuits and Antennas," in *Int. symp. on advanced applied electromagnetic research at Nagoya Institute of Technology*, Nagoya, Japan, Sept. 18, 2014. (**Invited**)

J. Long, J. Rushton and D. Sievenpiper, "Radial Waveguide Model for Permittivity Measurements of Disk-Shaped Dielectric Samples at RF Frequencies," in *Proc. IEEE Int. Symp. Antennas Propag. Soc. (APSURSI)*, Orlando, FL, 2013.

M. Jacob, **J. Long**, D. Sievenpiper, "Noise in Non-Foster Antenna Matching Circuits," in *Proc. IEEE Int. Symp. Antennas Propag. Soc. (APSURSI)*, Orlando, FL, 2013.

J. Long, M. Jacob, D. Sievenpiper, "Electronically Steerable Antenna Using Superluminal Waveguide and Tunable Negative Capacitors," in *Proc. IEEE Int. Symp. Antennas Propag. Soc. (APSURSI)*, Chicago, IL, 2012.

M. Jacob, **J. Long**, D. Sievenpiper, "Broadband non-Foster matching of an electrically small loop antenna," in *Proc. IEEE Int. Symp. Antennas Propag. Soc. (APSURSI)*, Chicago, IL, 2012.

D. Sievenpiper, M. Jacob, **J. Long**, "Active electromagnetic structures, metamaterials, and antennas," in *Int. Workshop on Antenna Technology (iWAT)*, Tucson, AZ, 2012.

ABSTRACT OF THE DISSERTATION

Non-Foster Circuit Loaded Periodic Structures for Broadband Fast and Slow Wave Propagation

by

Jiang Long

Doctor of Philosophy in Electrical Engineering (Electronic Circuits and Systems)

University of California, San Diego, 2015

Professor Daniel F. Sievenpiper, Chair

Periodic structure has been extensively applied in many applications, such as wireless communication, sensing, and advanced applied electromagnetics such as invisible cloaking and superlens. However, as broadband systems have rapidly advanced, the bandwidth of the periodic structure has become a bottleneck. In particular, the high dispersion of the periodic structure prevents it from being applied to future wide-band practical applications. Extensive research efforts have been done on the bandwidth problem of the periodic structure, and these have concluded that there is a fundamental bandwidth limitation for passive electromagnetic structures. Nevertheless, great interest still remains in

finding alternative solutions to increase the bandwidth of the periodic structures.

All conventional periodic structures are based on a repeatedly patterned passive metallic structure, which can be characterized as passive impedance that follows the Foster's theorem, resulting in a fundamental bandwidth limitation. In contrast, an active periodic structure is composed of unit cells that violate Foster's theorem. Thus, they are potentially capable of breaking the bandwidth limitation.

This thesis studies the non-Foster impedance loaded periodic structures and their broadband electromagnetic fast and slow wave propagation applications. To be more specific, a non-Foster impedance, realized by an active feedback circuit, is applied to the unit cell of the periodic structures in order to increase the bandwidth of the unit cell and eventually broaden the bandwidth of the periodic structures.

The thesis first introduces the fundamental principle of the non-Foster impedance, explains its difference to the passive impedance, and presents its possible active circuit implementation: a negative impedance converter based non-Foster circuit, which covers the derivation of the non-Foster input impedance, its stability, and a design example. Then, the thesis presents broadband fast and slow wave propagation based on the non-Foster impedance loaded periodic structures. For fast wave propagation, a periodically non-Foster impedance loaded waveguide is designed, fabricated, measured, and demonstrated for broadband dispersion-reduced fast wave propagation. The non-Foster fast wave propagation study extends to the observation of the dispersionless superluminal pulse transmission, and a fundamental limitation of a periodic non-Foster loading-based waveguide. On the other hand, this thesis also presents an extremely low-profile slow wave supported electromagnetic surface structure by loading non-Foster impedance to a conventional artificial impedance surface. All the applications presented in the thesis include the principle of

loading non-Foster impedance to the conventional passive periodic electromagnetic structures, the design of the non-Foster impedance circuits, and the broadband measurement demonstration.

Chapter 1

Introduction

Electromagnetic (EM) wave propagation has been extensively studied and widely applied to many applications that are essential to human life, improving our productivity and expanding the scope of human activities. For instance, wireless communication greatly shortens the distance between individuals, globally connecting human societies together. Wireless sensing not only extends our activity macroscopically to deep space, allowing us the ability of learning what happened thousands of light years away from the earth, but also leads us to the observation and manipulation of the microscopic world, enabling people to control objects on a sub-nanometer scale. In most general cases, EM waves are propagating in naturally existing media, and wave propagation in such media is normal and can be well controlled. However, special types of wave propagation are still desired, such as superluminal propagation for invisibility cloaking and negative refractive index propagation for superlenses, yet no natural material can support them. Therefore, artificial materials, or "metamaterials", have been invented to achieve such special propagation, and most metamaterials are designed with periodic structure, which is the main topic of this thesis.

1.1 Periodic Structure, Fast and Slow Wave Propagation

A periodic structure, as its name implies, is composed of periodically arrayed unit cells that share a similar pattern [1–3], as shown in Fig. 1.1. Microscopically, the unit cells are arranged in a specific format, and infinitely extend to three dimensions. When the size of the unit cell is small enough (usually no more than one tenth of the wavelength), it can be macroscopically regarded as a homogeneous material whose EM properties are strongly dependent on the characteristics of the unit cell and the periodicity [1–4].
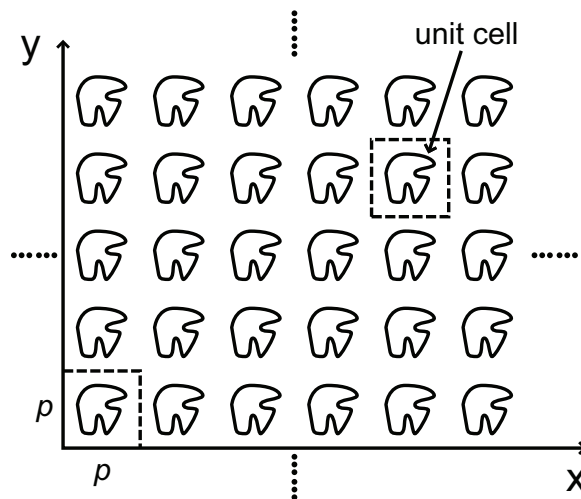
Figure 1.1: An illustration of the 2D periodic medium. It has periods along the x- and y-axes. The pattern is arbitrary. The unit cell is not necessarily a square, but must repeats in a certain formation.

There is a long history of study on the periodic structures. Before the 1990s, studies of periodic structures focused on one-dimensional (1D) structures in both microwave and optical engineering, such as dielectric gratings for beam splitting, linear accelerators, slot arrays, phase-array antennas, couplers, and so forth [5]. The first research on photonic crystal was published in 1987 [6, 7], inducing considerable research on two-dimensional (2D) and three-dimensional (3D) periodic structures. It should be noted that despite the name "photonic crystal" a lot of studies and applications have been done in the microwave

realm, because the photonic crystal represents a 2D or 3D periodic structure that mimics natural crystals, but its application is not restricted to the optical field. Around the year 2000, metamaterials (MTM) were proposed to develop artificial materials having negative permittivity, ε, and/or negative permeability, μ, by using resonant electronics as the unit cells of the periodic structures [8, 9]. The emergence of MTMs led to many applications including already established applications such as waveguides, couplers, and antennas, as well as new technologies like invisible cloaks and superlenses [10, 11]. In addition, another type of MTM, a low-profile MTM, as metasurface (MTS), also got a lot of attention as it is much thinner than a bulky MTM, and therefore more favorable for practical manufacture and fabrication [12]. Based on MTS, the theory of high impedance surface (HIS) [13] has been developed and applied to antenna prefect magnetic conductor ground planes [14] and microwave absorbers [15]. MTMs and MTSs have been developed as a very broad research area spanning optics and microwave fields.

The periodic EM structure has been extensively studied over many decades. The basic principle is that the EM waves interact with all the individual unit cells, which induces multiple reflection/diffraction and leads to the alteration in the wave propagation compared to the wave propagation in the homogenous medium [2, 3]. The wave propagation in the periodic structure can be analyzed by enforcing the Floquet theory to the solutions of the Maxwell equations [16, 17]. As a result, the wave propagation constant, k, is frequency dependent, and bandgaps also appear at some frequencies. The phase velocity and the propagation constant are related with

$$v_p = \frac{\omega}{k},$$

(1.1)

so the wave propagation can be categorized by comparing the phase velocity to the speed

of light c, with fast waves having $v_p > c$, and slow waves having $v_p < c$ [1, 18]. Gener-

ally speaking, a periodic structure presents fast wave and slow wave at different frequency

ranges. As an example, the dispersion diagram of a 2D center-shorted-patch periodic struc-

ture is shown in Fig. 1.2, which illustrates that k is frequency dependent [13]. Bandgap is

another characteristic of periodic structures, which is also illustrated in Fig. 1.2. Therefore,

three points can be observed: (1) the propagation is dispersive; (2) there is a bandgap; and

(3) part of the dispersion curve is under the light line, indicating slow wave propagation,

and another part of the curve is above the light line, representing fast wave propagation.
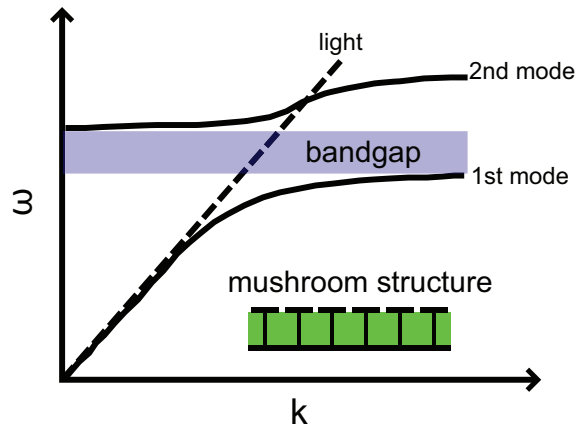
Figure 1.2: Typical dispersion diagram for a periodic structure. The dispersion diagram is based on the center-shorted-patch HIS structure. The first and second mode are plotted, along with a band gap. The dashed curve represents the wave propagation in vacuum.

Identifying the propagation constant or phase velocity is essential for controlling the

wave propagation, especially at the interface of the dielectric material and the air. Figs. 1.3

illustrate both fast and slow wave propagation at the interface of the grounded dielectric

slab waveguide and the air. Based on the phase matching condition [16, 19], the wave is

bounded at the interface during slow wave propagation, whereas it gradually leaks away

from the interface in the case of fast wave propagation. Figs. 1.4 show how and where

the fast and slow wave can be applied. As shown in Figs. 1.4(a) and (b), the slow wave

propagation at the surface can be related to the surface wave coupling of the patch antenna, which can potentially decrease the antenna efficiency and multiple antenna isolation [20]. It is also associated with the radar cross section (RCS) by controlling the surface currents. On the other hand, manipulating the fast wave propagation matters for controlling the beam direction of the leaky wave antennas [21, 22], and for invisible cloaking technology [11], as illustrated in Figs. 1.4(c) and (d).
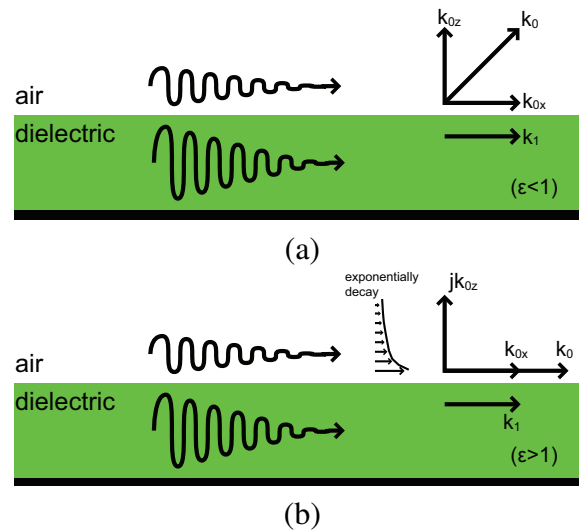
Figure 1.3: Slow and fast wave at the air–dielectric interface. (a) presents the fast wave at the air–dielectric interface. A leaky wave mode surface wave is produced based on phase matching condition. (b) illustrates a slow surface wave propagating along the surface and exponentially decaying away from the surface.

For realizing fast and slow wave propagation, a periodic structure is one good approach. Generally, a MTM must be properly designed to accomplish the desired phase velocity so that wave propagation is controlled. 2D MTM with a split-ring resonator (SRR) has shown the negative refractive index and many associated applications [8]. Composite right- and left- handed (CRLH) transmission lines (TLs) can be easily configured in fast wave regions for leaky wave antennas, as well as in slow wave regions for miniaturizing the slow wave structure [4]. By tuning the unit cell size of HIS, it can also be used as
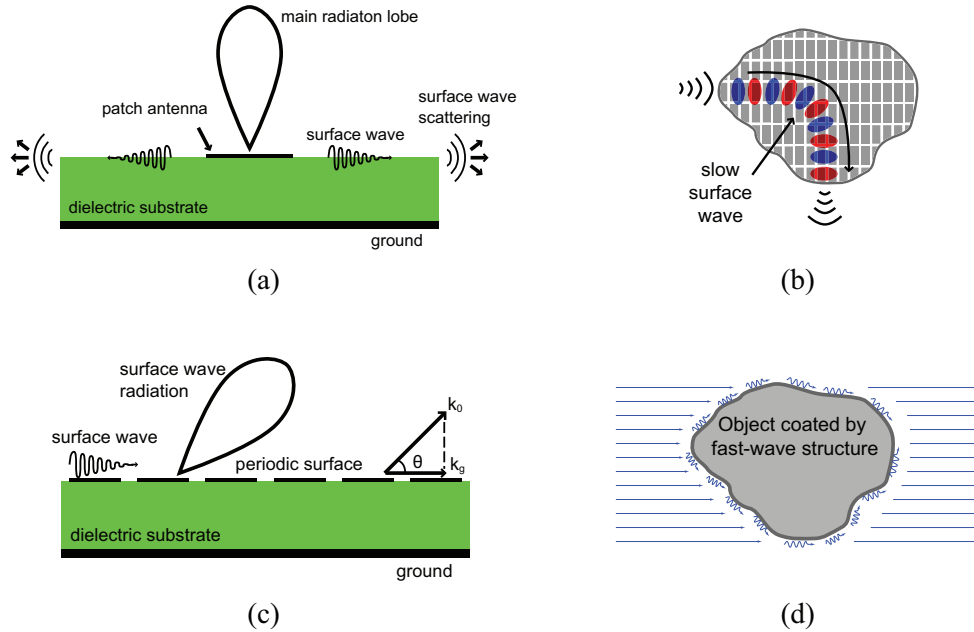
Figure 1.4: Slow and fast surface wave applications. (a) A slow surface wave causes decreased antenna efficiency and unwanted side lobes. (b) A slow surface wave can be manipulated to control the scattering direction. (c) A fast surface wave is explored as a leaky wave antenna. (d) A fast wave structure can be used in a thin invisibility cloak.

a fast wave structure for antenna applications and a slow wave structure as surface wave waveguide [13, 23].

1.2 Motivation

Although periodic structures can be used for fast and slow wave propagation, they suffer from the dispersion problem, limiting the operational bandwidth. This is because the unit cells of MTMs and MTSs are usually resonant structures, working near their resonant frequencies to achieve large reactance values that are hard to accomplish in limited size without the presence of the metallic structure [24]. As an example, Fig. 1.5 presents the shorted-patch-based impedance surface structure and its lumped circuit equivalence, which is clearly a resonant circuit [13]. Nevertheless, because of the inclusion of this resonant

structure, each unit cell is highly frequency dependent, leading to significant dispersion of the macroscopic periodic structure. Therefore, the fast or slow wave achieved by the periodic structure usually has significant dispersion, limiting its available bandwidth.

Figure 1.5: The unit cell of a periodic structure is usually a resonant circuit. The shorted-patch-based impedance surface unit cell is used here as an example. At resonance, the charges are collected in the adjacent patches in the gap. The path from one patch to another through the vias constitutes the current path, forming an inductor.

It is impossible to mitigate the dispersion by reducing the periodic structure, since this is the only way to build an artificial material. Modifying the resonant unit cell is the only possible method for reduce the dispersion. Nevertheless, conventional approaches such as multi-resonant unit cell do not work, because the resonance is still achieved by passive structure, which are restricted by Bode–Fano Limit [25]. Therefore, the only possible solution is to use a new kind of circuit electronic components — non-Foster electronics.

1.3   Non-Foster Impedance

All passive electronics follow the Foster's theorem [26], which states that electronic reactance monotonically increases with frequency (the reactance approaches positive infinity at poles and continues from negative infinity). This fundamentally prevents the achievable impedance from following any arbitrary function of frequency, which is why there is Bode–Fano limit in matching bandwidth limitation [25], and Wheeler–Chu limit in electrically small antenna (ESA) bandwidth [27]. By contrast, non-Foster impedance, by defini-

tion, is a kind of impedance that does not follow Foster's theorem. It thus does not exist in nature, but it can be realized by electronic circuits, particularly by active electronic circuits with positive feedback. Non-Foster impedance has a property that no passive impedance possesses — the negative slope of the reactance curve versus frequency. Consider a regular capacitor: the capacitance is positive, leading to the positive slope of the reactance curve versus frequency. In contract, a negative capacitor, as a typical non-Foster electronic impedance, with the same reactance capacitance relation but negative capacitance value, has a negative reactance-frequency slope relation. Due to this unique characteristic, an electronics system with a non-Foster circuit does not have bandwidth limitations as all other passive circuit systems do. Therefore, it is promising for reducing the dispersion in MTM and MTS. Non-Foster impedance can be realized by active circuit, particularly negative impedance converter (NIC) circuit, which will be reviewed in detail in Chapter. 2.

1.4   Scope of This Thesis

This thesis presents the non-Foster circuit loaded periodic structure and its application for broadband dispersion reduced fast and slow wave propagation.

Chapter 1 is the overview of the periodic structure, the motivation, and a brief introduction on the non-Foster impedance.

Chapter 2 discusses the non-Foster impedance and its implementation based on the NIC circuits, including the basic background of the non-Foster circuit, its broadband applications, the derivation of non-Foster input impedance, and a design example.

Chapter 3 presents the periodic non-Foster circuit loaded waveguide for broadband dispersion reduced fast wave propagation. A waveguide periodically loaded with negative capacitors can realize broadband fast wave propagation, which is demonstrated by

retrieving the propagation constant from the measured frequency response of the fabricated waveguide, and confirmed by measuring the near field. The stability of the non-Foster waveguide is also discussed.

Chapter 4 extends the research on the non-Foster loaded fast wave waveguide. Superluminal pulse propagation with negligible distortion is experimentally observed in the proposed non-Foster loaded waveguide. A theoretical limitation on superluminal pulse transmission for the non-Foster loaded waveguide is discussed. Under a negligible distortion condition, the superluminal pusle width is related to the transmission distance, indicating that superluminal events are impossible and demonstrating the consistency with relativity and causality.

In Chapter 5, the non-Foster impedance loaded aritificial impedance surface is presented for low-profile and low-dispersion slow surface wave propagation at ultra-high frequency (UHF). With loading non-Foster impedance, the thickness of the UHF impedance surface is significantly reduced. It is demonstrated by the near field measurement that the velocity of slow surface wave propagation is constant over a wider bandwidth compared to the HIS loaded with passive impedance.

Chapter 6 summarizes the thesis and discusses about the future work.

Chapter 2

Non-Foster Impedance

In contrast to passive electronic components, the non-Foster impedance has a negative reactance slope versus frequency, which makes it promising in broadband matching. This chapter reviews the basic principles of the non-Foster circuit, including its fundamental difference from the conventional impedance and its broadband application. A literature review on non-Foster circuit applications is also presented, followed by the theoretical design principle of the non-Foster circuit. A non-Foster circuit design example is presented.

2.1 Overview of Non-Foster Impedance

Any naturally existing impedance follows Foster's reactance theorem, which states that the reactance of a passive, lossless two-terminal (single-port) network, always strictly monotonically increases with frequency. This can be easily seen from an individual inductor or capacitor, and can be proven for any combination of inductors and capacitors, which was first demonstrated in 1924 by Ronald Martin Foster [26]. It can also be extended as a general rule for any arbitrary passive impedance network, by restricting all poles and

zeroes alternate with frequency and are located on the left-hand side of the complex frequency domain. Foster's theorem fundamentally defines the passive and causal behavior of impedance over frequency, from which the bandwidth lamination for the reactive matching network [25] and Wheeler–Chu limit for ESA [27] are further demonstrated. It should be noted that Foster's reactance theorem only works for passive network.

For an active network, poles and zeroes may move to the right side owing to the involvement of the active components that provide gains to the network. Therefore, it may generate some impedance that does not follow Foster's theorem. Due to its violation of Foster's theorem, such impedance is called non-Foster impedance.
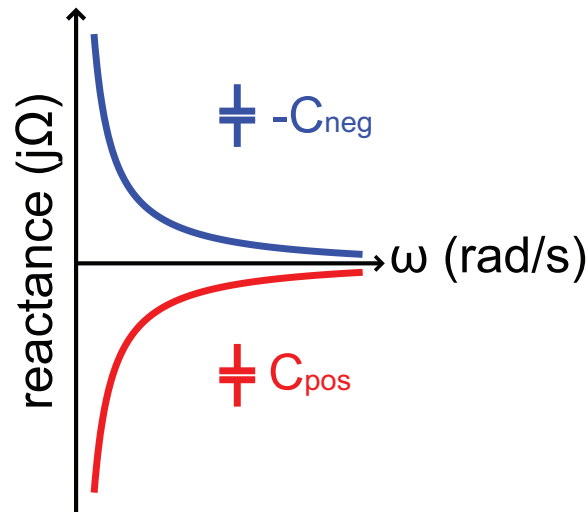
Figure 2.1: A comparison of negative and ordinary capacitors. The red curve is the reactance of the positive capacitor, and the blue one is associated with the negative capacitor.

The most straightforward non-Foster component is a negative capacitor and negative inductor. The reactance of a negative capacitor, $-C_{neg}$ (with the C_{neg} representing the magnitude of the negative capacitor), is compared to that of the positive capacitor, C_{pos}, in Fig. 2.1. Because

$$X_{cneg}(\omega) = j\frac{1}{\omega C_{neg}},$$

(2.1)

it is easy to derive the slope of the reactance as

$$\frac{dX_{cneg}}{d\omega} = -j\frac{1}{\omega^2 C_{neg}} < 0. \tag{2.2}$$

Therefore, the sign of the slope is determined by the sign of the capacitor. For a negative capacitor, $-C_{neg}$, with $C_{neg} > 0$, the slope is always negative. In contrast, the reactance of the positive capacitor monotonically increases with frequency. According to Foster's theorem, it is clear that a negative capacitor is categorized as non-Foster impedance, judging by the slope of the reactance curve. Actually, this unique non-Foster characteristic will be utilized for broadband application, which will be discussed in the following section.

Non-Foster impedance property is also reflected on a Smith chart. Since the non-Foster impedance has a negative reactance slope versus frequency, it can be demonstrated that the loci of the non-Foster impedance rotate counter-clockwise, whereas the Foster impedance has loci with clockwise rotation over the frequency. The demonstration is derived as follows:

The reflection coefficient is expressed as

$$\Gamma = \frac{1 - jx_{NF}}{1 + jx_{NF}}, \tag{2.3}$$

where x_{NF} is the normalized reactance of the non-Foster impedance. It is thus easy to derive its complex angle, as

$$\angle\Gamma = -2\arctan x_{NF}. \tag{2.4}$$

Since the derivative of the non-Foster impedance is negative, as

$$\frac{dx_{NF}}{d\omega} < 0, \tag{2.5}$$

It is thus derived that

$$\frac{d\angle\Gamma}{d\omega} = -2\frac{1}{1+x_{NF}^2}\frac{dx_{NF}}{d\omega} > 0, \qquad (2.6)$$

indicating the loci on the Smith chart move counter-clockwise. This anti-clockwise movement of the loci is utilized for broadband phase shifter, which will be discussed later in this chapter.

In summary, the differences between non-Foster impedance and Foster impedance are listed in Table 2.1. They are: (1) Although the sign of the reactance depends on the property of the electronic components (capacitor or inductor), the reactance of non-Foster impedance is always opposite its Foster counterpart. (2) The slope of non-Foster impedance is always negative, whereas the Foster impedance has positive slope. (3) When mapping the reactance on Smith chart, the loci of non-Foster impedance move in a counter-clockwise direction, indicating the reflection phase is increasing with frequency, whereas the Foster impedance reflection phase decreases with frequency.

Table 2.1: Summary of the comparison of the non-Foster and passive impedance

	Foster impedance	Non-Foster impedance
Sign of reactance		opposite of Foster impedance
Slope of reactance	> 0	< 0
Loci direction on Smith chart	clockwise	counter-clockwise

2.2 Non-Foster Matching to Passive Impedance

It is those unique differences that make the non-Foster impedance capable of doing what the Foster impedance can never achieve. One of these potentially useful applications

is the use of non-Foster impedance to match a conventional impedance.

Impedance matching is important for radio frequency (RF) and microwave circuits and systems. A matched impedance is capable of transmitting or receiving power with maximum efficiency. Therefore, impedance matching is desired for all the network nodes where the maximum power transmission is of interest [28].
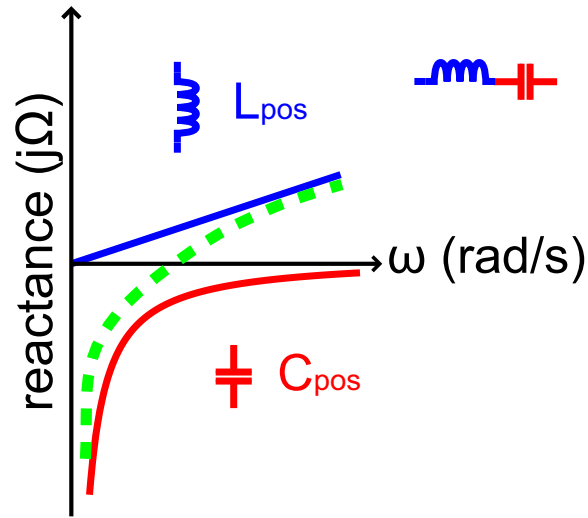
Figure 2.2: Conventional impedance matching. A capacitor (red) is matched with an inductor (blue). Zero reactance is only achieved at one frequency. The net reactance slope (dashed green curve) is still positive.

A matching condition requires the load impedance is conjugated to achieve zero net reactance. To put it in another way, the reactance in the network must be canceled. Fig. 2.2 illustrates how an inductor, L_{pos}, is used to compensate for the reactance of a capacitor, C_{pos}. In fact, the reactance of the inductor and that of the capacitor have different signs. Consequently, the series combination of the two components leads to zero reactance, as the resonance of a series LC circuit. It is easy to calculate the resonant frequency, which is

$$\omega_0 = \frac{1}{\sqrt{L_{pos}C_{pos}}}.$$

(2.7)

However, it is also easy to find that the net frequency reactance is

$$X_{LC}(\omega) = \omega L_{pos} - \frac{1}{\omega C_{pos}}, \tag{2.8}$$

which is zero only at the resonant frequency. At all other frequencies, the reactance is either positive or negative, deviating from zero. The further away from the resonant frequency, the more deviation there will be. This is because that the net reactance monotonically increases with frequency, as do the individual inductor and capacitor, which can be seen from the derivative of the reactance

$$\frac{dX_{LC}}{d\omega} = L_{pos} + \frac{1}{\omega^2 C_{pos}} > 0. \tag{2.9}$$

In addition, the slope is larger than either the individual inductor or the single capacitor. Therefore, perfect cancellation is only achieved at one frequency; consequently, a cancellation bandwidth exists, further relating to the quality factor, Q, and the matching bandwidth.

By contrast, significant bandwidth benefit can be obtained if non-Foster impedance is used to compensate for a Foster impedance. For example, if a negative capacitor, $-C_{neg}$, is employed to cancel the same positive capacitor, C_{pos}, and provided that

$$C_{neg} = C_{pos}, \tag{2.10}$$

the resulted net reactance is

$$X_{NFmatching}(\omega) = 0, \tag{2.11}$$

which applies for all frequencies, shown in Fig. 2.3. Apparently, larger bandwidth is accomplished.
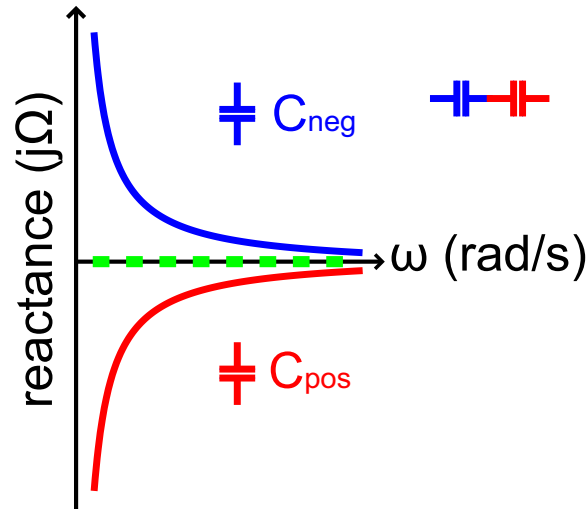
Figure 2.3: Non-Foster matching a capacitor (red) with a negative capacitor (blue). The net reactance (dashed green curve) slope is reduced. When $C_{neg} = C_{pos}$, the net reactance has zero slope, and zero reactance is achieved at all frequencies.

The increase in matching bandwidth results from the negative slope of the non-Foster reactance compensating for the positive slope of the Foster impedance. Once C_{neg} equals C_{pos}, the negative and positive slope are exactly the same and therefore cancel each other, resulting in perfect compensation for all frequencies, or infinite bandwidth. Even if C_{neg} is different from C_{pos}, the net reactance slope

$$\frac{dX_{NFmatching}}{d\omega} = \frac{-1}{\omega^2} \cdot \frac{(C_{neg} - C_{pos})}{(C_{pos}C_{neg})}, (C_{pos} - C_{neg} \to 0) \qquad (2.12)$$

is still mitigated by the negative slope of the non-Foster element, broadening the compensation bandwidth.

2.3 Application

Having identified the advantages of the non-Foster impedance matching, many researches have applied it to broadband RF and microwave circuits and antennas. The fun-

damental idea is to utilize the non-Foster property to compensate for the Foster impedance, achieving a more constant (less sloped) reactance so that the bandwidth of the circuits or antennas can be increased. The derived applications are shown in Fig. 2.4.
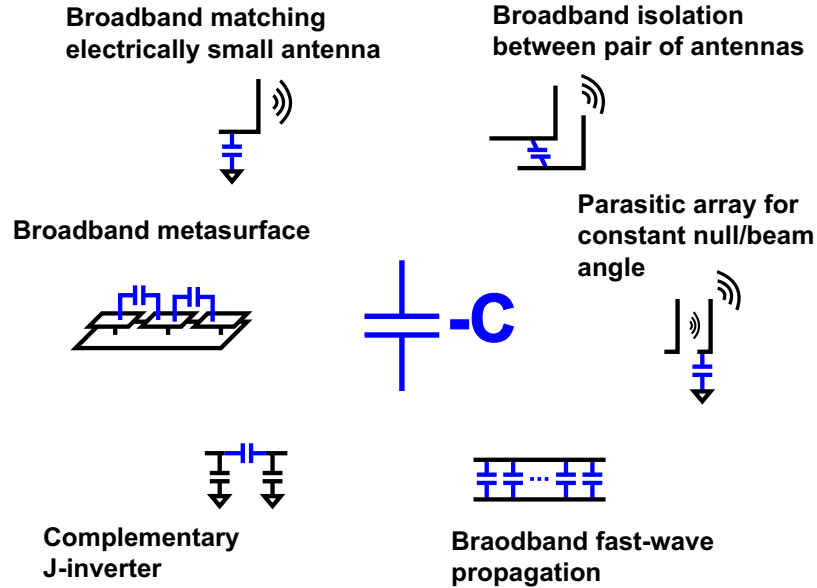
Figure 2.4: Potential applications of non-Foster impedance in RF/microwave circuits and antenna systems.

The most straightforward idea is to increase the matching bandwidth of an ESA. Theoretically, an ESA has very large reactance and small radiation resistance, which leads to very large Q and small matching bandwidth [29]. It is beneficial to match an ESA with non-Foster impedance. In particular, a negative capacitor can be used for broadband by canceling the reactance of a capacitive ESA, like a shorted dipole or a small patch [30]. There have been a lot of associated researches on non-Foster matching ESAs with significant improvement in bandwidth [31–34].

In a similar manner, a non-Foster circuit can be used to compensate for the coupling of two antenna system [35], achieving broadband isolation of the two closely placed antennas, which is important for the current multiple-input and multiple-output system and modern radar system [36]. Specifically, if the two antenna are capacitively-coupled,

a negative capacitance can be used, whereas a negative inductor is applied to isolate two inductively-coupled antennas.

Also, non-Foster impedance can be applied to MTM unit cells designed for broadband MTMs and MTSs. Constant or frequency-independent impedance of the unit cell can be obtained by loading the non-Foster impedance to the passive metallic unit cell structure. The macroscopic EM properties of the MTMs and MTSs (e.g. phase velocity) thus become broadband owing to the broadband unit cells. There have been broadband fast and slow wave periodic structures based on non-Foster loaded unit cells [37, 38], which are of primary interest in this thesis.

In addition, non-Foster impedance can be used to reduce circuit response time. It is well known that the RC constant determines the speed of the system response. It is thus desirable to reduce it in order to achieve faster response times. Using a passive approach can not decrease the RC constant, because more poles always result in the system response, reducing the bandwidth. In contrast, the only possible way is to use non-Foster impedance. In particular, a negative capacitor is able to directly reduce the network capacitance and loss without introducing any new zeroes or poles [39, 40]. It is, therefore, promising to use negative capacitors to increase the speed of the electronic system or even optical system [41].

Furthermore, with the counter-clockwise loci of the impedance on the Smith chart or the positive reflection phase, non-Foster can also be utilized to control the phase of the wave transmission and reflection, and can be further applied to a broadband antenna array to solve the beam squint problem [33]. This thesis covers non-Foster circuit fast wave and slow wave applications, which will be detailed in Chapters 3, 4, and 5.

2.4 Non-Foster Circuit Design

2.4.1 Basic principle

In order to achieve a non-Foster impedance, active circuits must be involved. More-over, positive feedback must be included to produce zeroes or poles on the right half plane of the complex frequency domain. Generally speaking, a non-Foster network can be either a single-port or a two-port network, depending on how it is configured in the system (series or shunt). A non-Foster impedance that is shunt connected to the system is usually re-garded as a single-port network, with input impedance being non-Foster like, as illustrated in Fig. 2.5(a). By contrast, a two-port network is usually used to describe a non-Foster impedance connected in the system in a series manner, as shown in Fig. 2.5(b). Note that a series non-Foster impedance is categorized as a two-port floating non-Foster element, and shunt connected non-Foster impedance is considered as a single-port, single-ended version in some literature [31, 42].

(a)

(b)
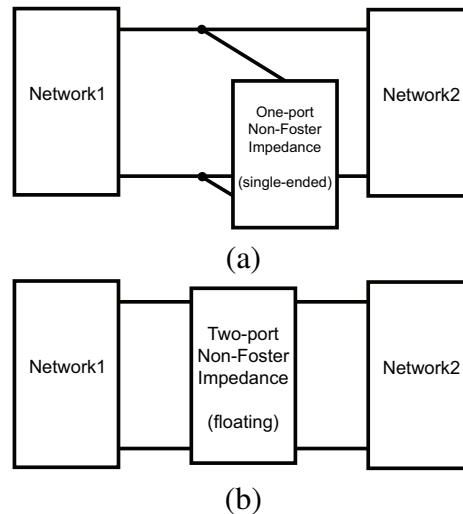
Figure 2.5: Single-ended and floating non-Foster impedance. (a) The single-ended impedance is connected to the network in shunt manner. (b) A floating impedance is connected in a "series" in the network.

No matter what configuration is used, the non-Foster impedance is obtained from positive feedback. In particular, a NIC is a typical non-Foster circuit that reverses the voltage/current of an impedance loaded in the circuit and reflects it at the input port while copying the current/voltage to the input port, so that the input impedance is seen as negative of the loaded impedance.
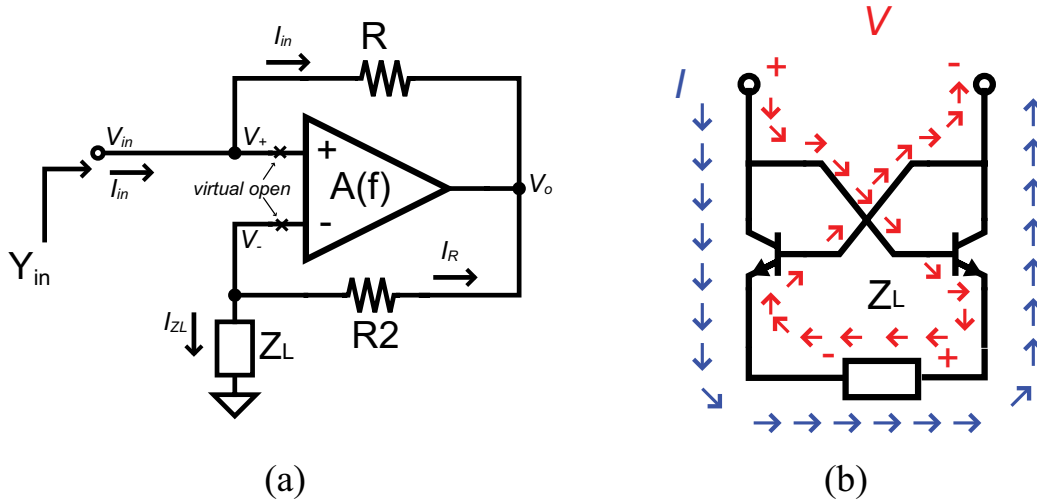
Figure 2.6: NIC circuit. (a) Op-amp based NIC copies the inverse of the current through the load Z_L to the input port, while maintaining the voltage. (b) Transistor based NIC invert the voltage across the load Z_L, while preserving the direction of the current.

Fig. 2.6 presents two type of NIC circuits based on either an operational amplifier (Op-amp) or bipolar junction transistors (BJTs). Both configurations contain positive feedback, and a current or voltage conversion is easy to identify. In particular, from Fig. 2.6(a), based on the basic characteristics of the Op-amp, we have

$$V_+ = V_- = V_{in} = V_{Z_L} \qquad (2.13)$$

$$I_+ = I_- = 0. \qquad (2.14)$$

It is thus easy to derive

$$I_{in} = \frac{V_+ - V_o}{R} = \frac{V_- - V_o}{R} = I_R. \tag{2.15}$$

Because no current flows into Op-amp ($I_- = 0$), all the current I_R must return to ground through Z_L. Considering the current direction, we have

$$I_R = I_{in} = -I_{Z_L}. \tag{2.16}$$

Therefore, the input impedance is derived as

$$Z_{in} = \frac{V_{in}}{I_{in}} = \frac{V_{Z_L}}{-I_{Z_L}} = -Z_L, \tag{2.17}$$

from which it can be understood that the input current is the reverse of the current through Z_L, leading to the negative of Z_L, a non-Foster impedance. In contrast, the input current for the BJT based NIC (see Fig. 2.6(b)) is the same as the current flowing through the load Z_L. It is, however, the voltage across the load that is reversely copied to the input, resulting in a non-Foster impedance. The derivation for BJT based NIC is covered in the next part of this chapter.

Both circuits are capable of producing non-Foster impedance; their differences only exist in practical issues, such as fabrication, and parasitics, which are listed in Table 2.2.

The Op-amp based NICs are easy to build and keep stable because the zeroes and poles of the Op-amp are well defined and controlled by external electronic components. However, Op-amp NICs are usually limited to operating frequencies and small bandwidth due to their extremely high open loop gain. In contrast, BJT based NICs have more freedom to control the loop gain and usually work for higher frequencies. However, the BJT based

Table 2.2: Comparison of Op-amp based NIC and BJT based NIC.

	Op-amp based NIC	BJT based NIC
Parasitics control	easy	hard
Bandwidth	< 50 MHz	> 100 MHz
Desgin freedom	limited	flexible
Fabrication	easy	hard

NICs struggle to control the parasitics of all the electronic components, which may cause serious stability problems. Nevertheless, due to its advantages in bandwidth and design freedom, BJT based NIC was chosen for the design in this thesis.

(a)   (b)
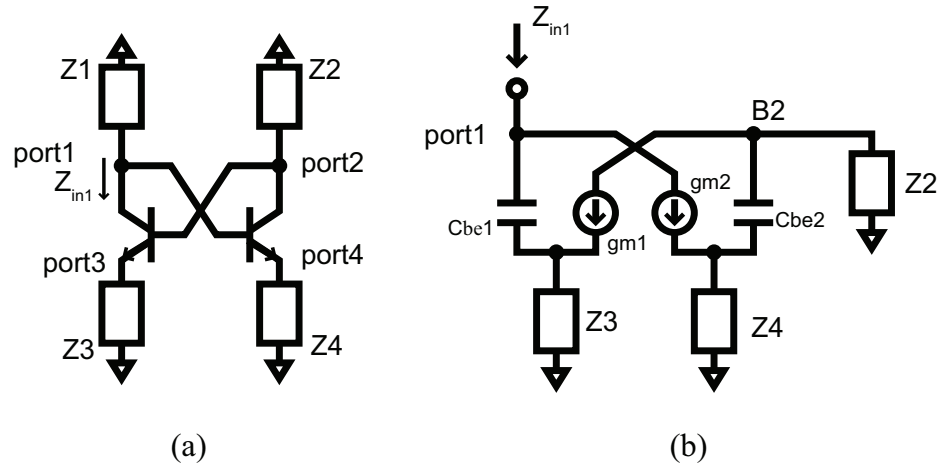
Figure 2.7: Linvill's NIC based non-Foster circuit. (a) schematic, with any of the four ports taken as the input port and the other three taken as the load, the input impedance is the function of the loaded impedance of the other three. (b) A small signal model when port 1 is taken as the input port.

2.4.2 Transistor based non-Foster circuits

A non-Foster impedance is generated by a BJT based NIC circuit. The first NIC circuit was presented by Linvill in 1953 [43] and since then has been extensively studied [44–49]. A general single-ended NIC configuration, consisting of two cross coupled

transistors, is displayed in Fig. 2.7. The input impedance at any of the four ports can be easily calculated as a function of the attached loads at the other three ports. Taking one of the collectors as the input port (e.g port 1), the input impedance can be derived from the small signal model illustrated in Fig. 2.7(b). The derivation is as follows: Starting from the load Z_3, it is easy to calculate

$$v_{Z3} = i_{Z3} \cdot Z_3 \tag{2.18}$$

$$i_{Z3} = sC_{be1}v_{be1} + g_{m1}v_{be1} \tag{2.19}$$

from which, V_{Z3} is derived as

$$v_{Z3} = Z_3(sC_{be1} + g_{m1})v_{be1}. \tag{2.20}$$

Then the input voltage is

$$
\begin{aligned}
v_{in} &= v_{Z3} + v_{be1} \\
&= [1 + Z_3(sC_{be1} + g_{m1})]v_{be1}.
\end{aligned}
\tag{2.21}
$$

In a similar manner, the relation of v_{be1} and v_{be2} can be obtained when equating KVL at point B2 in Fig. 2.7(b), which gives

$$v_{be1} = \frac{1 + Z_4(sC_{be2}g_{m2}) + Z_2sC_{be2}}{-Z_2g_{m1}} \cdot v_{be2}. \tag{2.22}$$

Thus, substituting Eq. 2.22 in Eq. 2.21,

$$v_{in} = [1 + Z_3(sC_{be1} + g_{m1})] \cdot \frac{1 + Z_4(sC_{be2}g_{m2}) + Z_2sC_{be2}}{-Z_2g_{m1}} \cdot v_{be2}. \tag{2.23}$$

On the other hand, the input current is the sum of the current through C_{be1} and the one from g_{m2}, which is

$$
\begin{aligned}
i_{in} &= g_{m2}v_{be2} + sC_{be1}v_{be1} \\
&= \left[g_{m2} + sC_{be1}\frac{1 + Z_4(sC_{be2} + g_{m2}) + Z_2 sC_{be2}}{-Z_2 g_{m1}} \right] v_{be2}.
\end{aligned}
\tag{2.24}
$$

Therefore, the input impedance when looking into the input port 1 is

$$
\begin{aligned}
Z_{in,port1} &= \frac{v_{in}}{i_{in}} \\
&= \frac{[1 + Z_3(sC_{be1} + g_{m1})][1 + Z_4(sC_{be2} + g_{m2}) + Z_2 sC_{be2}]}{-Z_2 g_{m1}g_{m2} + sC_{be1}[1 + Z_4(sC_{be2} + g_{m2}) + Z_2 sC_{be2}]}.
\end{aligned}
\tag{2.25}
$$

If the junction capacitance C_{be1} and C_{be2} are small enough to be neglected, the input impedance can be simplified as

$$
Z_{in,port1} = \frac{(1 + Z_3 g_{m1})(1 + Z_4 g_{m2})]}{-Z_2 g_{m1}g_{m2}}.
\tag{2.26}
$$

Furthermore, if the transistor are ideal, the input impedance becomes

$$
Z_{in,port1} = -\frac{Z_3 Z_4}{Z_2},
\tag{2.27}
$$

clearly showing that the input impedance is the negative function of the three loaded impedance. Therefore negative inductors or capacitors can be obtained by properly choosing Z_2, Z_3, and Z_4. Practically, two of them can be of the same type, providing a scaling factor. For example, if -1 nH is needed, Z_3 can be 1 pF and Z_4 and Z_2 can be chosen a pair of resistors with a value ratio of 1000.

Provided the emitter of the BJT, such as port 3, is taken as the input port, the input impedance can be derived through the same analysis, which can be expressed as

$$Z_{in,port3} = \frac{(1+sC_{be1}Z_1)[1+sC_{be2}Z_2+Z_4(sC_{be2}+g_{m2})]-g_{m1}g_{m2}Z_1Z_2}{(g_{m1}+sC_{be1})[1+sC_{be2}Z_2+Z_4(sC_{be2}+g_{m2})]}, \qquad (2.28)$$

which can be further simplified when making the transistors ideal, as

$$Z_{in,port3} = \frac{-Z_1Z_2}{Z_4}. \qquad (2.29)$$

Therefore, Eq. 2.27 and Eq. 2.29 show that for the NIC described in Fig. 2.7(a), a general input and load impedance relation can be expressed as

$$Z_1Z_2 = -Z_3Z_4. \qquad (2.30)$$

By taking out any of the loaded impedance that one of the four ports, the input impedance at that port can be derived by manipulating Eq. 2.30. No matter whichever port is taken as the input port, the input impedance is always non-Foster impedance.

2.4.3   Stability

Owing to the positive feedback, a non-Foster circuit is intrinsically unstable. NIC circuit is generally used for voltage controlled oscillator design [50–52]. Consequently, it often can not work alone. Instead, a proper load must be connected to the input port to stabilize the non-Foster circuit. As described above, the four ports in Fig. 2.7(a) can be configured as input port. However, the port at the collector requires a stabilizing impedance which must be much smaller than the non-Foster impedance. As an extreme case, a short

circuit is guaranteed to make the non-Foster impedance stable. Thus, the ports at the collector are called short circuit stable (SCS) ports. By contrast, an open circuit makes the non-Foster impedance at the emitter port stable, so the ports at the emitter are open circuit stable (OCS) ports [43, 53]. All the OCS and SCS ports can be obtained by analyzing the input impedance as shown in Eq. 2.25 and Eq. 2.28.

It should be noticed that OCS and SCS only indicate the extremely stable case. This can help a designer to choose a port based on what loading impedance the non-Foster circuit is connected to; however, it does not guarantee stability if the loading impedance is just slightly smaller than the SCS port non-Foster impedance. To examine the stability accurately, Nyquist criterion based frequency domain technology should be utilized [54]. The response of the net impedance, which is the combination of the load impedance and the non-Foster impedance, is derived over a broadband frequency range. The Nyquist plot reveals whether a right half plane pole exists. The system is working if there is no right half plane poles for any frequency. In addition to the frequency domain method, the time domain approach is also available in most SPICE-model simulation tools.

It is easy to design an unstable NIC circuit. The only practical way to make it stable is to reduce the positive feedback loop gain. The most effective method is to reduce the transconductance g_m of the BJT by reducing the biasing voltage; adding series resistors to the loop can also stabilizes the non-Foster circuit.

2.4.4   Design example

A design examples of SCS negative capacitor circuit is briefly introduced in this section [37] and will be further elaborated in Chapter 3. The schematic of the negative capacitor circuit is shown in Fig. 2.8, where the components' values are listed. Avago BJT
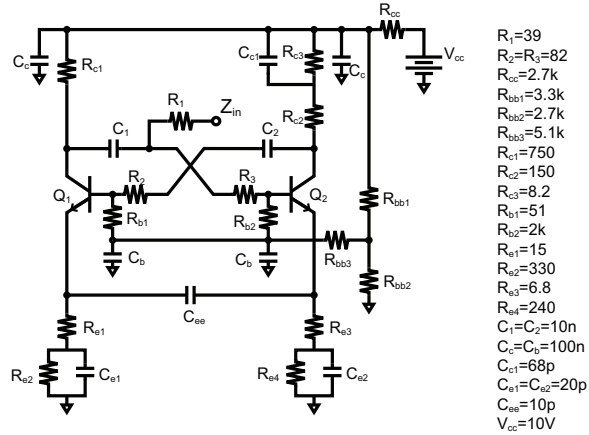
Figure 2.8: A -10 pF negative capacitor circuit. All the component values are listed.

AT41511 is adopted. All the passive electronic components are in the 0603 package. The circuit is designed on a 5 mm^2 printed circuit board (PCB) with FR4 substrate ($\varepsilon_r = 4.4$). The non-Foster impedance is sensitive to the parasitics of the layout. Hence, the parasitics of the actual fabricated layout are extracted from EM simulation in HFSS and further used in circuit co-simulation for stability testing and non-Foster impedance optimization. Also, in order to make the produced non-Foster impedance immune to layout and components parasitics and tolerance, the NIC is modified by adding an additional capacitor across the two emitters of the BJTs. This modification significantly alleviates the components' variation and the parasitics effects from the other lumped components, the layout, and the transistors (except the package lead inductance), making the resultant negative capacitor much less sensitive than conventional NIC circuits to the unexpected components and fabrication deviations. As mentioned above, resistors added in the feedback loop are helpful for stabilizing the NIC. R1 and R2 are thus connected in the loop for additional voltage division at the base of BJT.

In the measurement, it is necessary to examine the stability before measuring the S-parameter. Both time and frequency domain are performed for stability checking. An os-

cilloscope is used to check the direct current (DC) condition and low frequency instability, and a signal analyzer is utilized to examine the high frequency stability. Once the stability is confirmed, the S-parameter measurement is performed to obtain the input non-Foster impedance.

Fig. 2.9 shows the simulation and measurement results for a 10 pF loaded capacitor biased at 10.5 Volts [37]. A -10 pF equivalent input capacitance, C_{eff}, with a small variation (less than 1 pF) over the frequency range from 10 to 150 MHz is achieved in the measurement. The simulation and measurement match each other, confirming the measured result. The discrepancies in equivalent capacitance and Q factor are due to extra parasitics which were not included in the co-simulation. The circuit also shows tunability. More details are presented in Chapter 3.
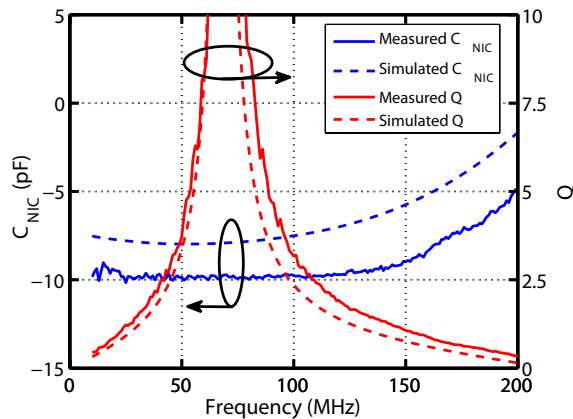
Figure 2.9: Measurement (solid curves) and simulation (dashed curves) results of the designed -10 pF negative capacitor circuit. The red curves include the quality factor Q of the input capacitance. The blue curves represent the input capacitance. [37]

2.5   Summary

In summary, this chapter introduces the basic information of the non-Foster circuit. At first, the definition of non-Foster impedance and its special characteristic in comparison to the passive Foster impedance are presented. Secondly, based on non-Foster properties, the advantages of non-Foster matching are discussed, followed by practical RF and microwave circuit and antenna applications associated with non-Foster circuits. Thirdly, the design of NIC based non-Foster circuits is studied, in which the input impedance of BJT based NIC is analyzed in detail. For practical applications, stability must be considered because non-Foster impedance is intrinsically unstable. Finally, a -10 pF negative capacitor circuit is presented as an example.

The design example in Sec. 2.4 is based on the published paper: J. Long, M. Jacob, D. Sievenpiper, "Broadband Fast-Wave Propagation in a Non-Foster Circuit Loaded Waveguide," *IEEE Trans. Microw. Theory Techn.*, vol. 62, pp. 789-798, 2014.

Chapter 3

Non-Foster Loaded Waveguide for Fast Wave Application

Knowing the special property of the non-Foster impedance, the first application to present here is the non-Foster loaded waveguide for broadband fast wave propagation.

3.1   Background and Motivation

The applications relating to the manipulation of the EM wave propagation for antennas [21, 55–58], cloaking devices [11, 59], and other microwave applications [60] need fast-wave propagation, where the phase velocity is faster than the speed of light in vacuum. As is well known, faster-than-light phase velocity can be easily realized by a non-TEM metallic waveguide and it has been applied to leaky wave antennas [56], and super coupling and energy squeezing devices [60]. Also, MTMs that support fast-wave propagation, including CRLH structures [57, 58] and SRRs [11, 59], have also been proposed. However, all these approaches for fast-wave propagation are dispersive, which reduces the bandwidth

of operation. Thus, it is desirable to find a method of implementing non-dispersive fast-wave propagation such that the phase velocity can be faster than the speed of light and independent of frequency.

The dispersion in the conventional fast-wave structures is attributed to the resonance. A non-TEM wave in a rectangular waveguide is dispersive due to its transverse resonance. All the other aforementioned realizations of the fast-wave propagation [11,57–59] are also based on resonance. The reason why resonance is often used for faster-than-light phase velocity originates from the well-known equation,

$$v_p = \frac{c}{\sqrt{\mu_r \times \varepsilon_r}}, \tag{3.1}$$

where c is the velocity of light in vacuum and ε_r and μ_r are the relative permittivity and permeability, respectively. The requirement of fast-wave (i.e., $v_p > c$) dictates that at least one of ε_r and μ_r has to be less than 1. This property can be easily achieved with the negative slope of the reactance or susceptance in EM structures at their anti-resonant frequencies. Nevertheless, the inverse relationship between the quality factor (Q) and the bandwidth of a resonance results in a trade-off between the loss and the maximum achievable bandwidth.

Fortunately, resonance is not the only way to realize an ε_r or μ_r less than 1. A non-Foster circuit has an input impedance with a negative reactance/susceptance slope vs. frequency, and consequently, it is able to compensate for the positive slope of a natrual reactance/susceptance without utilizing any resonances. Thus, non-Foster circuits are good candidates to obtain broadband fast-wave propagation.

In [24], Dr. Hrabar designed a unit cell consisting of a negative capacitor attached to a short TL and simulated an EM cloak. In [22], we have shown the possibility of designing beam-squint-free leaky wave antennas with non-Foster circuits. Both papers reported

measurements on single unit cell and the multiple-unit-cell simulations for investigating the effects of the large scale EM structures. The only available measurement of a multi-section fast-wave structure was presented over the bandwidth of $2 - 40$ MHz in [61, 62], where the negative capacitors were realized with op-amp circuits. As is well known, an op-amp circuit is an integrated circuit whose available operating frequency is usually below 50 MHz owing to the fixed gain-bandwidth product and its parasitics. In contrast, benefiting from the higher transition frequencies, transistor based circuits can work at higher frequencies. Additionally, the transistor based circuits are more desirable than op-amp circuits in integration, as the former possess less complexity and chip area-consumption. Therefore, transistor based non-Foster circuits earn more interests in realizing negative capacitors at higher frequencies and thus the broadband fast-wave applications.

In this Chapter, a discrete transistor based negative capacitor circuit has been proposed and integrated into a microstrip line (MLine). A three-unit-cell loaded MLine has been successfully fabricated and tested. The retrieved effective material parameters from the measured S-parameters identify an effectively uniform medium with a constant (less than 10% variation) phase velocity of $1.2c$ over $60 - 120$ MHz, or 2:1 bandwidth. Compared to [61, 62], the central operating frequency has been increased from 20 MHz to 90 MHz, and the bandwidth is still significantly more broadband than the conventional metallic waveguides. Furthermore, the measurement results have been verified by Kramers–Kronig relations and the measured near field distribution along the MLine, which demonstrate that the accomplished waveguide can be regarded as a stable, causal, and homogeneous material rather than a lumped element. Thus, this work shows the possibility of cascading multiple unit cells with transistor based non-Foster circuits to achieve an effectively homogeneous material that supports broadband fast-wave propagation. The accomplished

fast-wave waveguide can potentially be applied in broadband beam-squint-free leaky wave antennas and thin film cloaking techniques [55].

The Chapter is organized as follows: Section 3.1 introduces the fast-wave propagation and discusses the possibility of broadband fast-wave propagation with non-Foster circuits. Section 3.2 presents the analytical calculation of the phase delay in a TL periodically loaded with negative capacitors. The design and measurement of the transistor based negative capacitor circuit are detailed in Section 3.3. The implementation and measurement of the integrated fast-wave waveguide structure are shown in Section 3.4, including the fabrication, S-parameter measurement, the retrieved properties of the effective homogeneous material. It follows the verification on causality based on Kramers–Kronig relation in Section 3.5. More discussion on the stability of the non-Foster loaded waveguide and its number of unit cells is presented in Section 3.6. Section 3.7 draws the conclusion.

3.2 Principle

3.2.1 Periodic loaded transmission line model

Fast-wave propagation in a guided medium can be analyzed by using the basic TL theory. The proposed fast-wave waveguide consists of a MLine that is periodically loaded with negative capacitors, as illustrated in Fig. 3.1. The effective capacitance per unit length of an unloaded MLine can be easily derived from [63]. Provided that the negative capacitors have an absolute capacitance value that is smaller than the capacitance of the bare MLine, they reduce the net capacitance of the loaded MLine while keeping the total capacitance per unit length to be positive. Meanwhile, the inductance does not change. Consequently, the resultant phase velocity gets larger. Therefore, it is possible to have a faster-than-light
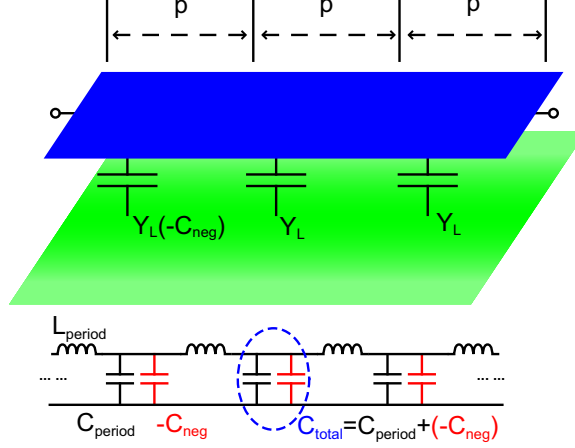
Figure 3.1: The proposed fast-wave propagation structure and its equivalent TL model.

phase velocity by properly choosing the negative capacitance.

To characterize the phase velocity accurately, the loaded MLine is modeled as general periodic structure with unit cells that are composed of a short TL and lumped capacitor. Therefore, it can be analytically studied based on the periodically loaded TL theory, as detailed in [16, 28]. The phase delay of one section of a loaded TL is obtained as

$$\theta = \arccos \left[\cos(kl) - \frac{Y_L}{2Y_0} \sin(kl) \right], \tag{3.2}$$

where k is the propagation constant of the unloaded MLine, l and Y_0 are the length of a section of the MLine (i.e., one unit cell) and its characteristic admittance, respectively, and Y_L is the admittance of the periodic load. According to Fig. 3.1, Y_L is a negative capacitor, and thus,

$$Y_L = -j\omega C_{neg}, (C_{neg} > 0). \tag{3.3}$$

The TL to be fabricated consists of a MLine that is 100 mm long (i.e., the length of

three unit cells) and 10 mm wide on a 62 mil thick FR-4 substrate (ε_r=4.4). The effective capacitance per unit cell, C_{period}, is calculated to be 10 pF, and the effective dielectric constant $\varepsilon_{r,eff}$ is 3.7 [63]. Since C_{period} is proportional to $\varepsilon_{r,eff}$, the required effective capacitance per unit cell that leads to unity effective dielectric constant is

$$C_{period,unity} = \frac{C_{period}}{\varepsilon_{r,eff}} = 2.7pF. \tag{3.4}$$

For the sake of achieving fast-wave phase velocity while avoiding backward propagation, the effective dielectric constant has to be between 0 and 1, which leads to that the total effective capacitance, C_{total}, as shown in Fig. 3.1, must be smaller than $C_{period,unity}$ but remain positive. This is expressed as

$$0 < C_{total} = C_{period} + (-C_{neg}) < C_{period,unity}, \tag{3.5}$$

where $-C_{neg}$ is the loaded negative capacitance in Fig. 3.1. Taking C_{period}=10 pF and $C_{period,unity}$=2.7 pF, the loaded negative capacitance, $-C_{neg}$, should be between -10 pF and -7.3 pF. To verify the analytical theory, the phase delays of a three-unit-cell loaded MLine, as shown in Fig. 3.1, are calculated based on (2), with $-C_{neg}$ equal to -7 pF, -8.5 pF, and -9.5 pF, respectively. The phase delays for the different values of $-C_{neg}$ are compared to the phase of light passing through the vacuum of the same distance (black, solid curve, with triangle markers) in Fig. 3.3. It is clear that the phase delay curves are above the light curve when the $-C_{neg}$ is less than -7.3 pF implying fast-wave propagation, whereas drops below the light line when the $-C_{neg}$ increases to -7 pF, which follows what we have defined for the range of $-C_{neg}$ required by the fast-wave propagation.
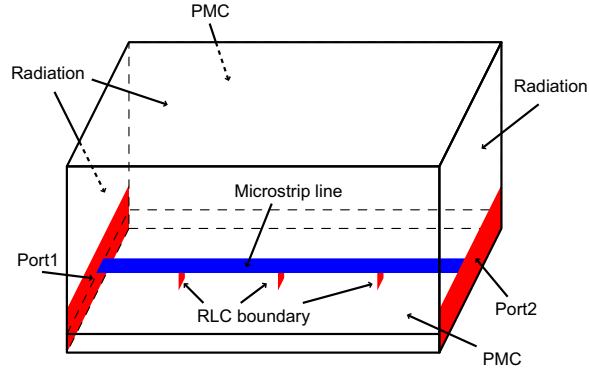
Figure 3.2: Numerical simulation model of the proposed periodically loaded TL.
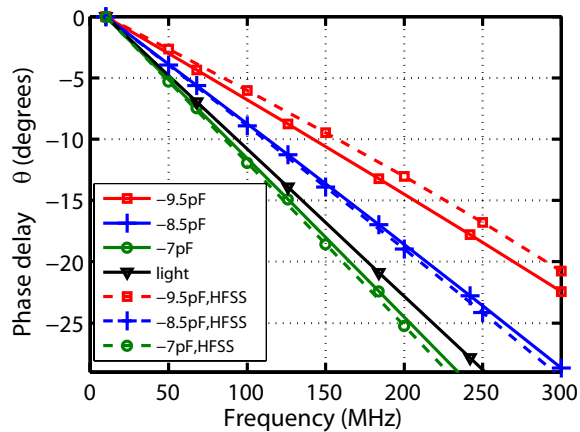
Figure 3.3: Phase delay versus frequency for the cases of different lossless negative capacitors. Dashed lines are EM simulation results and the solid lines are the analytical results based on Eq. 3.2. Different colors are the results with different loading capacitance. The black solid line with triangle marker is the phase delay of light traveling through the same distance in free space.

3.2.2   Numerical simulation

A simulation for the same structure is obtained from finite element method based EM simulator. As shown in Fig. 3.2, the arbitrary load impedance was realized with lumped boundary in the simulation. Wave ports were placed at both ends of the MLine. The walls on either side of the MLine were terminated with perfect magnetic conductor boundaries, and all the remaining faces were defined as radiation boundaries. The simulation results are also presented in Fig. 3.3 (dashed curves). Both analytical and simulated results are in

good agreement, and present fast-wave propagation when $-C_{neg}$ are within proper range.

Practically, negative capacitors implemented with active circuits have finite Q. This effect is investigated by replacing Eq. 3.3 with

$$Y_L = -j\omega C_{neg}\left(1 + j\frac{1}{Q}\right), (C_{neg} > 0),\tag{3.6}$$

and substituting it into Eq. 3.2. Fig. 3.4 shows the resultant phase delay associated with $-C_{neg}$ of -9.9 pF and different Q values. It is found that the finite Q affects the phase velocity. Specifically, the phase velocity has a negligible difference when Q is above 50, whereas it gets smaller as loss increases and drops below c when Q is below 2. As discussed in the following section, the active circuit that functions as a negative capacitor has a finite Q, so it limits the bandwidth of the fast-wave propagation.
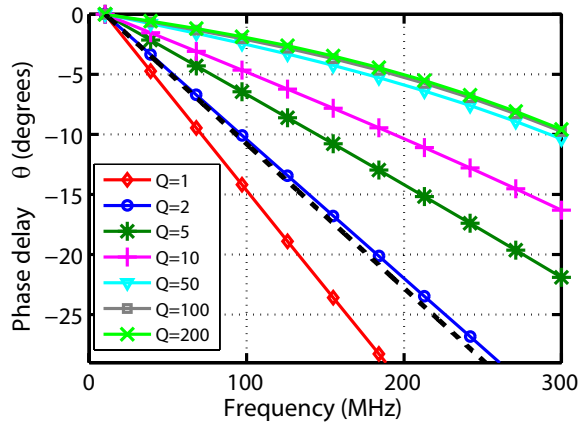
Figure 3.4: Phase delay versus frequency for the cases of loading capacitor with various Q. The curves with different colors and markers refer to different Q. The black dashed line refers to the propagation with the speed of light in free space.

3.3   Non-Foster Circuit

Negative capacitors are classified as non-Foster circuits with reactance having negative frequency slope and impedance locus that goes counter clockwise on a Smith chart [24].

NIC and negative impedance inverter circuits have been proposed for implementing non-Foster elements [31,32,43,64,65]. The conventional basic circuit schematic consisting of two cross coupled transistors is drawn in Fig. 3.5(a). The input impedance at any of the four ports can be easily calculated as a function of the attached loads at the other three ports. For example, the input impedance at port 1 is expressed as

$$Z_{input1,scs} = -\frac{Z_3 Z_4}{Z_2}. \tag{3.7}$$

If Z_3 and Z_2 are resistors and Z_4 is a capacitor, Eq. 3.7 implies that the NIC converts a capacitor (Z_4) into a negative capacitor with a multiplicative factor determined by Z_2 and Z_3. This port at the base-collector junction is defined as a SCS port. One can find another type of port, i.e., an OCS port, by taking one of the emitters as the input port. The corresponding input impedance can be expressed as [43]

$$Z_{input3,ocs} = -\frac{Z_1 Z_2}{Z_4}. \tag{3.8}$$

The definitions of OCS and SCS ports are based on the external loading conditions as required for the stability. For an OCS circuit, the load impedance must be greater than the magnitude of the converted negative impedance, whereas the SCS circuit requires the load impedance to be smaller than the magnitude of the converted negative impedance.
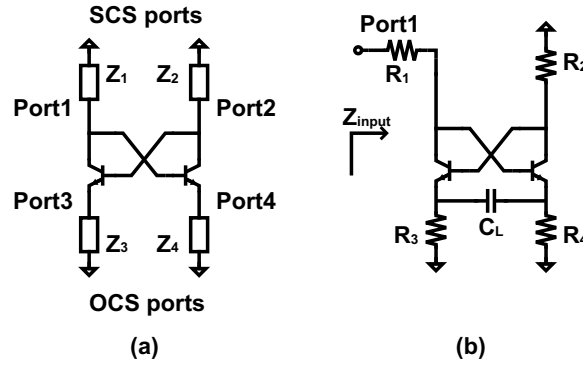
Figure 3.5: Transistor based NIC circuit. (a) The general topology of the NIC circuit. (b) The proposed NIC circuit topology.

The first challenge in the design of an NIC/NII circuit is to decide which port is appropriate. Since the negative capacitor circuit is intended to just partially compensate for the effective capacitance of the MLine for this particular fast-wave application, the magnitude of the negative capacitance must be smaller than the effective capacitance. This means the load impedance (i.e., the impedance corresponding to the effective capacitance of the MLine) must be smaller than the generated negative impedance (i.e., the input impedance of the designed NIC circuit). Therefore, the SCS port is chosen for the circuit design.

Another issue in the design is about the components variation and the parasitics in the circuit, which includes the parasitics of the transistors, discrete components, and PCBs. These variations and parasitics make it harder to explicitly express the input impedance as a simple equivalent capacitance. As a result, the input impedance is no longer a constant (frequency independent) negative capacitance, but instead is a bandwidth limited, non-constant negative capacitance, even with negative resistance. In order to overcome these effects of the variations and the parasitics, a modified topology has been proposed. As shown in Fig. 3.5(b), an additional capacitor C_L is placed across the two emitters. Different from the conventional three-load topology [22, 31], the three loads, Z_2, Z_3, and Z_4 in the new circuit are used for stability and DC biasing. Additionally, the negative capacitance of the
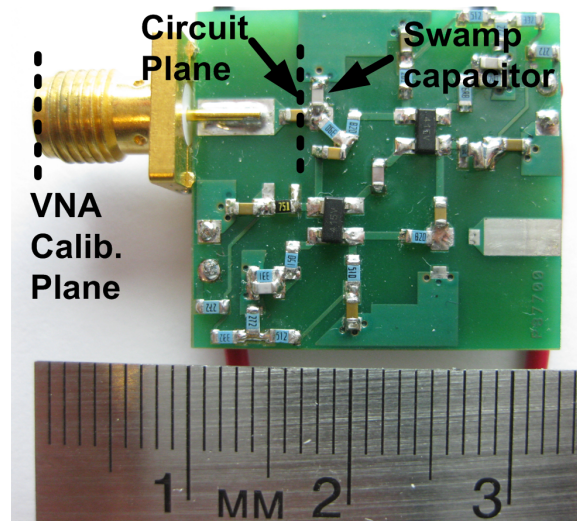
Figure 3.6: The fabricated circuit. The vector network analyzer calibration plane and circuit plane are used for de-embedding the NIC input impedance.

proposed configuration is mainly determined by C_L. This feature significantly alleviates the components variation and the parasitics effects from the other lumped components, the layout, and the transistors (except the package lead inductance), making the resultant negative capacitor much less sensitive to the unexpected components and fabrication deviation than the conventional NIC circuits.

In addition, using the proper port alone does not guarantee the stability. Since the NIC has a positive feedback circuit, the loop gain may become too large due to the unexpected parasitics. Thus, local oscillations may still exist within the circuit. In the practical circuit design, Z_2, Z_3, and Z_4 were carefully chosen to avoid local oscillations. Additional resistance was also added to the feedback loop in order to reduce the loop gain. In the simulation, accurate component models were utilized to include parasitics of the components [66]. The parasitics of the critical paths on the PCBs were extracted from the EM simulation. The stability was examined by using co-simulation techniques with both time and frequency domain stability analysis [42, 67–71].

The designed circuit was fabricated on a 5 cm^2 PCB with FR-4 substrate, as shown

in Fig. 3.6. Avago transistor AT-41511 was adopted. In order to maintain the stability, a positive and large enough swamping capacitor was employed [31, 64]. A two-step measurement technique was used for accurately measuring the negative capacitance. The first step is to measure the swamping element alone. The admittance of this swamping element, Y_{swamp}, is obtained by de-embedding the measured one-port S-parameters from the vector network analyzer (VNA, Agilent E5071C) calibration plane to the circuit plane, as indicated in Fig. 3.6. The second step is to measure the S-parameters of the NIC circuit together with the swamping capacitor following the same de-embedding approach, and it is denoted as $Y_{NIC,swamp}$. Then, the input admittance of the NIC circuit alone is obtained by subtracting the two, as

$$Y_{NIC} = Y_{NIC,swamp} - Y_{swamp}. \tag{3.9}$$

In the measurement, the stability was checked by monitoring any self-oscillations from DC to 10 GHz with signal analyzer (EXA, Agilent N9010A). Apparently, the stability is guaranteed, which leads to further measurement and study.

The simulation and measurement results with a 10 pF loaded capacitor biased at 10.5 Volts are presented in Fig. 3.7. It can be summarized from Fig. 3.7 that the active circuit produces an equivalent capacitance, C_{NIC}, of -10 pF from 10 to 150 MHz (blue curves). The achieved C_{NIC} varies within the range of 1 pF over the bandwidth of interest. The circuit has the maximum Q factor around 75 MHz and drops below 1 after 150 MHz (red curves). Besides, the conclusion from the measured results (solid curves) is affirmed by the simulation results (dashed curves). The discrepancies in equivalent capacitance and Q factor are due to extra parasitics which were not included in the co-simulation.

The tunability of the negative capacitor circuit has also been investigated. The
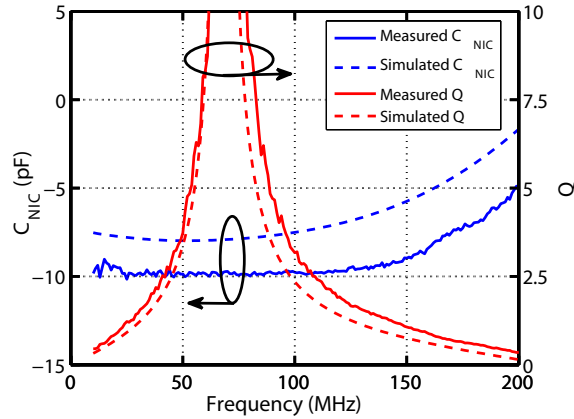
Figure 3.7: The equivalent capacitance of the developed NIC circuit with a loaded capacitor of 10 pF biased at 10.5 Volts and its quality factor. The solid lines are measurement results and the dotted lines are the simulation results.

generated C_{NIC} can be tuned in two ways: (1) by tuning the biasing voltage of the circuit; and (2) by varying the loaded capacitor C_L. Although the capacitor C_L is changed manually in this measurements, it can be tuned with a varactor under careful consideration of the loss and parasitics [22]. The tunability of the circuit is presented in Fig. 3.8. From Fig. 3.8(a) where the DC bias was fixed and the C_L was tuned, it is found that the C_L determines the C_{NIC} when the DC bias is fixed, and slightly affects the slope of the C_{NIC}. Whereas Fig. 3.8(b) illustrates that the slope of the C_{NIC} is strongly dependent on the DC bias. In particular, an optimum range of the DC voltages is required for a wider bandwidth and a smaller variation in the C_{NIC} over frequency. This feature is exploited in our following design since the change in C_{NIC} with frequency is helpful in compensating for the deviation of the phase velocity due to the finite Q problem.

The bandwidth and consistency of the capacitance for different tuned values are limited mainly due to the inductive parasitics in the circuit. It is possible to achieve better performance if more advanced transistors or integrated circuit (IC) technology is adopted. The low Q of the negative capacitor also stems from the parasitics. In addition, the low

(a)

(b)
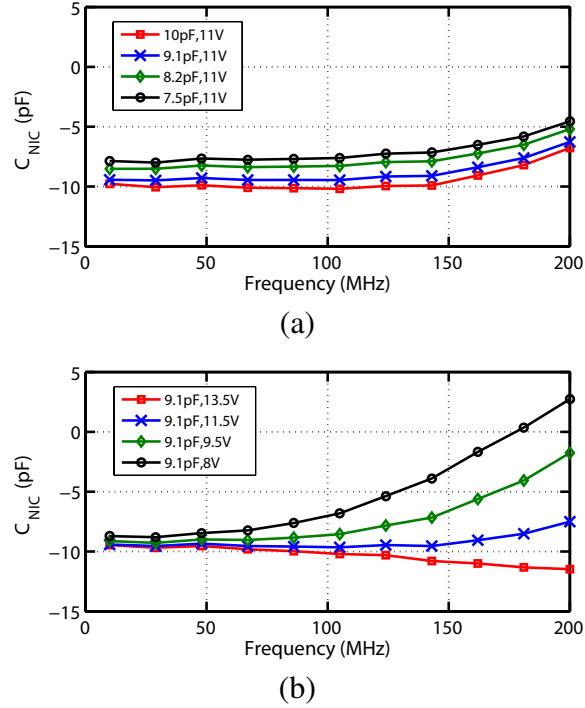
Figure 3.8: The tunability of the designed NIC circuit. (a) C_{NIC} with same biasing voltage and different load capacitance. (b) C_{NIC} with the same load capacitance and various biasing voltages.

Q is a result of the compromise needed to achieve stability, as a finite amount of loss is incorporated into the circuit to reduce loop gain for stability.

3.4 Fabrication and Measurement

3.4.1 Fabrication

The waveguide studied in Section 3.2s has been accomplished with the designed negative capacitor circuits. Fig. 3.9 illustrates how the fast-wave waveguide is fabricated, where three circuit copies of the same negative capacitor design are integrated to a MLine with the width of 10 mm and periodicity of 33 mm on FR-4 substrate. Three vias on the MLine are used to connect to the active circuits. The circuit also has a via at the junction
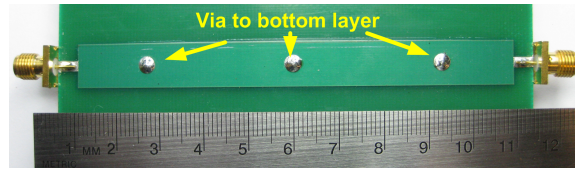
(a)
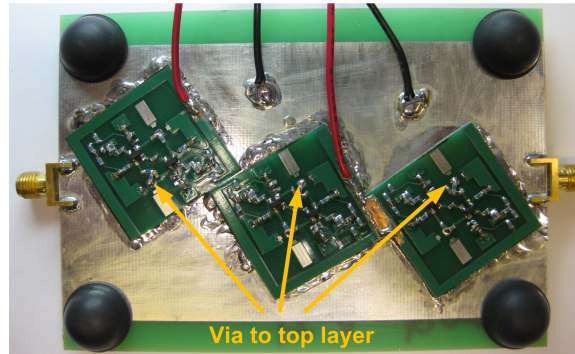
(b)

Figure 3.9: The fabrication of a 3-unit-cell fast-wave waveguide. (a) Top view. (b) Bottom view.

where the swamping capacitor is connected. The circuit and MLine are soldered back-to-back.

A co-simulation for the measurement setup was done with an EM model of the MLine configured with the same manner as described in Section II, where the lumped boundaries were replaced with a via structure and a 50 Ω lumped port.

3.4.2 S-parameter measurement

In the measurement, the stability of the setup was investigated first. In addition to the methods described in Sec. 3.3, a single-tone RF signal was injected into one port, the signal analyzer was used to see if any spurious modulated frequencies were detected at the other port. After the stability was guaranteed, a two-port S-parameter measurement of the fabricated waveguide was performed. The phase delay θ and the group velocity (v_g) were

calculated from the measured S_{21}, as

$$\theta = \angle S_{21}, \tag{3.10}$$

and

$$v_g = -\frac{L}{\frac{\partial \theta}{\partial \omega}}, \tag{3.11}$$

where L=100 mm is the length of the developed waveguide. The phase delay θ and the normalized group velocity v_g to c with the C_L of 9.1 pF at 13 Volts biasing voltage are extracted and plotted in Fig. 3.10.

Fig. 3.10(a) plots the phases of S_{21} and the normalized group velocity. The phases of S_{21} with power on (square markers) and off (diamond markers) are compared to the phase delay of light in vacuum through the same distance (black dashed curve with cross markers). It can be seen that the phase velocity of the waveguide is slower than c when powered off and faster when powered on. Fig. 3.10(b) is the transmission (S_{21}, red curves) and the reflection (S_{11}, blue curves) of the fabricated waveguide. The reflection is well below -10 dB over the frequency of interest, indicating good match. The transmission coefficient is almost 0 dB below 100 MHz and even presents gain above 100 MHz, which is due to the negative resistance of the loaded non-Foster circuits. The maximum gain is about 25 dB near 200 MHz. It should be noted that the circuit is still stable even with reflection and transmission both greater than unity. A discrepancy between simulation and measurement is observed, which is caused by the parasitics from the manual soldering and fabrication.

The tunability of the three-unit-cell fast-wave structure is studied in Fig. 3.11, where
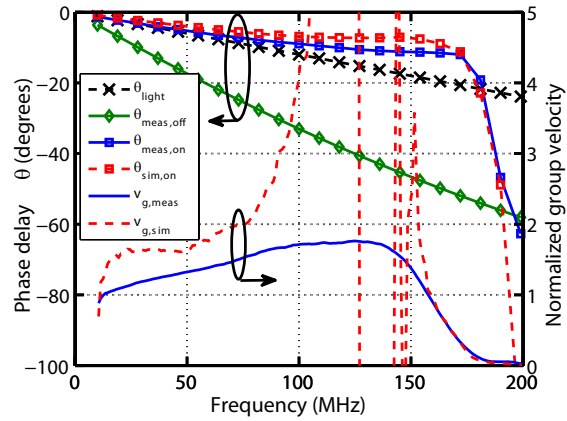
(a)
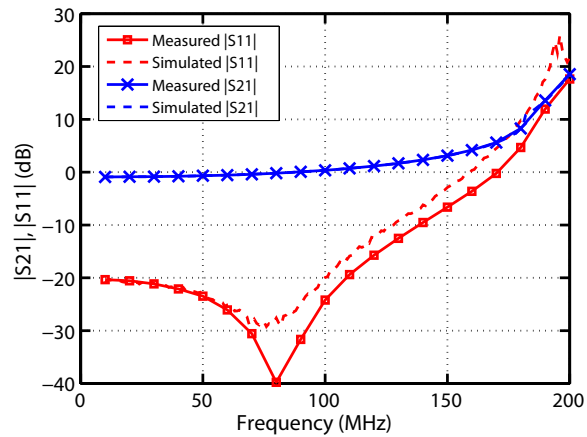
(b)

Figure 3.10: S-parameter measurement of the non-Foster loaded fast-wave waveguide. Dashed lines are simulated results and solid lines are measurement results. (a) The phase of S_{21} and the normalized group velocity. (b) The transmission and reflection coefficient.

three different velocities are obtained by biasing the circuit with different voltages and tuning the load capacitance. The measured tunability results show that the fabricated structure can produce the phase velocity varying from c to $2c$, which can potentially be applied in controlling the phase delay of a guided wave device, such as the feeding system of the phased array antennas. Additionally, it is seen that the bandwidth changes with the tuning, which is because that the bandwidth of the C_{NIC} changes with frequency, as seen from Fig. 3.8. Therefore, the performance of the waveguide relies on the performance of the negative capacitor circuits.
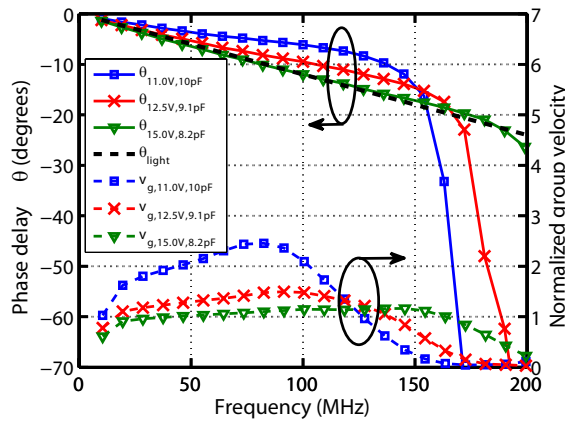
Figure 3.11: The tunability of the three-unit-cell fast-wave propagation structure.

The measured S-parameter in Fig. 3.10 is the transmission and reflection between the two-port network when the developed waveguide is considered as a two-port network with 50 Ω termination, as shown in Fig. 3.12. If this two-port network is considered as an effective homogeneous material which is represented by its characteristic impedance Z_c and phase delay θ, these parameters can be retrieved from the measured S-parameters as [72]

$$Z_c = 50 \times \left(\pm \sqrt{\frac{(1+S_{11}^2)^2 - S_{21}^2}{(1-S_{11}^2)^2} - S_{21}^2} \right), \tag{3.12}$$
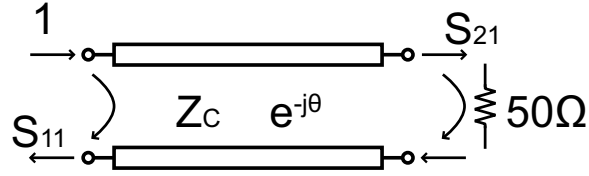
Figure 3.12: An effective homogeneous material under S-parameter measurement.

and

$$e^{j\theta} = \frac{S_{21}}{1 - S_{11}\frac{Z_c-50}{Z_c+50}}. \tag{3.13}$$

The plus or minus sign in Eq. 3.12 will be determined by the following two rules: (1) the correct sign should make the real part of Z_c positive, and (2) the consistency between the resultant imaginary part of θ and the magnitude of S_{21} should be maintained. This is because that Z_c only indicates the ratio of the E-field to H-field (or voltage to current) but does not determine the passivity of the material, which, actually, is dictated by the imaginary part of θ. Since the real part of θ indicates the phase propagation, whereas the imaginary part is the loss of the effective material, the phase velocity can be derived as

$$v_p = -\frac{\omega L}{\theta_r}, \tag{3.14}$$

where θ_r is the real part of the phase delay θ obtained from Eq. 3.10 and L is the total length of the effective homogeneous material, which is 100 mm. The group velocity v_g of the effective material is associated with the derivative of the θ_r to the angular frequency as stated in Eq. 3.11.

The results of the retrieved phase delay θ and the normalized phase velocity v_p are shown in Fig. 3.13(a), where faster-than-light phase velocity can be observed over the band-

width of $50-150$ MHz. Fig. 3.13(b) presents the retrieved loss of the homogeneous material from the imaginary part of θ, which implies less than 1 dB loss below 100 MHz. We can even see gain above 100 MHz due to the negative resistance from the active loads. The consistency between the magnitude of S_{21} in Fig. 3.10(b) and the loss factor in Fig. 3.13(b) validates the retrieved results, which presents an effective low loss fast-wave material over a bandwidth of $50-150$ MHz. Furthermore, a stationary phase velocity about $1.2c$ is observed at 90 MHz in Fig. 3.13(a), indicating perfect dispersionless fast-wave propagation. In particular, the effective bandwidth is 60-120 MHz (i.e., 2:1 bandwidth) by taking 10% variation around $1.2c$.

It should be noticed that the bandwidth of the achieved fast-wave propagation is limited within RF frequency band. This limitation is attributed to the following effects: (1) As discussed in Section II, when the Q of the negative capacitor drops below 2, the phase velocity dramatically decreases. Thus, the most important limiting factor is the finite Q of the negative capacitor circuit. (2) The parasitics of the circuit also lead to additional dispersion, causing extra variation in v_p. All these two problems can be solved by adopting ASIC technologies, where the parasitics are reduced so that it would not affect the functionality at relatively low frequency. Additionally, according to theory of the periodic structure, it should be pointed out that the dispersion is significant if the period is large compared to the operating wavelength. However, this is not the main reason for the limited bandwidth of the realized structure in this research.

3.4.3   Near field distribution measurementss

In order to further verify that the developed fast-wave waveguide indeed represents an effective homogeneous medium rather than a lumped element, the near field distribu-
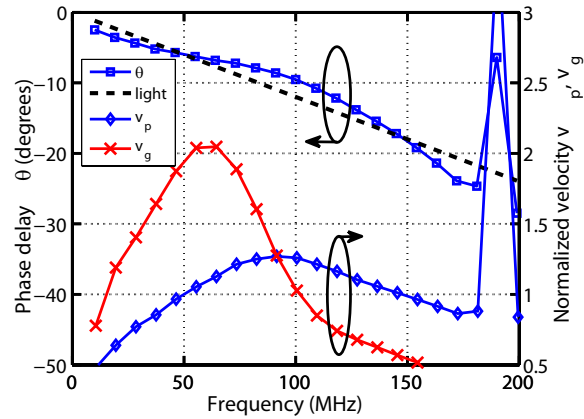
(a)
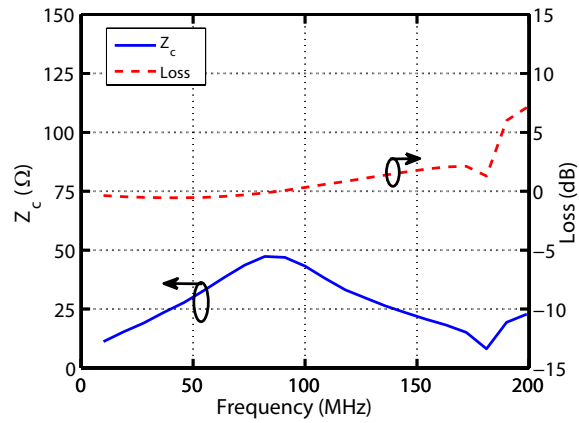
(b)

Figure 3.13: The retrieved effective propagation parameters. (a) Normalized phase velocity, normalized group velocity and phase delay compared to light passing through the same distance in free space. (b) Transmission loss and characteristic impedance.

tion along the MLine has been measured and analyzed. Fig. 3.14 illustrates the near field measurement setup, where one port of the MLine is connected to port 1 of the VNA and the other port is terminated with a matched load. A field detector probe mounted on a 1D positioner sweeps along the MLine (z direction in Fig. 3.14) and measures the electric field. The phase of the coupled power is extracted and presented in Fig. 3.15.
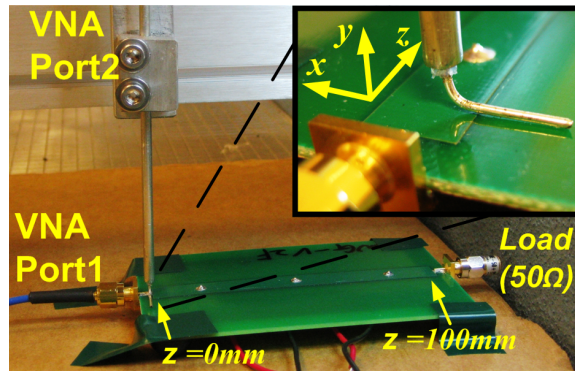
Figure 3.14: The configuration of the near field measurement setup. The probe is scanned along the MLine to obtain the phase as a function of position.

The phases of the near field along the waveguide are derived with four approaches and compared in Fig. 3.15, including (1) the phase of the raw measured near field, (2) the linear fitted phase from the raw near field data, (3) simulated phase from EM simulation, and (4) the calculated phase based on the retrieved parameters of the material. The phase of the raw measured data (blue, solid curve) is obtained directly from the measurement and thus, is noisy. The linear fitted phase (red, dashed curve, with cross markers) is derived by fitting the raw data with the first order linear function in order to extract the slope of the phase variation along the waveguide. The simulated phase (green, dashed curve, with triangle markers) is from the same EM model described in Section III. The calculated phase

(green, dashed curve, with square markers) is extrapolated by

$$\theta = -\frac{2\pi f}{v_p}z,$$ (3.15)

where v_p is the retrieved phase velocity from Eq. 3.14 at a particular frequency f and z is the distance from the port connected to the VNA to the position of the probe.
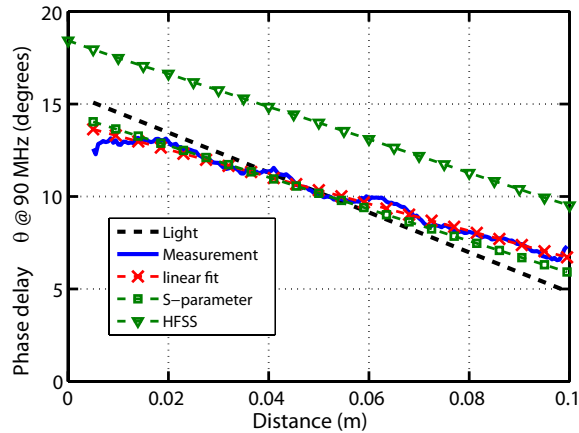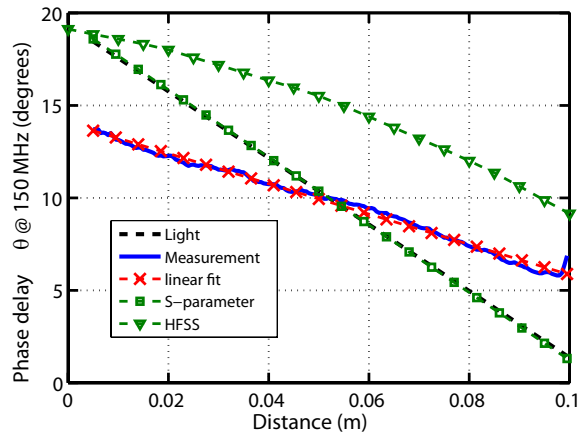
Figure 3.15: Field measurement results at (a) 90 MHz and (b) 150 MHz. Blue solid curve is the measured phase of the coupled field along the MLine, and the red dashed curve with cross markers is the linear fitting result to the measured field. They are compared to the green dashed curve with square markers, which is the result derived from retrieved phase velocity. The EM simulation result (green dashed curve, marked with triangle) is used to verify the measured field.

Fig. 3.15(a) and (b) are the comparison at two frequencies, i.e., 90 MHz and 150 MHz, respectively. It is seen that the results at 90 MHz in Fig. 3.15(a) shows great consistency among the four phases to be compared, supporting the validity of each other. Moreover, compared to the theoretical phase variation of the light in vacuum (black, dashed curve), the four phase results all present less slope than the light, which implies fast-wave propagation. By contrast, near field results deviate from the calculated results at 150 MHz in Fig. 3.15(b), but still keep coherence with the EM simulation. This is because of the change in the frequency dependent characteristic impedance, which can be seen in Fig. 3.13(b) that the characteristic impedance is around 50 Ω near 90 MHz and deviates at other frequencies. To put it another way, the result in Fig. 3.15(a) is with a good matching condition, which indicates that the field in the TL is mainly from a propagating wave. Whereas result in Fig. 3.15(b) is under the condition of large impedance mismatch, so the field distribution are the results of the superposition of multi-reflected waves, or a standing wave.

To conclude this part, the field measurement is valid only when the characteristic impedance is matched to the load. The results within the 50 Ω frequency range show good agreement with the retrieved results in Sec. IV, sub Sec. B. Although the three-unit-cell structure is relatively short compared to the wavelength, the continuously changing of the phase along the waveguide without any abrupt jumps implies that the waveguide can be considered as a homogeneous medium rather than a lumped element, and this has been demonstrated by different methods including analytical calculation, EM simulation, and measurements. The design of a longer fast-wave waveguide with more unit cells is ongoing, which can open many possibilities in the broadband beam-squint-free leaky wave antenna and active thin film MTS for cloaking [55].

3.5   Kramers–Kronig Relation

Although it is seen that both phase and group velocity in Fig. 3.13(a) are larger than the speed of light, Einsteins theory of special relativity is still satisfied. This is because the "superluminal" propagation is obtained over a limited bandwidth, whereas the beginning and ending parts of any meaningful information, which are described with the step function, contain spectrum spreading over the entire frequency range. Therefore, the velocity of the start and end of the information can not exceed c. To put it another way, as discussed in [61,62,73], the speed of the information is determined by the "precursor velocity" or the "front velocity" rather than the group velocity, and they are never faster than c. However, the "precursor velocity" or the "front velocity" argument can not clearly and comprehensively answer the question of whether a band-limited "superluminal" propagation exists or not, and thus it is still an open question calling for further scientific debate.

Regarding to the stability and causality, if the system is stable and causal, the magnitude and the phase of the system response must follow Kramers–Kronig relations [73,74], as

$$\phi(\omega) = -\frac{1}{\pi} P_v \int_{-\infty}^{+\infty} \frac{\ln(G(\omega'))}{\omega' - \omega} d\omega', \tag{3.16}$$

where $\phi(\omega)$ and $G(\omega)$ are the phase and magnitude of a system response, respectively. In order to verify the causality and stability of this system, the magnitude of the measured S_{21} from DC to 10 GHz were applied to Eq. 3.16, the calculated phase (dashed, red curve) is compared with the measured phase of S_{21} (solid, blue curve) in Fig. 3.16, which clearly shows the agreement between the calculated and measured results, indicating that the developed system is causal and stable.
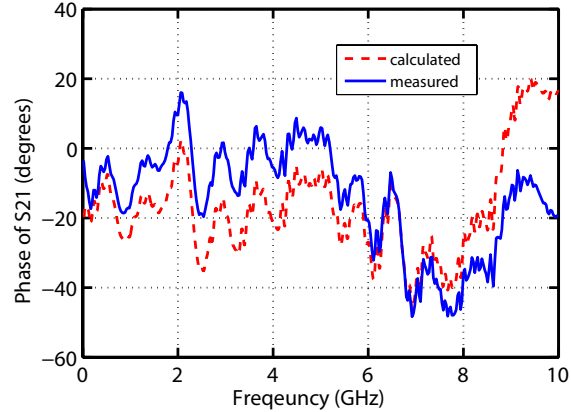
Figure 3.16: Comparison of the measured phase of S_{21} (solid, blue) to calculated results (dashed, red) based on Kramers–Kronig relations.

3.6 Waveguide Length, Unit Cell number, and Stability

It is demonstrated in the previous sections that waveguides with periodically loaded non-Foster circuits have the capability of broadband non-dispersive fast-wave propagation [37, 62], which has been proposed for broadband leaky wave antennas [55, 75], series antenna feeding structures [76, 77], broadband EM cloaking MTSs [78], etc. However, to the knowledge of the authors, only a few researchers have successfully realized and measured broadband fast-wave propagation, and only three cascaded non-Foster circuit loaded unit cell at most have been reported [24, 37, 61, 79]. Moreover, waveguides with non-Foster circuit loads have further been challenged with the lack of unconditional stability [80], which puts doubts on its practical applications in antennas and metasufaces. In fact, based on the Foster theorem, any passive element must have Foster reactance [26], so non-Foster circuits always present gain along with the non-Foster reactance, and thus cascading more non-Foster circuit loaded unit cells must result in potential instability. Nevertheless, despite the potential instability, the multiple non-Foster circuit loaded waveguides can still be stable with specific loads, such as 50Ω, which is usually used as a termination in RF/microwave

circuits.

For demonstration, we have designed and fabricated a 10-unit-cell non-Foster circuit loaded waveguide, which contains significantly more unit cells than the prior work, and furthered this research in realizing a 38-unit-cell waveguide, which, to the author's best knowledge, has the largest number of unit cells and is the longest measured non-Foster loaded waveguide in all published researches [24, 37, 61, 79].

A 10-unit-cell is designed and tested first. The waveguide and non-Foster circuit is designed on a three-layer PCB. The top layer is the MLine, which periodically connects to the non-Foster circuits (bottom layer) through vias. The bottom layer is for the non-Foster circuits, where 10 non-Foster circuit layouts are printed in alternative direction to the MLine. The middle layer is the common ground plane for both of the MLine (top layer) and the non-Foster circuits (bottom layer), which also provides isolation between both the top and bottom layers. Rogers RO4003C is used for both layers of substrates, of which the one for MLine (i.e., above the ground) is 1.5 mm and the other (i.e., below the ground) is 0.2 mm. A thin substrate for the non-Foster circuits helps for better controlling the parasitics. With a 7.5-mm-wide MLine and a periodicity of 10 mm, the capacitance per unit-cell-length is 3 pF, the effective permittivity is 2.97. Therefore, at least 1 pF is needed for achieving fast-wave propagation, and about $1.2c$ phase velocity can be achieved when -2.4 pF is loaded to the waveguide.

The non-Foster schematic shares the same idea of the previously achieved -10 pF in Chapter 2.4, which is presented in Fig. 3.17(a). And the input equivalent capacitance and conductance is shown in Fig. 3.17(b), manifesting a constant -2.8 pF negative capacitance at the input port. The agreement between the simulation and the measurement double confirms the accomplished -2.8 pF capacitor.
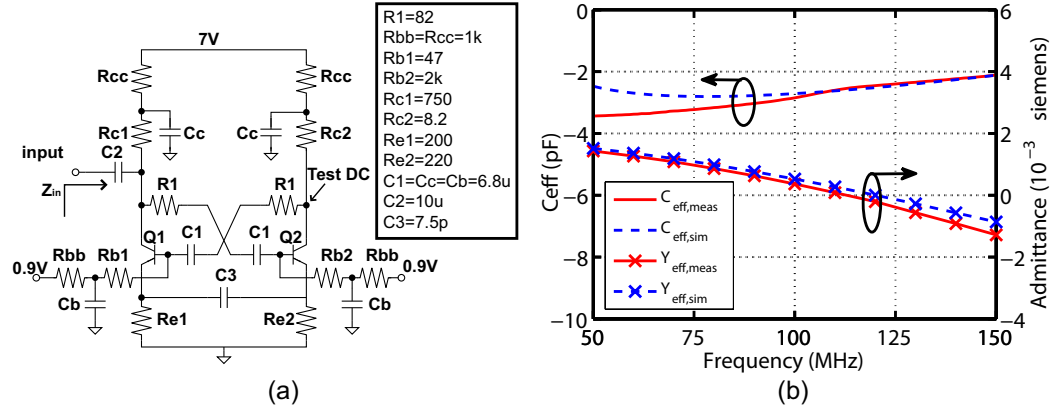
Figure 3.17: Schematics (a) and measurement results (b) of the designed non-Foster circuits.

The implemented -2.8 pF negative capacitor circuits have been incorporated into a 10-unit-cell non-Foster circuit loaded waveguide. The stability of the fabricated waveguide is tested with the time domain experiment setup, where one port of the waveguide is terminated with 50Ω or short (i.e., 0Ω). Three approaches are used for investigating the stability. Firstly, a signal analyzer (EXA, Agilent N9010A) was used to terminate the other port of the waveguide. Spurious oscillation can be read out from the measured spectra of the signal analyzer if the system is unstable. Secondly, DC biasing collector voltage at Q2 (see Fig. 3.17(a)) in one of the non-Foster circuits is monitored by an oscilloscope (Agilent MSO7104B) for low frequency stability and DC bias shift due to the oscillation. Finally, the fabricated waveguide is measured with a VNA (Agilent E5071C). The magnitude of the frequency response is applied to Kramers–Kronig relations for estimating its phase response [74], which is compared with the measured results.

The measurement results are presented in Fig. 3.18. When loaded with 0 Ω, the DC bias is averaged at 6.217 V, and spurious oscillations are found (see Fig. 3.18(a)), implying the waveguide is unstable with short load. In contrast, Fig. 3.18(b) reveals averaged DC voltage of 6.254 V and no oscillations from measured spectrum for the 50Ω load
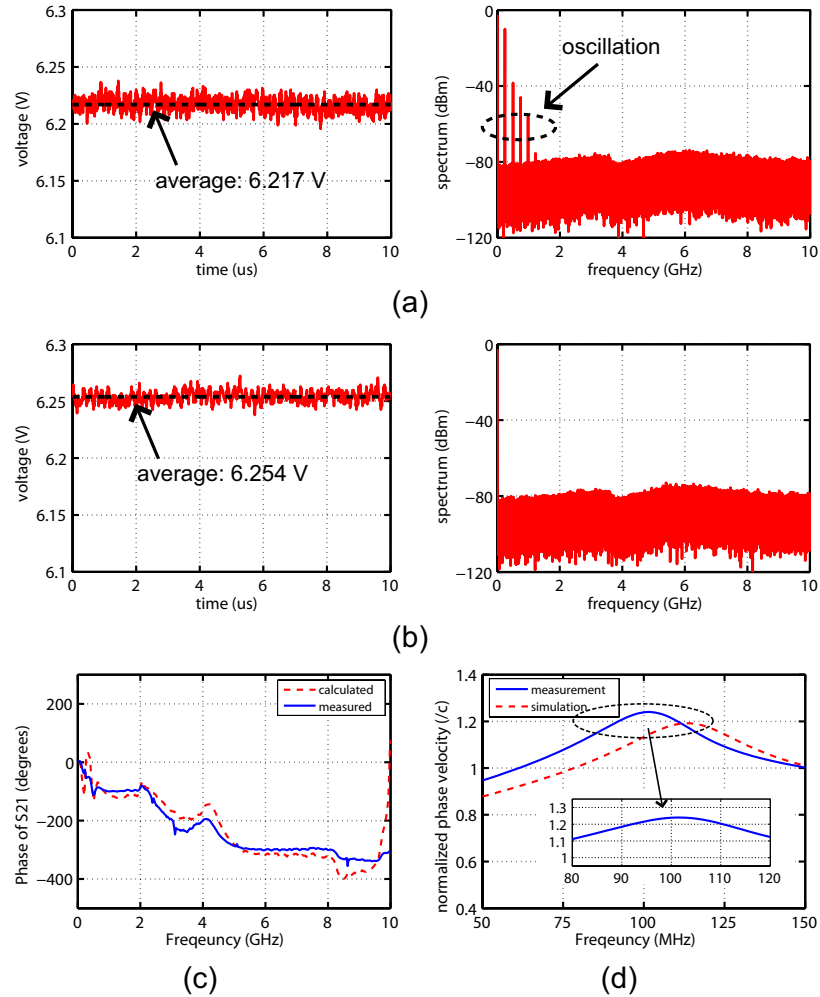
Figure 3.18: Measurement results. (a) The measured DC voltage (left) and spectrum (right) when the waveguide is terminated with short load. (b) The DC voltage and spectrum for 50Ω load case. (c) The comparison of the measured phase S21 to the calculated result based on Kramers–Kronig relations for 50Ω load case. (d) The retrieved phase velocity in measurement and simulation for the 50Ω load case. The inset presents the detail of the retrieved phase velocity in measurement, indicating non-dispersive frequency point and low dispersion band.

case, which indicates stability. The stability and causality have been further demonstrated by Kramers–Kronig relations as shown in Fig. 3.18(c), where the calculated phase of S21 based on Kramers–Kronig relations matches the measurement. The retrieved and simulated phase velocities are exhibited in Fig. 3.18(d), manifesting a fast-wave propagation with the phase velocity of $1.2c$ over the bandwidth of 80–120 MHz (within 10% variation), which is 1:1.5 bandwidth. The inset in Fig. 3.18(d) presents the detail of the retrieved phase velocity from measurements from 80 MHz to 120 MHz. It is clear to see that the phase velocity reaches a maximum at about 100 MHz, where zero-slope phase velocity is obtained. As is known that zero-slope phase velocity indicates non-dispersive propagation, it thus can be concluded that non-dispersive propagation can be achieved at around 100 MHz, which is impossible for any other conventional fast-wave waveguide, such as a metallic rectangular waveguide. Moreover, the phase velocity varies less than 10% around $1.2c$, which can be sufficiently regarded as a low dispersive or non-dispersive band. The discrepancy between the simulation and the measurement is due to the tolerance of the realistic components. The measurement results clearly demonstrate that the 10-unit-cell non-Foster circuit loaded waveguide is stable with, in particular, 50Ω load, even though the waveguide is only conditionally stable.

With the same manner, we successfully increase the number of unit cell up to 38 unit cells and measured a stable fastwave propagation in both time and frequency domain, which will be detailed discussed in Chapter 4.

To sum up this section, although non-Foster circuit loaded waveguide is potentially unstable, it is still possible to ensure the stability with specific loads, which makes the fast-wave waveguide still realizable for applications. For demonstration, we firstly designed a 3 unit cell non-Foster loaded waveguide, and further increase the number of the unit cell to

10 and even 38. It is proved that even though 10-unit-cell non-Foster waveguide is unstable with short load, it is stable with 50Ω load.

3.7   Summary

This chapter reports the implementation of a fast-wave propagation medium over a bandwidth of $50 - 150$ MHz. The fast-wave structure has been accomplished by a TL periodically loaded with transistor based non-Foster circuits. A novel transistor based non-Foster circuit has been proposed for better engineering the negative capacitor. The designed circuit exhibits -10 pF negative capacitance over a bandwidth from 10 MHz to 150 MHz. Three such non-Foster circuits have been attached to a TL and the S-parameters of the fabricated waveguide have been measured. The retrieved material parameters from the measured S-parameter of the developed waveguide characterize an effective homogeneous material with constant phase velocities about $1.2c$ over a bandwidth of $60 - 120$ MHz, which has been further verified by Kramers–Kronig relations and the near field measurement. This design has shown the possibility of cascading multiple unit cells and making an causal, stable, and effective homogeneous fast-wave material with transistor based non-Foster circuits. The proposed structure can be applied to a broadband beam-squint-free leaky wave antennas and cloaking.

Chapter 3 is based on and mostly the reprint of the following paper: J. Long, M. Jacob, D. Sievenpiper, "Broadband Fast-Wave Propagation in a Non-Foster Circuit Loaded Waveguide," *IEEE Trans. Microw. Theory Techn.*, vol. 62, pp. 789-798, 2014; J. Long, D. Sievenpiper, "Stable multiple non-Foster circuits loaded waveguide for broadband non-dispersive fast-wave propagation," *Electronics Lett.*, pp. 1708-1710, 2014.

Chapter 4

Superluminal Pulse Transmission in a Non-Foster Loaded Waveguide and Limitation

It is demonstrated that the non-Foster loaded waveguide is capable of supporting broadband fast wave propagtion, with $v_p > c$. Besides, it is also noticed that for a certain fast wave bandwidth, the group velocity, v_g is also greater than the speed of light, implying superluminal propagation. It is demonstrated on the superluminal propagation in passive MTMs and MTSs, with obvious dispersion. This chapter studies the possibilities of the superluminal propagation in a non-Foster loaded waveguide, and its dispersion. The chapter further discusses its theoretical limitation.

4.1 Background and Motivation

Superluminal propagation has been investigated for decades, owing to its great potential in practical and fundamental applications, such as the fast accessing [81, 82], invisible cloaking [11, 83], leaky wave antennas [22, 55] and the validation of relativity and causality [84–87]. Theoretically, ideal superluminal propagation requires an EM wave to travel in a homogeneous medium with a group velocity defined by a group index $0 < n_g < 1$, as denoted in Eq. 4.1,

$$n_g(\omega) = n_r(\omega) + \omega \frac{\partial n_r(\omega)}{\partial \omega}, \tag{4.1}$$

where n_r is the frequency-dependent refractive index, and the second term is the derivative of the refractive index with respect to the frequency. Normally, no such materials exist because most materials have $n_r > 1$ and positive slope with ω. Nevertheless, considerable research efforts have been made towards accomplishing superluminal propagation using engineered materials with narrow gain/absorption frequency bands and anomalous dispersion [87, 88]. Experiments have been extensively reported on the observation of the superluminal or even negative Gaussian pulse transmission over a short distance with the help of dispersive atomic gases [89], photonic crystal band gap structures [90], Bragg gratings [91], optical cavities [92], and MTMs [93] and so forth. Specifically, these experiments were accomplished at a narrow frequency bandwidth with the negative slope of n_r (the second term in Eq. 4.1) dominating n_g, as illustrated in Fig. 4.1(a). However, this frequency dependent n_r inevitably causes dispersion, leading to even smaller distortion-free transmission bandwidth than the superluminal/negative propagation band of the media ($n_g < 1$) itself. Recently, a half-sine wave packet was transmitted through an anomalously dispersive media [94] with a superluminal peak but significant distortion of the beginning and trailing

parts, which is primarily attributed to having more frequency components in the half-sine pulse than those in a Gaussian pulse being transmitted through the anomalously dispersive media. Therefore, significant distortion can be observed for half-sine wave packet whereas Gaussian pulse did not experience apparent distortion [89–93].

To overcome the distortion, a dispersiveless superluminal band is desired. As illustrated in Fig. 4.1(b), a non-Foster loaded material creates $n_g < 1$ by reducing n_r to a less than unity value while keeping it constant $(\partial n_r(\omega)/\partial \omega = 0)$ within the superluminal bandwidth, a necessity for dispersionless superluminal propagation. The resultant n_g is close to n_r as the derivative term diminishes, leading to $n_g = n_r < 1$. Compared to superluminal propagation using an anomalous dispersive gain/absorption band, the non-Foster loaded approach is more promising for providing broader bandwidth which is important for most applications [11, 22, 55, 81–83].

4.2 Observation of the Superluminal Pulse Transmission

4.2.1 Non-Foster waveguide design

Previous researches have demonstrated non-dispersive superluminal propagation with periodic non-Foster loaded waveguides [37, 62, 79]. However, the number of loaded non-Foster circuits was limited, and the superluminal propagation distance was short, due to the instability induced by the negative resistance associated with the non-Foster reactance [80]. To stabilize the non-Foster loaded waveguide and allow more non-Foster circuits for longer propagation distance, a smaller non-Foster reactance is desirable as the associated negative resistance is reduced. Since the non-Foster reactance is used for partially compensating for the intrinsic reactance of the waveguide [37], an air-substrate further re-

duces the required non-Foster reactance value.

With these consideration, we have built a non-Foster loaded waveguide consisting of 38 unit cells over a 3-mm-thick air substrate. As illustrated in Figs. 4.1(c) and (d), the top conductive trace and its ground plane are printed on two 1-mm-thick substrates (Rogers RO4003C, $\varepsilon_r = 3.55$) respectively and separated by a 3-mm air gap, forming an air-substrate MLine. The non-Foster loads are mounted on the other side of the substrate with the ground plane and connected to the MLine through vias. The periodicity of the non-Foster load is 30 mm, corresponding to about 1.5-pF intrinsic capacitance per unit cell. Consequently, a -0.5 pF capacitor is capable of generating an equivalent phase velocity of $1.2c$. Due to the fabrication panel size limitation, a U-shape MLine is designed, with 16 unit cells on the two parallel straight sections, and 8 unit cells on the curved part. The total length of the waveguide is 1200 mm, corresponding to 0.2λ at the central frequency.

The -0.5 pF non-Foster circuit is designed with discrete transistors based on a NIC circuit [43]. A constant measured -0.5 pF is achieved over a bandwidth of 35–70 MHz, as illustrated in Fig. 4.1(e).

A Non-Foster circuit has its impedance/admittance that does not follow Foster's theorem for passive components. The designed -0.5 pF negative capacitor circuit is shown in Fig. 4.2(a), which is based on Linvill's NIC circuit [43]. It is known that positive feedback is necessary to generate a non-Foster impedance. However, negative conductance, G_{NIC}, is also produced by the positive feedback, consequently causing the instability problem. To reduce G_{NIC}, the loop gain of the non-Foster circuit must be reduced, which inevitably decreases the magnitude of the negative capacitance, C_{NIC}. This can be seen from the circuit simulation results shown in Fig. 4.2(b) and (c), where the loop gain is reduced by reducing the biasing voltage at the base of the transistors. This implies that a larger G_{NIC} should
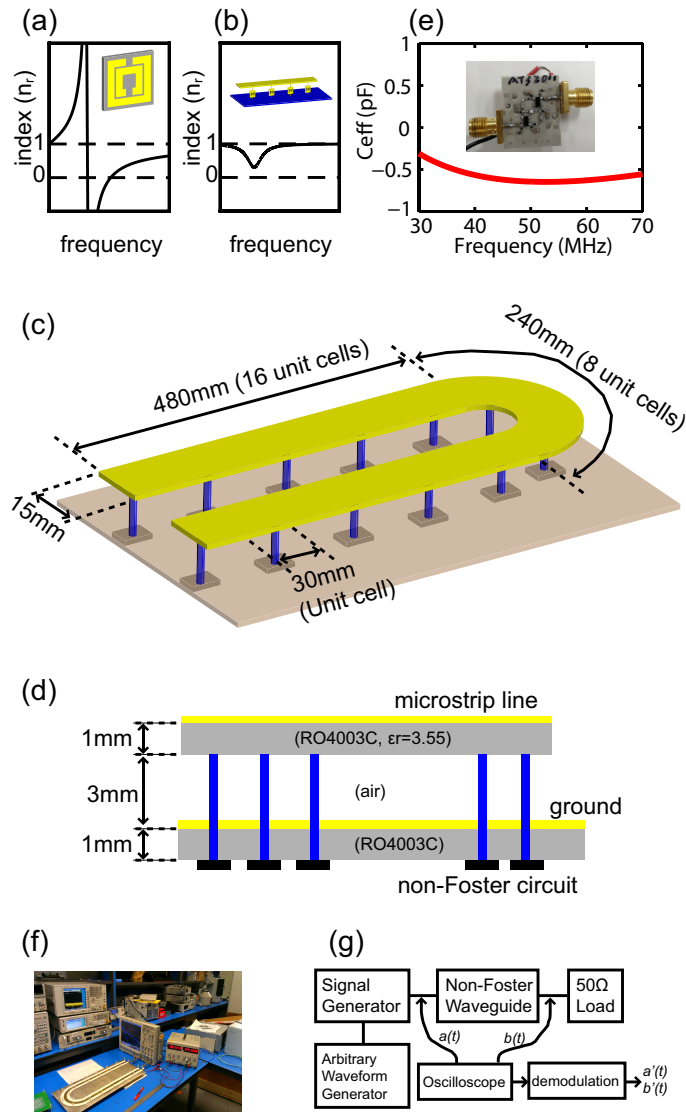
Figure 4.1: The illustration of the non-Foster loaded waveguide. Comparing the refractive index of a MTM based waveguide (a), which achieves superluminal propagation within the band where n_r has negative slope with frequency, inevitably causing dispersion, a non-Foster loaded waveguide (b) produces n_r less than 1, and zero slope with frequency, avoiding unwanted dispersion. The implementation geometry and practical fabrication, including side view (c) and perspective view (d), with detailed dimensions. The measured non-Foster circuits for -0.5 pF capacitors with the measurement sample is shown in (e). The final fabrication is shown in (f). The time domain measurement scheme is illustrated in (g).
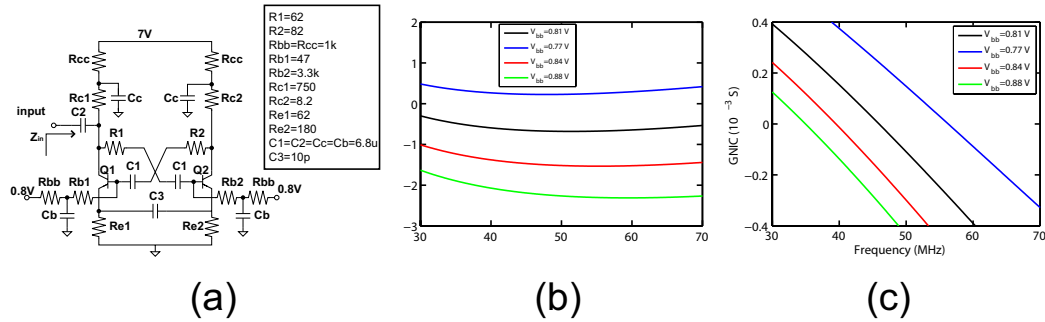
Figure 4.2: A typical Linvill's NIC circuit.(a) presents the circuit schematic, with all component values listed; (b) is the input capacitance with different bias conditions at the base of the transistors; (c) shows the associated input conductance under various bias conditions.

accompany a less negative C_{NIC}, manifesting a trade-off between C_{NIC} and G_{NIC}. The extreme case is that the conductance is always positive, leading to an absolutely stable system, however, the corresponding C_{NIC} will be no longer negative. In this application, in order to improve the stability of the non-Foster circuit loaded waveguide, we make the C_{NIC} negative but very close to zero, so that the corresponding conductance G_{NIC} can be improved, maximumly avoiding the instability. Therefore, a -0.5 pF is designed as Fig. 4.2(a), and its simulated C_{NIC} is shown in Fig. 4.2(b) and (c), which presents a constant -0.5 pF over 30–70 MHz bandwidth. It should be noted that a negative conductance is still present with -0.5 pF when the circuit is biased at 0.81 V (see Fig. 4.2(c)). Nevertheless, the negative conductance is weak enough that the 38 cascaded non-Foster circuits can be stable with a 50Ω load.

The fabricated waveguide shown in Fig. 4.1(f) is expected to produce a 1.2c frequency independent phase velocity or an equivalent n_r of 0.83. It was first tested in frequency domain [37]. The retrieved n_r and n_g were plotted in Figs. 4.3(g) and (h). Fig. 4.3(g) clearly shows a constant n_r near the center frequency of 50 MHz, having a 10% variation within the bandwidth of 42–60 MHz. The measurement results indeed manifest a zero-

slope n_r, which can not be achieved by any gain/absorption line based approaches [89–93].

4.2.2   Superluminal measurement

To clearly observe a superluminal abrupt change of a wave packet, a square wave was modulated to an RF carrier for testing the implemented waveguide. The time domain measurement configuration is illustrated in Fig. 4.1(g). A carrier frequency of 50 MHz is generated by a signal generator (Agilent N5181A), modulated by a 1-μs period 50%-duty-cycle square wave generated by an arbitrary signal generator (Agilent 33210A), and delivered to a 50Ω load through the non-Foster loaded waveguide. The input $a(t)$ and output $b(t)$ waveform are sampled with an oscilloscope (Agilent MSO7104B). Subsequently, the square wave is demodulated from sampled $a(t)$ and $b(t)$, and denoted as $s(t)$ and $r(t)$.

Figs. 4.3(a) and (b) present part of the sampled signals (with carrier) and demodulated waveforms (with carrier removed) at both input and output. The expended details of 1-cycle are presented in Figs. 4.3(c) and (d), clearly demonstrating the resemblance of the input and output waveforms, and consequently, little distortion introduced by the non-Foster waveguide transmission. In particular, the profiles of $s(t)$ and $r(t)$ are in good agreement in Fig. 4.3(d). Here we note that the ringing effect observed in the magnitude of the waveform is the only distinction between $s(t)$ and $r(t)$, indicating that the higher frequency components are amplified, which will be further explained in the following parts. Nevertheless, little distortion can be seen from the profile of the demodulated pulse waveform. The delay of the carrier frequency and square wave packet are calculated by correlating $a(t)$ with $b(t)$, and $s(t)$ with $r(t)$, respectively. In order to avoid the inaccuracy of the time domain measurement, a set of data are selected from the total 25-μs-long sampled waveforms by using a 10-μs window and sliding it every 0.7-μs distance (see Fig. 4.3(b)). Note
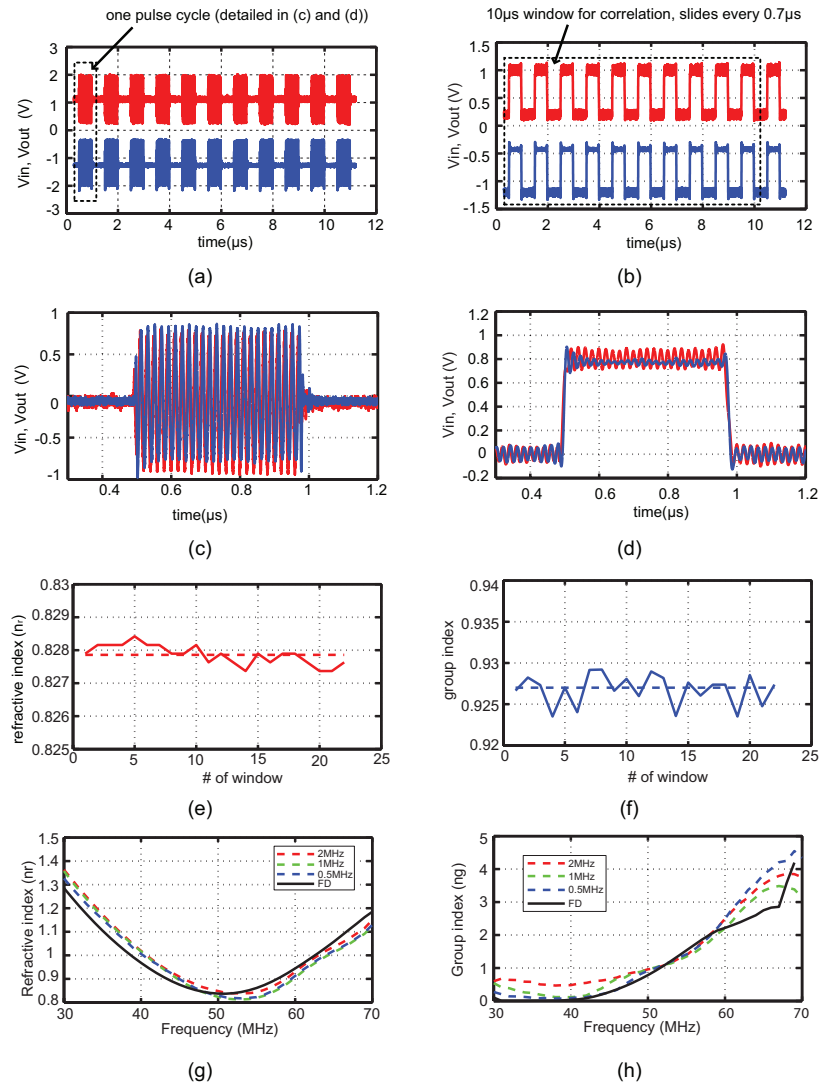
Figure 4.3: Measurement setup and data sampling for calculating the index. The sampled modulated waveforms at the input and output (a) and the demodulated wave packets (b) are detailed in (c) and (d), respectively. A 10-μs data at input and output are windowed from the total 25-μs data and correlated to find the delay for carrier (e) and square pulse (f). The index n_r (g) and group index n_g (h) are measured with carrier frequency ranging from 30–70 MHz, and compared to the frequency domain measurement results. For (a)–(d), blue curves represent waveforms at input, and red color is for output.

that n_r and n_g are related with the delay of the sampled and demodulated waveforms as shown in Figs. 4.3(e) and (f). Here it is observed that the averaged n_r for all sliding windowed samples is 0.828, and n_g is 0.926, both being smaller than unity, which indicates the simultaneously superluminal phase and group velocity.

In addition, n_r and n_g with different carrier frequencies ranging from 30 MHz to 70 MHz and different square pulse width (0.5μs, 1μs, 2μs,) are measured and compared in the frequency domain measurements as shown in Figs. 4.3(g) and (h). Great consistency between the time and frequency domain measurement can be observed, confirming the validity of the measured superluminal propagation results.

Compared to the distorted waveform in [94], distortion has been significantly reduced primarily because most frequency components of the square wave travel with the same velocity in the proposed non-Foster loaded waveguide, whereas the half-sine wave in [94] experienced different delays for different frequency components in the MTM based medium. This indeed reveals the advantage of the non-Foster loaded waveguide to the gain/absorption line based approaches.

Furthermore, tunability of the superluminal propagation is achieved by varying the biasing voltage. Fig. 4.4(a) shows the experimentally obtained n_r with the non-Foster circuits' biasing voltage ranging from 0.74V to 0.78V. The larger biasing voltage results in more negative non-Foster capacitance, and consequently leads to the smaller n_r. The variation of the minimum n_r as a function of the biasing voltage is presented in Fig. 4.4(b), demonstrating a 0.6 (fast wave) to 1.1 (slow wave) tuning range of n_r.

In summary, we have developed a 1200 mm non-Foster loaded waveguide with 38 unit cells, which, to our best knowledge, is the longest non-Foster loaded waveguide and contains the largest number of the non-Foster unit cells. Relying on such design, the
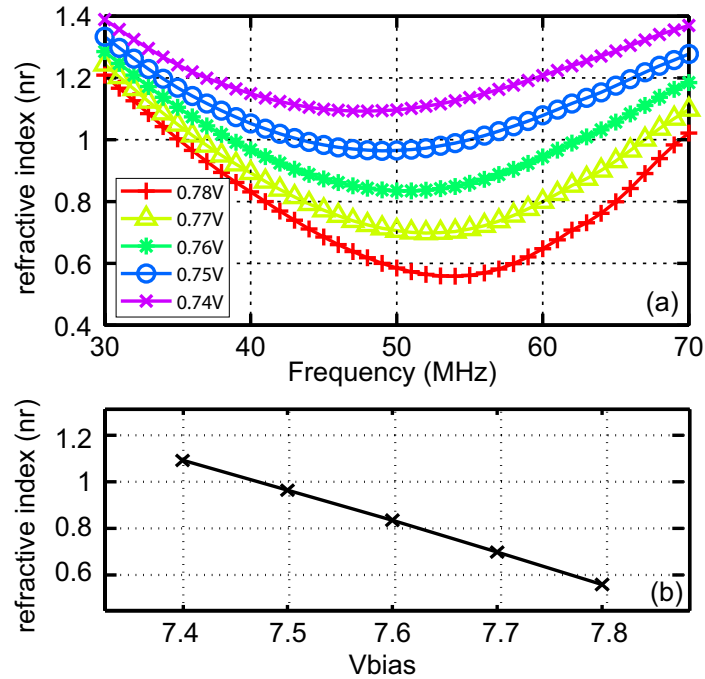
Figure 4.4: The tunability of the non-Foster loaded waveguide. By varying the biasing voltage, the refractive index n_r can be tuned (a), and the disperionless n_r versus biasing voltage is presented in (b).

retrieved n_r indeed manifests a zero slope over bandwidth of 42–60 MHz, about 36% fractional bandwidth (FBW), implying that all frequency components travel with almost the same velocity, which is different from gain/absorption line approaches [89–93]. In addition, despite the fact that the spectrum of a square pulse is broader than the Gaussian pulse and even half-sine waveform of previous works, negligible distortion was found by comparing the waveforms at the input and output of the non-Foster loaded waveguide, further confirming the advantage of the non-Foster loaded waveguide.

4.3 Theoretical Limitation

Although the observation of the non-dispersive superluminal propagation is demonstrated in this work, it still follows Einstein's special relativity and causality [37], in other

words, no signal can travel so fast that the end of a pulse transmitted through a superluminal medium for a certain distance emerges earlier than the beginning of the same pulse traveling in vacuum with the same distance (i.e. the advanced time of the superluminal pulse is larger than the pulse duration of the same pulse in vacuum). Garrett [87] has demonstrated the validity of superluminal propagation in an anomalously dispersive gain/absorption medium with a limited distance. Here, we further this theory and demonstrate the validity of the non-Foster loaded waveguide based superluminal propagation, and address its distance limitation by limiting the pulse advance in terms of the transmitted pulse duration.

4.3.1 Mathematical derivation

Assume a narrow band signal $s(t)$, whose bandwidth is denoted as bw, is transmitted through a carrier $e^{j\omega_c t}$ ($bw \ll \omega_c$). Thus, the transmitted waveform is

$$a(t) = s(t)e^{j\omega_c t}, \tag{4.2}$$

and its Fourier transformation is

$$A(\omega) = S(\omega - \omega_c), \tag{4.3}$$

where $S(\omega)$ is the spectrum of $s(t)$. After passing through an L-meter-length non-Foster loaded medium that is described by a transfer function $H(\omega)$, the output signal in the frequency domain is

$$B(\omega) = A(\omega)H(\omega), \quad (|\omega| < bw). \tag{4.4}$$

and the demodulated output signal is

$$R(\omega) = B(\omega + \omega_c) = A(\omega + \omega_c)H(\omega + \omega_c) = S(\omega)H(\omega + \omega_c), \quad (|\omega| < bw). \quad (4.5)$$

where $H(\omega)$ is expressed as

$$H(\omega) = e^{-\frac{L}{c} \cdot \omega n(\omega)}, \quad (4.6)$$

with $n(\omega)$ being the refractive index of the non-Foster loaded media. Therefore,

$$R(\omega) = S(\omega)e^{-j\frac{L}{c} \cdot (\omega + \omega_c)n(\omega + \omega_c)}, \quad (|\omega| < bw). \quad (4.7)$$

Owing to the narrow bandwidth $bw \ll \omega_c$, $(\omega + \omega_c)n(\omega + \omega_c)$ can be expanded at ω_c by Taylor series, and approximated by neglecting all the higher order terms, as

$$(\omega + \omega_c)n(\omega + \omega_c) \approx \omega_c n(\omega_c) + \omega[n(\omega_c) + \omega_c n'(\omega_c)]. \quad (4.8)$$

Thus, Eq. 4.6 can be further derived as

$$
\begin{aligned}
R(\omega) \quad &\approx S(\omega)e^{-j\frac{L}{c} \cdot \omega_c n(\omega_c)}e^{-j\frac{L}{c}\omega[n(\omega_c) + \omega_c n'(\omega_c)]} \\
&= S(\omega)e^{-j\frac{L}{c} \cdot \omega_c n(\omega_c)}e^{-j\frac{L}{c}\omega[n_r(\omega_c) + \omega_c n'_r(\omega_c)]}e^{-\frac{L}{c}\omega[n_i(\omega_c) + \omega_c n'_i(\omega_c)]}, (|\omega| < bw)(4.9)
\end{aligned}
$$

As mentioned in previous section, the non-Forster loaded fast wave waveguide produces a refractive index that has a flat slope at the center frequency of its superluminal band $(\partial n_r(\omega)/\partial \omega|_{\omega_c} = 0)$ and converges to 1 at infinite frequency. Taking these features,

the index of the non-Foster loaded waveguide is assumed with the basis function

$$n_r = 1 - \frac{\frac{n_{r0}}{BW}}{\left(\frac{\omega - \omega_c}{BW}\right)^2 + 1},$$ (4.10)

and its imaginary part is derived from the Hilbert transformation of n_r to enforce causality [95], as

$$n_i = -\frac{\left(\frac{n_{r0}}{BW}\right)\left(\frac{\omega - \omega_c}{BW}\right)}{\left(\frac{\omega - \omega_c}{BW}\right)^2 + 1}.$$ (4.11)

In both Eqs. 4.10 and 4.11, ω_c is the center frequency, at which n_r reaches its minimum value. In addition, since the derivative of n_r at ω_c is zero, the group index, as defined in Eq. 4.1, is equal to the refractive index number at the center frequency, denoted as

$$n_{g0} = n_r(\omega_c) = 1 - \frac{n_{r0}}{BW}.$$ (4.12)

n_{g0} is determined by the parameter n_{r0}/BW, where BW is the bandwidth where n_r is half way between 1 and n_{g0}. Furthermore, it is easy to derive

$$n_r(\omega_c) = 1 - \frac{n_{r0}}{BW} = n_{g0}, \quad n_i(\omega_c) = 0,$$ (4.13)

and

$$n_r'(\omega)|_{\omega_c} = 0, \quad n_i'(\omega)|_{\omega_c} = -\frac{n_{r0}}{BW} \cdot \frac{1}{BW} = -(1 - g_{g0}) \cdot \frac{1}{BW}.$$ (4.14)

By substituting Eqs. 4.13 and 4.14 to Eq. 4.9,

$$R(\omega) = S(\omega)e^{-j\frac{L}{c}\cdot\omega_c n(\omega_c)}e^{-j\frac{L}{c}\omega\cdot n_{g0}}e^{\frac{L}{c}\omega\cdot\omega_c(1-g_{g0})\frac{1}{BW}}, \quad (|\omega| < bw), \tag{4.15}$$

and the time domain output signal is

$$r(t) = \int_{-bw}^{bw} R(\omega)e^{j\omega t}d\omega. \tag{4.16}$$

Among the three exponential terms in Eq. 4.15, the first one is a constant number, which does not contribute any distortion to the output signal. The second term corresponds to a phase modulation. In particular, this linearly frequency dependent phase modulation results in a constant time delay in the time domain, as $\tau_g = \frac{L}{C}\cdot n_{g0}$, which explicitly implies that n_{g0} represents the group velocity. The third exponential term in Eq. 4.15 represents a frequency dependent amplitude modulation, which introduces the distortion to the signal $R(\omega)$. As the propagation distance L increases, the distortion grows exponentially, and eventually, the output signal $r(t)$ will no long represent the original input signal $s(t)$. Therefore, there must be a distance limitation, which limits the distortion term. Thus, we defined the power difference between the distortion term and ideal amplitude modulation, as

$$P_\Delta = \int_{-bw}^{bw} \left(e^{\frac{L}{c}\omega\cdot\omega_c(1-g_{g0})\frac{1}{BW}}\right)^2 d\omega - \int_{-bw}^{bw} (1)^2 d\omega. \tag{4.17}$$

Let

$$K = 2\frac{L}{c}\cdot\omega_c(1-g_{g0})\frac{1}{BW}, \tag{4.18}$$

Eq. 4.17 becomes

$$
\begin{aligned}
P_\Delta &= \int_{-bw}^{bw} e^{K\omega} d\omega - \int_{-bw}^{bw} (1)^2 d\omega \\
&= \frac{1}{K}(e^{bwK} - e^{-bwK}) - 2bw.
\end{aligned}
\tag{4.19}
$$

As discussed above, P_Δ should be limited so that the output signal is not distorted too much to be recognized as the original signal. However, there is not a straightforward approach to quantitatively find the limitation. Here, we test P_Δ with respect to N times the ideal integral power, as

$$
P_\Delta = N \times \int_{-bw}^{bw} (1)^2 d\omega, \quad (N > 0),
\tag{4.20}
$$

which leads to

$$
(e^{bwK} - e^{-bwK}) = 2(N+1)bwK.
\tag{4.21}
$$

The solution for $bw \cdot K$ can be found by graphic method shown in Fig. 4.5(a). Then a testing Gaussian pulse (with a -40 dB bandwidth of 20 MHz),

$$
s_{test}(t) = e^{\frac{(t-\tau)^2 \cdot (2\pi bw)^2}{16\ln(10^{bwr/20})}}, \quad (\tau = 20 \times 10^{-6}, bw = 20 \times 10^6, bwr = -40),
\tag{4.22}
$$

is used for passing through a testing system function defined as the third exponential term in Eq. 4.15, i.e.

$$
\begin{aligned}
H_{test}(\omega) &= e^{\frac{L}{c}\omega \cdot \omega_c(1-g_{g0})\frac{1}{BW}} \\
&= e^{\omega K/2}.
\end{aligned}
\tag{4.23}
$$
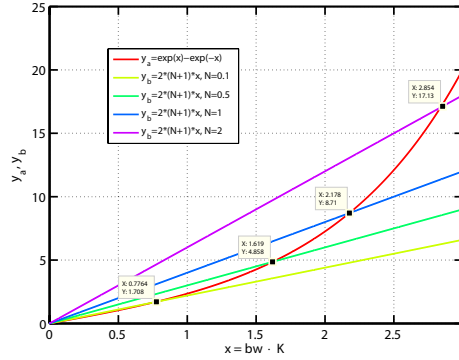
Figure 4.5: The solution $bw \cdot K$ of the Eq. 4.21 based on graphic method. The red curve is the left side of Eq. 4.21. All other curves represent the right side of Eq. 4.21 with $N = 0.1$, 0.5, 1, and 2. The intersection points represents the solution $bw \cdot K$ with parameter of N.
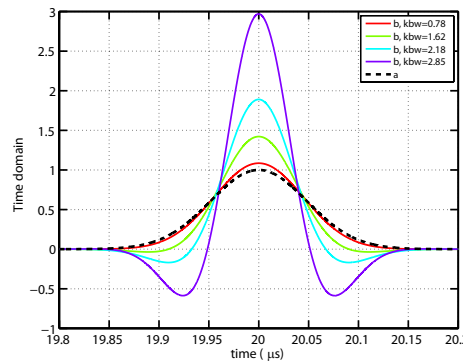
Figure 4.6: The output of a Gaussian pulse defined as Eq. 4.22 through a testing system defined as Eq. 4.23. The parameter K is based on the solution $bw \cdot K$ and the testing Gaussian pulse bandwidth defined in Eq. 4.22. The dotted curve is the input pulse. All other solid curves are the resulting output for different K cases.

The resulting output in the time domain based on different N, $r_{test}(t)$, is compared with $s_{test}(t)$ in Fig. 4.6, from which it is clear to see the distortion when $N > 1$.

Admittedly, $N = 1$ is not the exact limit boundary. Nevertheless, it is enough to see that the boundary must be a finite number as apparent distortion has already been observed when $N = 1$. Thus, he we assume $N = 1$ as the limitation, and in the following discussion, we will demonstrate, although relaxed, leads to the expected conclusion. Therefore, with

$N = 1$, Eq. 4.21 becomes

$$(e^{bwK} - e^{-bwK}) < 4bwK. \tag{4.24}$$

Solving the inequality with the help of Fig. 4.5, it is derived that

$$Kbw = 2\frac{L}{c} \cdot \omega_c (1 - g_{g0}) \frac{1}{BW} \cdot bw < 2.178. \tag{4.25}$$

As n_{g0} is the velocity of the wave packet. $\frac{L}{c} \cdot (1 - n_{g0})$ represents the advanced time of a pulse propagating in the non-Foster loaded superluminal medium compared to that transmitted in vacuum media, denoted as τ_{AD}. In addition, $\frac{1}{2bw}$ equals $\frac{\tau_{pulse}}{2\pi}$, where τ_{pulse} is the pulse duration. Therefore,

$$Kbw = \frac{\tau_{AD}}{\tau_{pulse}} \frac{\omega_c}{BW} \cdot 2\pi < 2.178, \tag{4.26}$$

and thus

$$\frac{\tau_{AD}}{\tau_{pulse}} < \frac{2.178}{2\pi} \cdot \frac{BW}{\omega_c}. \tag{4.27}$$

Base on the causality, n_r must converge to 1 at infinite frequency, so the superluminal bandwidth, BW must be much smaller than the center frequency (also as seen from the bandwidth of the gain/absorption material). Thus,

$$\frac{\tau_{AD}}{\tau_{pulse}} \ll \frac{2.178}{2\pi} = 0.35, \tag{4.28}$$

which explicitly implies that the advanced time of the pulse propagating in a non-Foster

loaded superluminal waveguide must be far less than 35% of the total transmitted pulse duration, indicating that no pulse can travels so fast that the end of the superluminal pulse occurs before the beginning of the same pulse transmitted through vacuum, preserving causality.
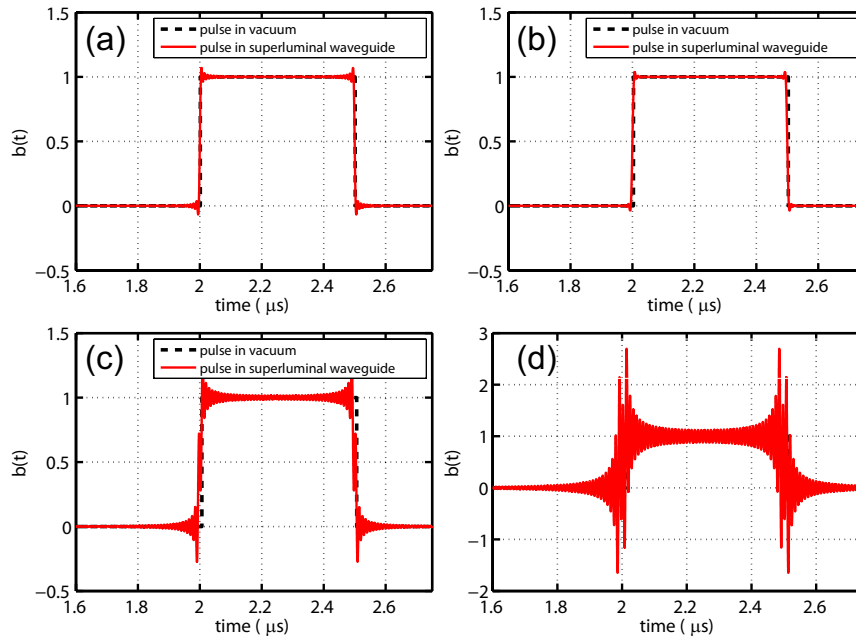
Figure 4.7: The testing case with media distance of (a) 0.5 m, (b) 1 m, (c) 2 m, and (d) 4 m. The testing case is based on the analysis from Eq. 4.2 to Eq. 4.28. The parameters are $\omega_c = 50$ MHz, $BW = 20$ MHz, $n_g = 0.8$, and the tested square pulse has 0.5μs pulse width.

4.3.2 A study case

To verify this demonstration, we numerically calculated a superluminal medium whose refractive index follows Eq. 4.10 and Eq. 4.11 , with $n_{r0}/BW = 0.19$, and $\omega_c/BW = 2.5$, close to the measurement condition. With a 0.5-μs square pulse as $S(\omega)$, the response $b(t)$ is calculated for different distance L as presented in Fig. 4.7. In the above calculation (relying on Eq. 4.28), the maximum distance with acceptable distortion is 262.5m. How-

ever in this case, great distortion appears when the distance is increased to 4m, far less than the theoretically predicted 262.5m. We believe that the P_{add} limitation only quantifies a rough boundary. Nevertheless, it is still confirmed that a superluminal pulse can not be transmitted with an advancement to the light pulse more than a small fraction of the pulse width.

4.4 Summary

In summary, we have introduced a 1200 mm dispersionless superluminal waveguide with 38 non-Foster loads. A refractive index $n_r = 0.83$ is accomplished over a bandwidth of 42–60 MHz. A square wave packet is transmitted through the waveguide without apparent distortion, demonstrating the dispersionless property. A theoretical analysis on the non-Foster based superluminal waveguide is carried out and a limitation on the superluminal advancement in terms of the pulse width is presented.

Chapter 4 is mostly based on the submitted for publication paper: J. Long, D. Sievenpiper, "The Observation of Dispersionless Superluminal Propagation and its Limitation in a Non-Foster Loaded Waveguide," submitted to *Phys. Rev. Lett.*.

Chapter 5

Non-Foster Loaded Broadband Artificial Impedance Surface for Slow Wave Propagation

Different from previous chapters, this chapter is focused on loading the periodic structure with non-Foster impedance for slow wave application – surface wave propagation on an arbitrary impedance surface at UHF band. It is demonstrated that with the help of the loaded non-Foster circuits, two improvements are achieved: (1) the thickness of the HIS is reduced. (2) small dispersion of the HIS is accomplished.

5.1 Background and Motivation

An artificial impedance surface is an EM structure which can be abstracted as a reactive surface impedance boundary, so that it is capable of supporting and interacting with the surface wave propagation [13, 96]. This has inspired many applications, such

as surface wave waveguides [97], RCS reduction [98], surface wave absorbers [15], non-linear MTSs [99] and so forth. It has been further applied to various antenna applications, including artificial magnetic conductors (AMCs) for antenna ground plane [14], antenna reflector [100], and decoupling of multiple antennas [101].

Impedance surfaces have generated so much interest primarily due to their low profile and the simplicity of fabrication, providing superiority over the conventional bulky MTMs. However, artificial impedance surfaces become impractically thick when designed for the UHF band. This can be seen from the basic principle of the HIS [13]. For a typical mushroom structure as shown in Fig. 5.1, it is equivalent to a shunt LC resonant circuit, and the HIS is usually operated near its resonant frequency to obtain a well-bounded surface wave. In particular, the capacitance C and inductance L are contributed by the gap of the adjacent patches and the loop from one patch to the neighboring one through the vias and the ground plane, respectively. Artificial impedance surfaces without vias can also be modeled in the same manner [102]. To make a HIS work at UHF, the LC product should be large enough for resonance at hundreds of megahertz frequency. Using a large C is not a good approach, since it results in larger quality factor, Q, consequently, reducing the bandwidth. In contrast, sufficient L can be realized by increasing the thickness of the HIS, which is a possible approach and is even helpful in producing more bandwidth, nevertheless, this may lead to a thick structure that is no longer practical. Therefore, there is a trade-off between the impedance surface thickness and the bandwidth, limiting the artificial impedance surface applications in the UHF band. In addition, the reactive impedance is always frequency-dependent near the resonance, causing dispersion and consequently further limiting the bandwidth. Thus, it is necessary to find a solution for designing a low-profile and low-dispersion artificial impedance surface in the UHF band.
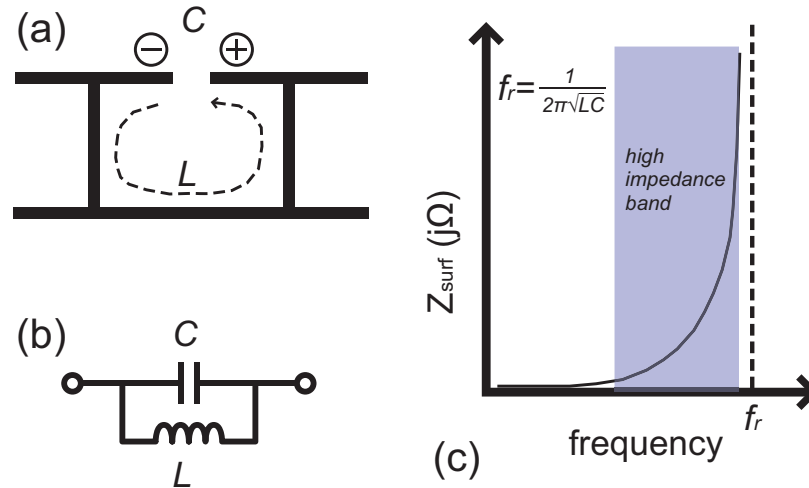
Figure 5.1: The principle of the HIS.

Many efforts have been directed at mitigating the trade-off between the thickness and the bandwidth. Resistively loading a low-profile impedance surface is helpful to obtain broadband absorbers [103, 104], but this approach only works for absorber designs which are intended to absorb/attenuate the incoming waves. Tunable/reconfigurable HIS is another possible solution for designing a thin HIS that is capable of covering a large frequency bandwidth by continuously tuning the loaded elements (usually diodes) [105, 106]. However, this method does not provide wide instantaneous bandwidth as only small bandwidth can be achieved at each configuration. Alternatively, non-Foster loading is promising, since it has been demonstrated in many broadband applications [33, 37, 65, 78, 79, 107–109]. For example, a broadband AMC has been measured in a coaxial transverse electromagnetic (TEM) waveguide by loading with non-Foster negative inductors to the impedance surface [107]. Although bandwidth is improved, the surface still has in-band dispersion, i.e. frequency-dependent surface impedance. Our previous simulation results showed that a combination of negative inductor and capacitor can further reduce the dispersion [109], leading to a broadband reflection-type phase shifter.

In this chapter, we extend the non-Foster loading approach [38] and present a systematic synthesis method, demonstrating that a frequency-dependent non-Foster type impedance is able to accomplish a low-profile artificial impedance surface and also reduce the dispersion of the well-bounded surface wave propagation. Starting from a conventional 5-mm-thick impedance surface resonating at over 1 GHz, an optimized non-Foster type frequency-dependent impedance, which is capable of producing a constant surface wave propagation index, is synthesized. The required non-Foster load, a shunt combination of -2.8 pF $||$ -3.6 nH, is designed and integrated with the thin artificial impedance surface. The near-field measurement of the non-Foster impedance loaded surface presents a constant surface wave index of 1.5, corresponding to a 420 $j\Omega$ surface impedance, over 450–800 MHz, a FBW of 56%. By varying the biasing voltage of the non-Foster circuit, the achieved surface impedance can be tuned from 250 $j\Omega$ to 420 $j\Omega$, while maintaining the low dispersion and the same bandwidth.

The chapter is organized as follows: Sec. 5.2 presents the synthesis approach for determining the desired non-Foster impedance in detail. An artificial impedance surface with such synthesized non-Foster impedance is demonstrated by both eigen and driven mode simulations in Sec. 5.3. Sec. 5.4 describes the non-Foster circuit design and the loaded impedance surface fabrication, and the measurement results are detailed and discussed in Sec. 5.5. Sec. 5.7 concludes this chapter.

5.2   Synthesis of The Non-Foster Impedance Loads

The primary goal of this design is to achieve a low-profile and low-dispersion artificial impedance surface for surface wave propagation in the UHF band. As an example for demonstrating the synthesis algorithm, we design a low-profile impedance surface sup-

porting transverse-magnetic (TM) surface wave with refractive index of 1.5 around 500 MHz.

At first, a conventional thin square patch based impedance surface structure is chosen, as illustrated in Figs. 5.2(a) and (b). The dimension of the unit cell is 50 mm, with a 47-mm square patch and 3-mm gap between adjacent patches. The thickness of the Rogers TMM6 substrate ($\varepsilon_r = 6$) is 5 mm. In this design, we are focused on TM surface waves. The eigen mode simulation configuration and its resulting dispersion curve is presented in Fig. 5.2(c). Master and slave boundaries are used in the eigen mode simulation. The top face of the tall air box is set as a perfect electric conductor boundary for expediting the simulation while maintaining accuracy since the surface wave is well confined near the surface, and exponentially decays away from the surface.

The dispersion diagram in Fig. 5.2(c) implies that the resonant frequency is about 1.2 GHz, and it presents high impedance from about 1–1.2 GHz, which is much higher than our target of 500 MHz. Since it is well-known that loading a capacitance between the patches can reduce the resonant frequency, enabling the surface to work at a lower band [13], a lumped capacitance in the gap implemented wwith RLC boundary in HFSS is added and swept from 10 pF to 100 pF, as shown in the inset of Fig. 5.3. The eigen mode simulation results of the sweep are summarized in Fig. 5.3, from which it is evident that the resonant frequency is reduced by the loading capacitor. Furthermore, it is observed that different dispersion curves have been achieved with different loaded capacitance. In particular, the greater the loaded capacitance, the lower the resonance frequency.

With a goal of providing a dispersion curve with a constant index of 1.5, as shown by the dashed line in Fig. 5.3, the points on the targeted ideal $n = 1.5$ line intersecting with the swept dispersion curves, such as point A and B in Fig. 5.3, are of the most importance.
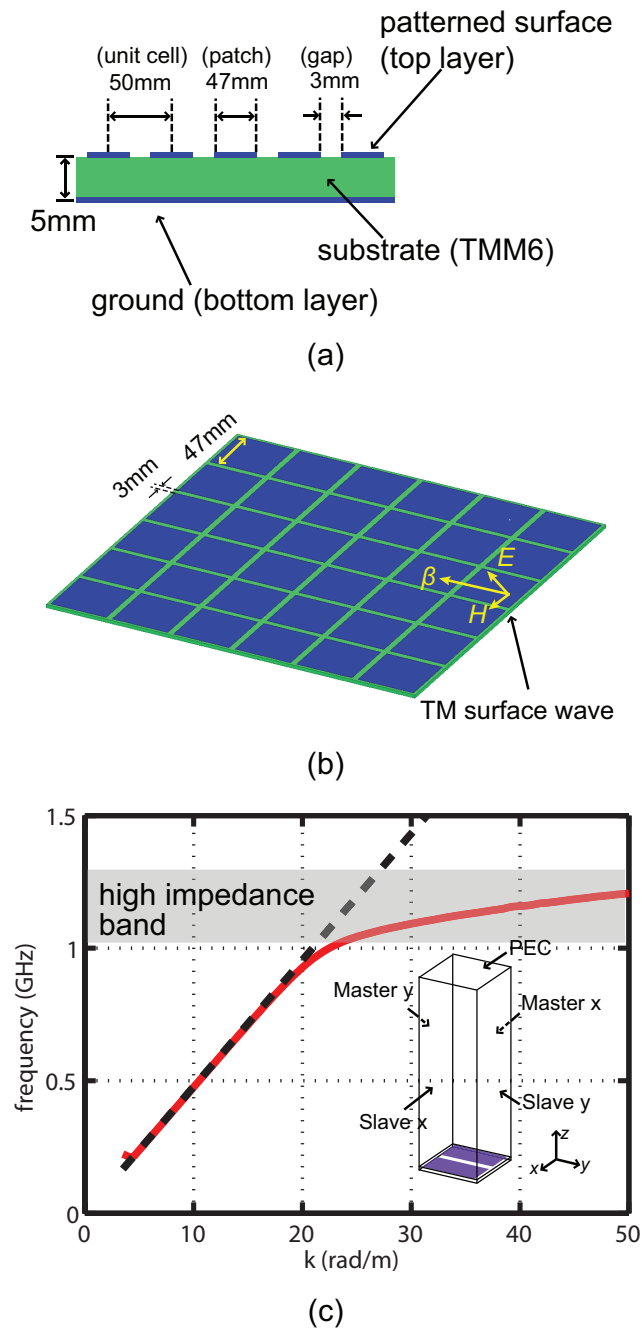
Figure 5.2: The low-profile impedance surface dimension and its dispersion diagram without any loads. (a) and (b) illustrates the dimensions of the unit cell. (c) presents the dispersion diagram, with the description on the eigen mode simulation configuration.
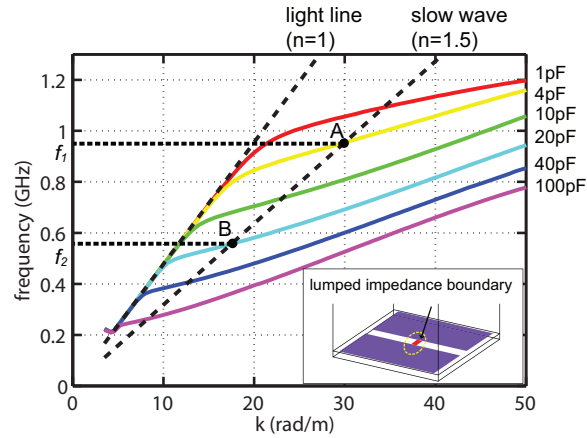
Figure 5.3: Impedance surface with passive capacitance swept from 1 to 100 pF. Points A and B are the intersection of the swept dispersion curve and the ideal $n = 1.5$ slow wave dispersion curve.

Particularly, point A indicates that a 10-pF capacitor is needed to load the impedance surface for achieving a $n = 1.5$ index at frequency f_1. Similarly, point B means that a 20-pF load is demanded for f_2. This can be further interpreted as how much susceptance is required for the load to achieve a $n = 1.5$ index at each frequency. Therefore, based on all the intersecting points, it is possible to derive a susceptance–frequency table to describe this required frequency dependent load, with which the resulting dispersion curve of the loaded HIS passes through all of the intersecting points, lining up with the targeted ideal $n = 1.5$ dispersion curve. Since the intersecting points range from 200 MHz to 1000 MHz, the synthesized dispersion curve can be expected to overlap with the targeted $n = 1.5$ curve over the bandwidth of 200–1000 MHz.

Such frequency-dependent susceptance is plotted as the solid curve in Fig. 5.4. Two points can be observed from Fig. 5.4: (1) the slope of the susceptance versus frequency is negative, clearly implying this synthesized impedance is a non-Foster impedance [26], and (2) it can be fitted by a shunt circuit of -5 nH and -3 pF (dashed curve in Fig. 5.4), indicating that only a single non-Foster element such as a negative inductor is not enough
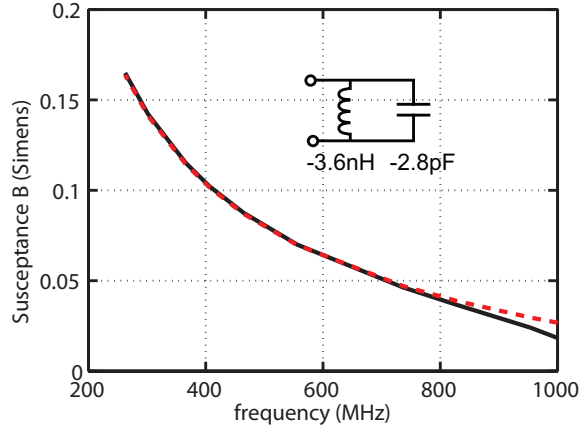
Figure 5.4: The synthesized loading impedance (black solid curve) and its equivalent non-Foster element combination (red dotted curve).

for reducing the dispersion. With the same manner the frequency-dependent non-Foster impedance for $n = 1.2$ is also derived and summarized in Table. 5.1.

Table 5.1: Synthesized non-Foster lumped equivalent circuit

index	Z_{surf}	shunt L	shunt C
$n = 1.2$	250 $j\Omega$	-4.1 nH	-3.4 pF
$n = 1.5$	421 $j\Omega$	-3.6 nH	-2.8 pF

To summarize this section, a frequency-dependent load is synthesized by finding the intersecting points of the swept dispersion curves and the targeted ideal curves [65]. This load is identified as a non-Foster impedance.

5.3   Simulation on The Non-Foster Loaded Surface

As a demonstration, the 5-mm-thick impedance surface loaded with the previously synthesized frequency-dependent non-Foster impedance is simulated. Two simulation approaches are adopted: eigen mode simulation and driven mode simulation.

The eigen mode simulation model is the same as the inset of Fig. 5.3, with the

lumped RLC boundary being configured as -3.6 nH $||$ -2.8 pF. The driven mode simulation model is illustrated in Fig. 5.5(a). A 1-meter-long non-Foster loaded surface composed of 20 unit cells is placed in a tall air box with three faces (top, front and end face) configured as radiation boundaries. A perfect magnetic conductor is used for both left and right face since only the TM surface wave is of interest. The non-Foster load in each unit cell is realized by a lumped boundary. A parallel plate waveguide is utilized for exciting a vertically polarized plane wave, which is coupled to the surface as a TM surface wave mode. The phase progression along the longitudinal direction is extracted, from which the propagation constant at the excitation frequency is calculated. The excitation is swept in the frequency domain so that the dispersion information is obtained.

The simulated dispersion diagram from both eigen and driven mode simulations are presented in Fig. 5.5(b), where both results are consistent, confirming an almost constant $n = 1.5$ dispersion curve over a wide bandwidth, demonstrating very low-dispersion surface wave propagation is accomplished. It should be noted that the eigen mode simulation has a sharp bend at about 800 MHz, which is because of a transverse electric wave mode coming into the passband. In contrast, the dispersion from the dirven mode simulation extends over 500 MHz, because the polarization of the excitation and the perfect magnetic conductor boundary condition prevent the incident wave from coupling into the transverse electric surface wave mode. Thus, it is demonstrated that with the synthesized non-Foster impedance load, the 5-mm-thick impedance surface is able to support a wide band dispersion-reduced $n = 1.5$ surface wave propagation.
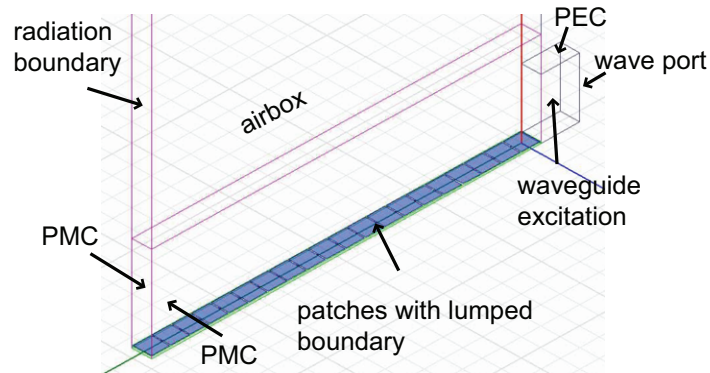
(a)
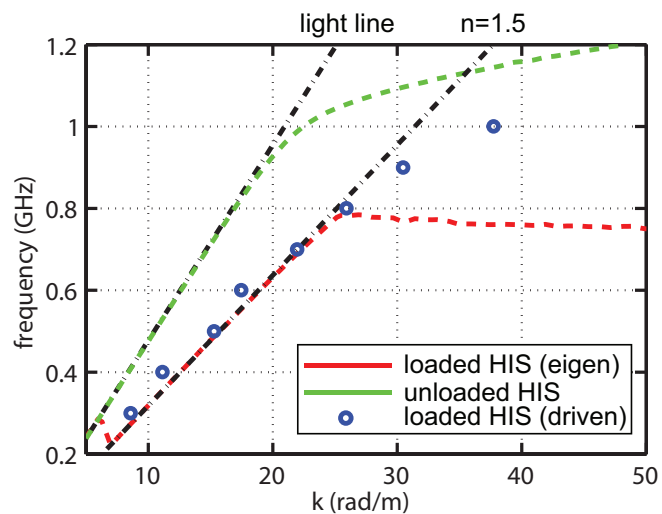
(b)

Figure 5.5: Simulation demonstration of the impedance surface loaded with the synthsized impedance. (a) presents the driven mode simulation configuration. (b) shows the simulated results for both driven and eigen mode simulation, which is compared to the light line and the targeted $n = 1.5$ slow wave line. The dispersion curve of the unloaded impedance surface is appended for comparison.

5.4   Experimental Implementation

5.4.1   Non-Foster impedance

The synthesized non-Foster impedance is designed based on Linvill's NIC [43]. In particular, since the circuit is intended to be loaded between the two adjacent patches, which possesses high impedance at low frequencies, the OCS type NIC is adopted for the stability consideration. The circuit schematic and the electronic component values are illustrated in Fig. 5.6(a). Two transistors (Avago AT32011) are cross coupled, providing positive feedback. An inductor is connected between the collectors of the two transistors. This inductor, along with the biasing networks at the collectors, forms the parallel LC circuit for impedance conversion. In the OCS configuration, the output is at the two emitters, where two resistors are used for DC biasing. In addition, resistors in the cross coupled loop are for controlling the loop gain for stability.

The non-Foster circuit is designed and fabricated on a 10×10 mm^2 PCB with 0.8-mm-thick Rogers RO4003C ($\varepsilon_r = 3.4$) substrate as shown in the inset of Fig. 5.6(b). All the traces in the layout are kept short so as to avoid unwanted parasitics. The parasitics of the layout are modeled and extracted from HFSS for co-simulation, for predicting the freqeuncy domain performance and stability. The simulation first passed the transient test for stability, and we then calculated the input impedance with the frequency domain simulation. The fabricated sample is also tested with a signal analyzer and oscilloscope to ensure stability, and then measured in the frequency domain. The result after deembedding is shown in Fig. 5.6(b), where it is confirmed that the fabricated non-Foster circuit possesses a susceptance very close to what is synthesized. In addition, by tuning the biasing voltage, both impedances needed for constant index of $n = 1.2$ and $n = 1.5$ are realized over a wide

(a)

(b)
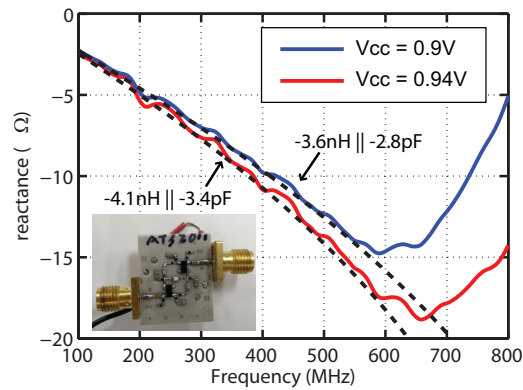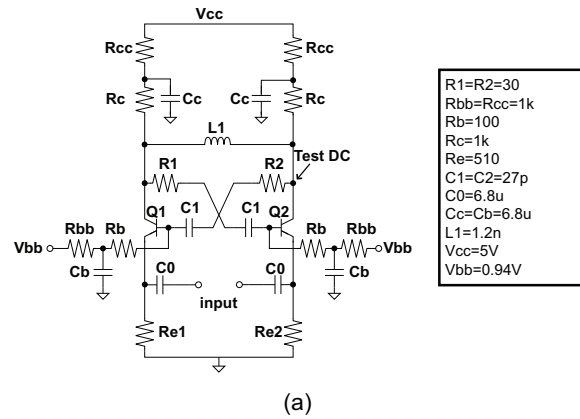
Figure 5.6: The designed non-Foster circuit for the synthesized impedance. The schematic is illustrated in (a), and its measurement results at 0.9V and 0.94V are compared to the synthesized impedance in (b). The measurement sample is shown in the inset of (b).

bandwidth.

5.4.2 Loaded impedance surface fabrication

The entire non-Foster impedance loaded surface is designed as shown in Fig. 5.7, where Fig. 5.7(a) illustrates how the surface and non-Foster circuit are configured. The unit cell is the same as depicted in Fig. 5.2(a). The non-Foster circuit is fabricated and attached to the other side of the impedance surface. The circuits and artificial impedance surface are sharing the same ground plane and connected through vias, so that not only

are the parasitics minimized, but also the circuit components are immune to the impact from the impedance surface side, and the fabrication process is simplified as all electronic components are surface mounted on the bottom side. The ground is configured on the second layer from the top, providing an intact artificial impedance surface structure. The third layer is for DC bias routing, which is also an alternating current (AC) ground. Besides through hole vias connecting the non-Foster circuit to the patches, buried vias are used for connecting the ground on the second layer and the power network on the third layer to the non-Foster circuit on the bottom layer. A non-Foster loaded surface consisting of 7×10 unit cells is fabricated as shown in Fig. 5.7(b) and (c).

5.5   Measurement

The fabricated non-Foster loaded artificial impedance surface is measured with the near field measurement approach, as illustrated in Fig. 5.8. Two fabricated 7×10 unit cell panels are cascaded and put underneath a vertically polarized high impedance probe. A WR10 waveguide is used for exciation with the E-field oriented in the vertical direction. The probe is scanned in the horizontal plane to measure the relative magnitude and phase progression on the surface. When the non-Foster circuit is biased at 0.9V, the measured E_z field distribution at 0.65 GHz is plotted on Fig. 5.9(a), demonstrating that the excited wave from the rectangular waveguide adapter is converted into a surface wave propagating along the surface. The apparent attenuation is due to the loss of the non-Foster loaded surface. The phase progression at the center line (see Fig. 5.9(a)) is extracted, unwrapped and presented in Fig. 5.9(b). To find the propagation constant, the 1st-order linear fit algorithm is used. Provided that the phase progression over this distance has a 1st-order linear fit
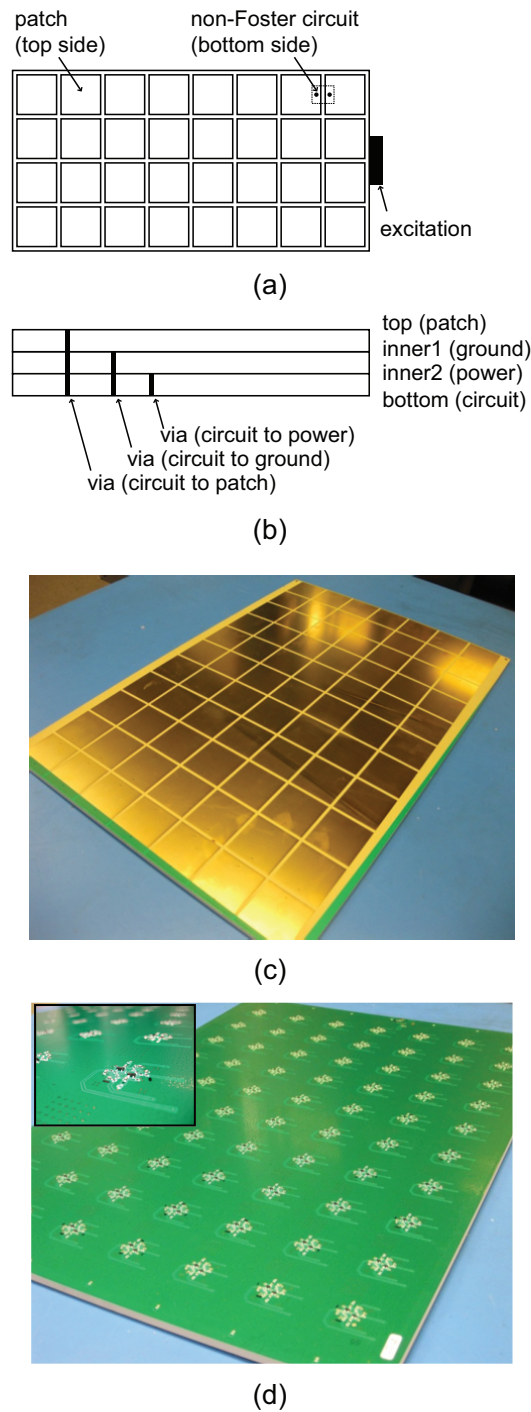
(a)

(b)

(c)

(d)

Figure 5.7: The fabrication of the non-Foster loaded artificial impedance surface (a) and (b) illustrate the entire PCB configuration, (c) and (d) are the top and bottom side of the fabricated sample.
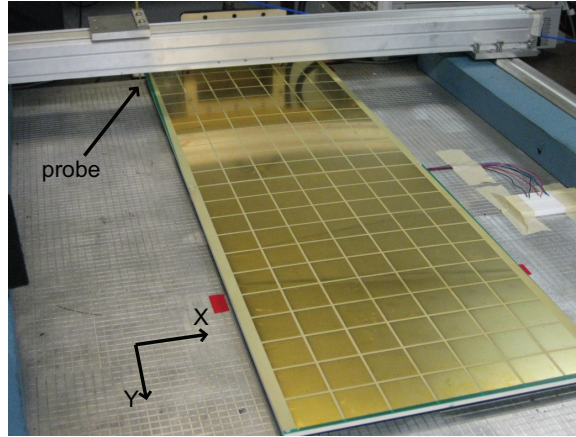
Figure 5.8: The near field measurement setup of the non-Foster loaded artificial impedance surface.

coefficient, p_1, the propagation constant k and refractive index n are

$$k = -P_1, \tag{5.1}$$

and

$$n = \frac{-P_1 \cdot c}{\omega}, \tag{5.2}$$

where c is the speed of light. The surface impedance can be further found from the slow wave propagation index, as [13]

$$Z_{surf} = \eta \sqrt{1 - n^2}, \tag{5.3}$$

where $\eta = 377\Omega$ as the wave impedance in the free space. Thus, $n = 1.5$ is found for the extracted phase progression shown in Fig. 5.9(b), corresponding to 420 $j\Omega$. With the same manner, the refractive indices for frequencies from 400 to 1000 MHz are derived and summarized in Fig. 5.10. Below 400 MHz, it is hard to obtain an accurate phase since the 1-meter long impedance surface is still electrically short at low frequencies.
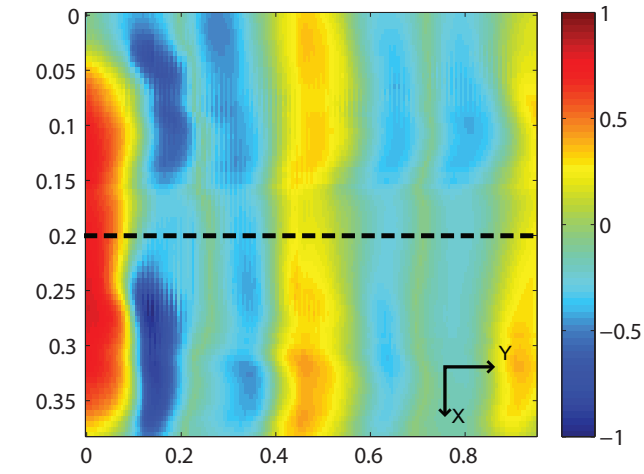
(a)
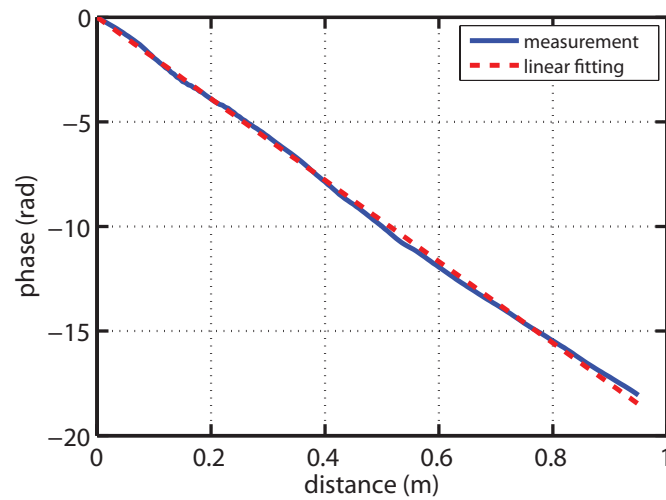
(b)

Figure 5.9: Near field measurement result of the non-Foster loaded artificial impedance surface. (a) presents the normalized near field E_z distribution at 650 MHz. The phase progression at the center (along the dashed line) is extracted, as shown in (b). The 1st order linear fit is applied to calculate its slope and further to derive the refractive index.

Fig. 5.10(a) presents the derived dispersion diagram for biasing of 0.9V (blue) and 0.94V (red) respectively, which clearly shows that both $n = 1.3$ and $n = 1.5$ slow wave conditions have been realized. In particular, the consistency with the ideal $n = 1.3$ and $n = 1.5$ line (dashed lines) for the measured dispersion curves (solid lines) over a wide bandwidth indicates the accomplished slow wave propagation has low dispersion. The bare board without out circuits populated is also measured and the result is shown in Fig. 5.10(a) with red color. It is found that the dispersion curve follows the light line over the entire frequency range below 1 GHz. As aforementioned, the unloaded surface is resonant at around 1.2 GHz. The consistency with the light line below 1 GHz is thus reasonable, confirming the measurement results. Ripples are observed for the measured dispersion curves. This is primarily because of the small size of the impedance surface sample compared to the wavelength and the 1st-order linear fit based algorithm for finding the propagation constant, which causes inaccurate measurements at some frequency points. Nevertheless, the overall performance, from 400 MHz to 1000 MHz clearly shows the predicted trends as expected.

Fig. 5.10(b) shows the refractive index versus frequency, which clearly manifests a wideband constant index of 1 (for unloaded surface), 1.3 (for the impedance surface with non-Foster load biased at 0.94V) and 1.5 (for the surface with non-Foster load at 0.9V). In particular, the achieved indices are constant over the bandwidth from 450 MHz to 800 MHz, a 56% FBW.

5.6   Discussion

The accomplished 450–800 MHz bandwidth is significant. Provided the impedance surface is working at 450–800 MHz with the same 5-mm-thick surface having the same unit cell size loaded by a passive capacitor, based on Fig. 5.3, a 20-pF capacitor is needed, yet
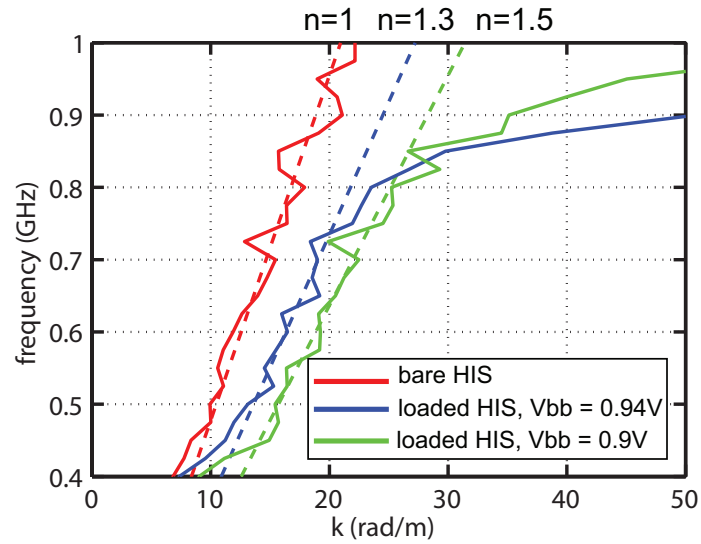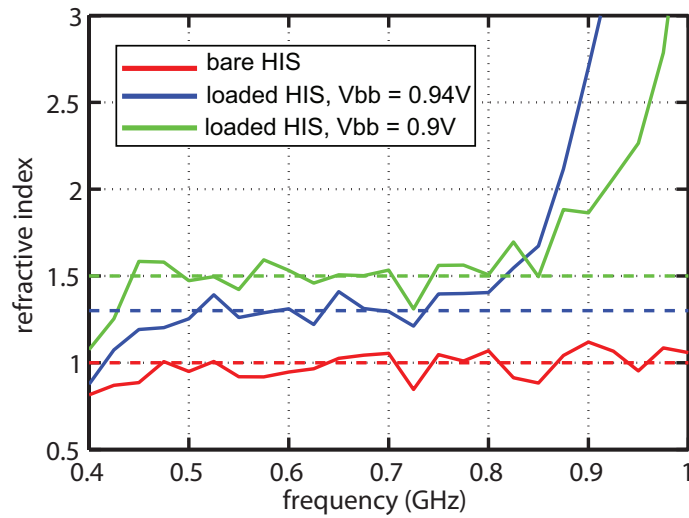
Figure 5.10: The measured dispersion diagram and the measured refractive index. (a) presents the measured dispersion diagram of the bare impedance surface (red), the non-Foster loaded surface at 0.94V (blue) and 0.9V (green). The ideal dispersion curve for $n = 1$, 1.3, 1.5 are appended for comparison. (b) illustrates the refractive index versus frequency.

the bandwidth can not be as large as what is achieved by the non-Foster impedance load. This can be seen from the comparison in Fig. 5.11, where the surface impedance of the non-Foster loaded surface (blue and green curves) are compared to the one obtained from a passive capacitance loaded surface (red curve). Within the shaded region (450–800 MHz), it is clear that the surface impedance achieved by the non-Foster load is much flatter, and covers much larger bandwidth than the passive loading approach.
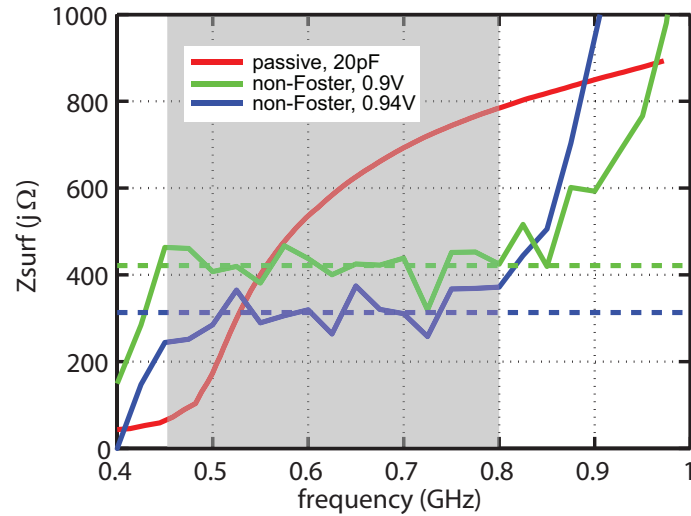
Figure 5.11: The comparison of the impedance bandwidth obtained from passive (red) and non-Foster (blue and green) approaches.

5.7   Summary

To sum up this chapter, we have introduced a low-profile artificial impedance surface whose dispersion is significantly reduced over a wide bandwidth. The approach to accomplish this thin and non-dispersive impedance surface is by loading a frequency dependent non-Foster like impedance to the conventional electrically thin impedance surface unit cells. A systematic algorithm for obtaining the frequency dependent impedance for achieving the dispersion reduced artificial impedance surface is introduced, and it is demonstrated

that a non-Foster impedance is required to control the dispersion. The proposed method is demonstrated with both eigen and driven mode simulations. For experimental demonstration, the synthesized $-2.8\,\text{pF} \,||\, -3.6\,\text{nH}$ circuit is designed as a transistor based NIC circuit and fabricated on the 5-mm-thick impedance surface structure in a back-to-back configuration, forming a multi-layer impedance surface board. The fabricated non-Foster loaded artificial impedance surface is measured with the near field scanner. From the near field distribution, its surface impedance properties are characterized over a wide bandwidth. By extracting and analyzing the phase progression over the surface, constant slow wave propagation indices of 1.3 and 1.5 are measured over a bandwidth of 450–800 MHz, a 56% FBW. Compared to the passive capacitor loaded surface working in the same band, the non-Foster loaded artificial impedance surface possesses significantly larger bandwidth and less dispersion.

Chapter 5 is based on the submitted and published papers: J. Long, and D. Sievenpiper, "UHF Low-Profile Non-Foster Circuits Loaded Dispersion Reduced High Impedance Surface," submitted to *IEEE Trans. Antenna Propag.*; J. Long, and D. Sievenpiper, "Dispersion-reduced high impedance surface loaded with non-Foster impedances," in *Proc. IEEE Antennas Propag. Soc. Int. Symp. (APSURSI)*, Vancouver, Canada, 2015.

Chapter 6

Summary and Future Work

6.1 Summary of Work

It has been demonstrated that the non-Foster impedance is fundamentally different from the passive impedance, which is the reason why it is potentially capable of breaking the theoretical frequency bandwidth limitation, including the limitation for the periodic structures. This thesis starts from the basic theory of the non-Foster impedance, discusses its negative reactance slope with frequency, explains the advantages of the non-Foster impedance in the impedance matching circuits, and presents many associated potential broadband RF/microwave and antenna applications. Specifically, the thesis focuses on the study of the non-Foster loaded periodic fast and slow wave EM structures.

Chapter 2 introduces the fundamental principle of the non-Foster impedance. The properties of the non-Foster impedance are reviewed. Unlike passive impedance, non-Foster reactance monotonically decreases with frequency, which can be further utilized in perfect compensation for the passive reactance, resulting in a significant increase in the frequency bandwidth. Many possible broadband applications are then introduced in Chapter 2.

The thesis continues with an explanation of detailed non-Foster circuit design approaches, including mathematical derivation of the non-Foster input impedance and experimental design examples.

Chapter 3 presents a non-Foster loaded fast wave periodic structure. By periodically loading negative capacitors to a conventional TL, the capacitance per unit length is reduced, so that the effective phase velocity can be boosted to a point that is faster even than the speed of light. An s-parameter and a near-field distribution approaches are adopted to measure the faster-than-light phase velocity, both manifesting fast wave propagation over a relative wide bandwidth at UHF band. The stability and causality are also discussed and demonstrated according to the Kramers–Kronig relation.

In addition to the phase velocity, the group velocity is also observed to be greater than c over the same frequency band. Therefore, Chapter 4 will extend the study on the negative-capacitor loaded waveguide to investigate the possibility of the superluminal pulse propagation. To produce enough time delay for observation, a longer non-Foster loaded waveguide with more non-Foster unit cells is designed. Through such a waveguide, a superluminal propagation delay with negligible distortion is measured and confirmed by both frequency and time domain measurements. Nevertheless, it is demonstrated that the distortion increases with the length of the superluminal waveguide. Consequently, it is concluded that superluminal wave propagation under a certain distortion level is only possible within a distance limitation, thereby ensuring causality.

Chapter 5 presents the non-Foster loaded artificial impedance surface for broadband slow wave propagation. It is found that a non-Foster impedance is needed in order to produce constant surface wave propagation velocity over a wide band. A systematic synthesis approach is proposed. The synthesized impedance — in particular, a shunt negative LC
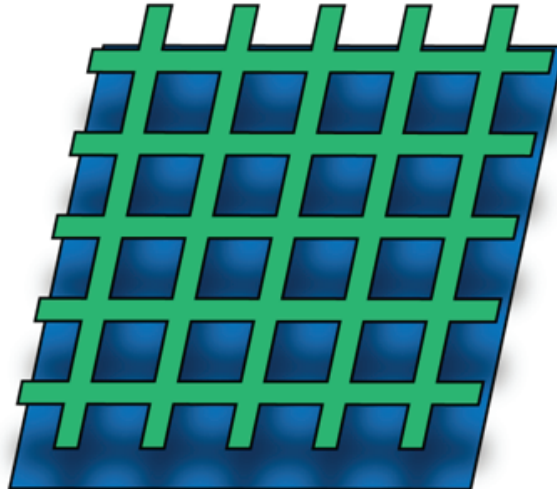
Figure 6.1: An illustration for 2D non-Foster loaded periodic structure. A 2D non-Foster loaded waveguide based on the 1D waveguide presented in Chapter. 3 is used as an example.

circuit — is realized by the same NIC-based non-Foster circuit. A constant slow surface wave propagation index is measured by means of near-field distribution approach.

6.2   Future Work

Regarding the non-Foster circuit, the current design still converts passive electronic components to non-Foster impedance through an NIC circuit, in which the conversion follows a simple function of frequency. Thus, the generated non-Foster impedance behaves like a negative capacitor/inductor or combination of the two. A non-Foster impedance with a more complicated function of frequency would be interesting for future work, because it would give researchers more freedom to match impedance network with a wider bandwidth than in the case of the current design. Also, an integrated circuit process could help improve the operating frequency to gigahertz level. Furthermore, owing to the involvement of the transistors, noise and linearity performance should also be investigated in the future.

In the thesis, a 1D slow and fast wave periodic structures are demonstrated. There

will be more challenges in 2D and 3D design, as shown in Fig. 6.1. However, it is worth studying these, since they provide more freedom to control the wave propagation, especially for anisotropic MTMs and MTSs [23].

In addition, the active loaded periodic structure is not limited to non-Foster impedance loading for broadband applications. It has been demonstrated that periodically loading diodes, rectifiers, and more complex regulating circuits to unit cells result in waveform/power-dependent and self-focusing surfaces [15, 99] that, perhaps, will pave the way for entirely revolutionary intelligent MTMs and MTSs.

Bibliography

[1] N. Engheta and R. W. Ziolkowski, *Metamaterials: physics and engineering explorations*.   John Wiley & Sons, 2006.

[2] J. D. Joannopoulos, S. G. Johnson, J. N. Winn, and R. D. Meade, *Photonic crystals: molding the flow of light*.   Princeton university press, 2011.

[3] R.-B. R. Hwang, *Periodic Structures: Mode-matching Approach and Applications in Electromagnetic Engineering*.   John Wiley & Sons, 2012.

[4] C. Caloz and T. Itoh, *Electromagnetic metamaterials: transmission line theory and microwave applications*.   John Wiley & Sons, 2005.

[5] S. Peng, T. Tamir, and H. L. Bertoni, "Theory of periodic dielect waveguides," *IEEE Trans. Microw. Theory Techn.*, vol. 23, no. 1, pp. 123–133, 1975.

[6] E. Yablonovitch, "Inhibited spontaneous emission in solid-state physics and electronics," *Phys. Rev. Lett.*, vol. 58, no. 20, p. 2059, 1987.

[7] S. John, "Strong localization of photons in certain disordered dielectric superlattices," *Phys. Rev. Lett.*, vol. 58, no. 23, p. 2486, 1987.

[8] D. R. Smith, W. J. Padilla, D. Vier, S. C. Nemat-Nasser, and S. Schultz, "Composite medium with simultaneously negative permeability and permittivity," *Phys. Rev. Lett.*, vol. 84, no. 18, p. 4184, 2000.

[9] R. A. Shelby, D. R. Smith, and S. Schultz, "Experimental verification of a negative index of refraction," *science*, vol. 292, no. 5514, pp. 77–79, 2001.

[10] J. B. Pendry, "Negative refraction makes a perfect lens," *Phys. Rev. Lett.*, vol. 85, no. 18, p. 3966, 2000.

[11] D. Schurig, J. Mock, B. Justice, S. Cummer, J. Pendry, A. Starr, and D. Smith, "Metamaterial electromagnetic cloak at microwave frequencies," *Science*, vol. 314, no. 5801, pp. 977–980, Nov. 2006.

[12] A. V. Kildishev, A. Boltasseva, and V. M. Shalaev, "Planar photonics with metasurfaces," *Science*, vol. 339, no. 6125, p. 1232009, 2013.

[13] D. Sievenpiper, "High impedance electromagnetic surface," Ph.D. dissertation, UCLA, Los Angeles, 1999.

[14] R. F. J. Broas, D. F. Sievenpiper, and E. Yablonovitch, "A high-impedance ground plane applied to a cellphone handset geometry," *IEEE Trans. Microw. Theory Techn.*, vol. 49, no. 7, pp. 1262–1265, 2001.

[15] H. Wakatsuchi, S. Kim, J. J. Rushton, and D. F. Sievenpiper, "Waveform-dependent absorbing metasurfaces," *Phys. Rev. Lett.*, vol. 111, no. 24, p. 245501, 2013.

[16] J. A. Kong, *Theory of electromagnetic waves*. New York: John Wiley and Sons, 1975.

[17] P. A. Kuchment, *Floquet theory for partial differential equations*. Birkhäuser, 2012, vol. 60.

[18] P. W. Milonni, *Fast light, slow light and left-handed light*. CRC Press, 2004.

[19] C. A. Balanis, *Advanced engineering electromagnetics*. Wiley Online Library, 2012, vol. 111.

[20] ——, *Antenna theory: analysis and design*. John Wiley & Sons, 2005, vol. 1.

[21] A. A. Oliner and D. R. Jackson, "Leaky-wave antennas," *Antenna Engineering Handbook*, vol. 4, p. 12, 1993.

[22] J. Long, M. Jacob, and D. F. Sievenpiper, "Electronically steerable antenna using superluminal waveguide and tunable negative capacitors," in *Proc. IEEE Int. Symp. Antennas Propag. Soc. (APSURSI)*. IEEE, 2012, pp. 1–2.

[23] R. Quarfoth, "Anisotropic artificial impedance surfaces," Ph.D. dissertation, UCSD, La Jolla, 2014.

[24] S. Hrabar, I. Krois, and A. Kiricenko, "Towards active dispersionless enz metamaterial for cloaking applications," *Metamaterials*, vol. 4, pp. 89–97, 2010.

[25] R. M. Fano, "Theoretical limitations on the broadband matching of arbitrary impedances," *J. Franklin Institute*, vol. 249, no. 1, pp. 57–83, 1950.

[26] R. M. Foster, "A reactance theorem," *Bell System Technical Journal*, vol. 3, no. 2, pp. 259–267, 1924.

[27] H. Wheeler *et al.*, "Fundamental limitations of small antennas," *Proc. IRE*, vol. 35, no. 12, pp. 1479–1484, 1947.

[28] D. M. Pozar, *Microwave engineering*, 2nd ed. New York: John Wiley and Sons, 1998.

[29] D. F. Sievenpiper, D. C. Dawson, M. M. Jacob, T. Kanar, S. Kim, J. Long, and R. G. Quarfoth, "Experimental validation of performance limits and design guidelines for small antennas," *IEEE Trans. Antennas Propag.*, vol. 60, no. 1, pp. 8–19, 2012.

[30] S. Koulouridis, "Non-foster design for antennas," in *Proc. IEEE Int. Symp. Antennas Propag. Soc. (APSURSI).* IEEE, 2011, pp. 1954–1956.

[31] S. E. Sussman-Fort and R. M. Rudish, "Non-foster impedance matching of electrically-small antennas," *IEEE Trans. Antennas Propag.*, vol. 57, no. 8, pp. 2230–2241, Aug. 2009.

[32] M. M. Jacob, L. Jiang, and D. F. Sievenpiper, "Broadband non-foster matching of an electrically small loop antenna," in *Proc. IEEE Int. Symp. Antennas Propag. Soc. (APSURSI)*, Chicago, IL, Jul. 2012.

[33] M. M. Jacob, J. Long, and D. F. Sievenpiper, "Non-foster loaded parasitic array for broadband steerable patterns," *IEEE Trans. Antennas Propag.*, vol. 62, no. 12, pp. 6081–6090, 2014.

[34] ——, "Nonlinear effects of non-foster matching networks," in *Proc. IEEE Int. Symp. Antennas Propag. Soc. (APSURSI).* Vancouver, Canada: IEEE, Jul. 2015.

[35] C. R. White, "A non-foster monopole array," in *Proc. IEEE Int. Symp. Antennas Propag. Soc. (APSURSI).* Chicago, IL: IEEE, Jul. 2012.

[36] J. Li, M. Parlak, H. Mukai, M. Matsuo, and J. F. Buckwalter, "A reconfigurable 50-mb/s-1 gb/s pulse compression radar signal processor with offset calibration in 90-nm cmos," *IEEE Trans. Microw. Theory Techn.*, vol. 63, no. 1, pp. 266–278, 2015.

[37] J. Long, M. Jacob, and D. Sievenpiper, "Broadband fast-wave propagation in a non-foster circuit loaded waveguide," *IEEE Trans. Microw. Theory Techn.*, vol. 62, no. 4, pp. 789–798, April 2014.

[38] J. Long and D. F. Sievenpiper, "Dispersion-reduced high impedance surface loaded with non-foster impedances," in *Proc. IEEE Int. Symp. Antennas Propag. Soc. (APSURSI)*, Vacouver, Canada, Jul. 2015.

[39] S. Galal and B. Razavi, "10-gb/s limiting amplifier and laser/modulator driver in 0.18-μm cmos technology," *IEEE J. Solid-State Circuits*, vol. 38, no. 12, pp. 2138–2146, 2003.

[40] A. P. Jose and K. L. Shepard, "Distributed loss-compensation techniques for energy-efficient low-latency on-chip communication," *IEEE J. Solid-State Circuits*, vol. 42, no. 6, pp. 1415–1424, 2007.

[41] J. Li, G. Li, X. Zheng, K. Raj, A. V. Krishnamoorthy, and J. F. Buckwalter, "A 25-gb/s monolithic optical transmitter with micro-ring modulator in 130-nm soi cmos," *IEEE Photon. Technol. Lett.*, vol. 25, no. 19, pp. 1901–1903, 2013.

[42] J. T. Aberle and R. Loepsinger-Romak, *Antennas with non-Foster matching networks*.   San Rafael, CA: Morgan & Claypool Publishers, 2007.

[43] J. Linvill, "Transistor negative-impedance converters," *Proc. IRE*, vol. 6, no. 41, pp. 725–729, 1953.

[44] J. Brownlie, "On the stability properties of a negative impedance converter," *IEEE Trans. Circuit Theory*, vol. 13, no. 1, pp. 98–99, 1966.

[45] A. Larky, "Negative-impedance converters," *Proc. IRE*, pp. 124–132, 1957.

[46] T. Yanagisawa, "Rc active networks using current inversion type negative impedance converters," *IRE Trans. Circuit Theory*, vol. 4, no. 3, pp. 140–144, 1957.

[47] H. Yogo and K. Kato, "Circuit realisation of negative-impedance convertor at vhf," *Electronics Lett.*, vol. 10, no. 9, pp. 155–156, 1974.

[48] R. Brennan, T. Viswanathan, and J. Hanson, "The cmos negative impedance converter," *IEEE J. Solid-State Circuits*, vol. 23, no. 5, pp. 1272–1275, 1988.

[49] S. G. El Khoury, "New approach to the design of active floating inductors in mmic technology," *IEEE Trans Microw. Theory Techn.*, vol. 44, no. 4, pp. 505–512, 1996.

[50] J. Li, N. Xu, Y. Sun, W. Rhee, and Z. Wang, "A 6.5 mw, wide band dual-path lc vco design with mode switching technique in 130nm cmos," in *IEEE Topical Meeting Silicon Monolithic Integrated Circuits in RF Syst. (SiRF)*.   IEEE, 2015, pp. 7–10.

[51] Z. Zhang, J. Li, Y. Sun, W. Rhee, and Z. Wang, "A digitally reconfigurable auto amplitude calibration method for wide tuning range vco design," in *IEEE Int. Conf. Solid-State and Integrated Circuit Technology (ICSICT)*.   IEEE, 2010, pp. 542–544.

[52] R. He, J. Li, W. Rhee, and Z. Wang, "Transient analysis of nonlinear settling behavior in charge-pump phase-locked loop design," in *IEEE Int. Symp. Circuits and Syst. (ISCAS)*.   IEEE, 2009, pp. 469–472.

[53] A. Davies, "Stability properties of a negative immittance converter," p. 80, 1968.

[54] H. Nyquist, "Regeneration theory," *Bell System Technical Journal*, vol. 11, no. 1, pp. 126–147, 1932.

[55] D. F. Sievenpiper, "Superluminal waveguides based on non-foster circuits for broadband leaky-wave antennas," *IEEE Antennas Wireless Propag. Lett.*, vol. 10, pp. 231–234, 2011.

[56] W. Menzel, "A new travelling wave antenna in microstrip," *Arch. Elektron. Uebertrag. Techn.*, vol. 33, no. 4, pp. 137–140, Apr. 1979.

[57] A. Grbic and G. V. Eleftheriades, "Leaky cpw-based slot antenna arrays for millimeter-wave applications," *IEEE Trans. Antennas Propag.*, vol. 50, pp. 1494–1504, Nov. 2002.

[58] S. Lim, C. Caloz, and T. Itoh, "Metamaterial-based electronically controlled transmission-line structure as a novel leaky-wave antenna with tunable radiation angle and beamwidth," *IEEE Trans. Microw. Theory Techn.*, vol. 53, no. 1, pp. 161–173, Jan. 2005.

[59] B. Kanté, D. Germain, and A. de Lustrac, "Experimental demonstration of a nonmagnetic metamaterial cloak at microwave frequencies," *Phys. Rev. B*, vol. 80, no. 20, p. 201104, Nov. 2009.

[60] B. Edwards, A. Alù, M. E. Young, M. Silveirinha, and N. Engheta, "Experimental verification of epsilon-near-zero metamaterial coupling and energy squeezing using a microwave waveguide," *Phys. Rev. Lett.*, vol. 100, p. 033903, Jan. 2008.

[61] S. Hrabar, I. Krois, I. Bonic, and A. Kiricenko, "Negative capacitor paves the way to ultra-broadband metamaterials," *Appl. Phys. Lett.*, vol. 99, no. 25, p. 254103, Dec. 2011.

[62] ——, "Ultra-broadband simultaneous superluminal phase and group velocities in non-foster epsilon-near-zero metamaterial," *Appl. phys. lett.*, vol. 102, no. 5, p. 054108, 2013.

[63] J.-S. Hong and M. J. Lancaster, *Microstrip filters for RF/microwave applications*. New York: Wiley, 2001.

[64] C. R. White, J. W. May, and J. S. Colburn, "A variable negative-inductance integrated circuit at uhf frequencies," *IEEE Microw. Wireless Compon. Lett.*, vol. 22, no. 1, pp. 35–37, Jan. 2012.

[65] N. Zhu and R. W. Ziolkowski, "Active metamaterial-inspired broad-bandwidth, efficient, electrically small antennas," *IEEE Antennas Wireless Propag. Lett., IEEE*, vol. 10, pp. 1582–1585, 2011.

[66] [Online]. Available: http://www.modelithics.com/

[67] M. Tian, V. Visvanathan, J. Hantgan, and K. Kundert, "Striving for small-signal stability," *IEEE Circuits Devices Mag.*, vol. 17, no. 1, pp. 31–41, Jan. 2001.

[68] R. D. Middlebrook, "Null double injection and the extra element theorem," *IEEE Trans. Educ.*, vol. 32, no. 3, pp. 167–180, Aug. 1989.

[69] S. D. Stearns, "Non-foster circuits and stability theory," in *Proc. IEEE Int. Symp. Antennas Propag. Soc. (APSURSI)*, Spokane, WA, Jul. 2011, pp. 1942–1945.

[70] ——, "Incorrect stability criteria for non-foster circuits," in *Proc. IEEE Int. Symp. Antennas Propag. Soc. (APSURSI)*, Chicago, IL, Jul. 2012.

[71] E. Ugarte-Munoz, S. Hrabar, D. Segovia-Vargas, and A. Kiricenko, "Stability of non-foster reactive elements for use in active metamaterials and antennas," *IEEE Trans. Antennas Propag.*, vol. 60, no. 7, pp. 3490–3494, Jul. 2012.

[72] X. D. Chen, T. M. Grzegorczyk, B. I. Wu, J. Pacheco, and J. A. Kong, "Robust method to retrieve the constitutive effective parameters of metamaterials," *Phys. Rev. E*, vol. 70, no. 1, Jul 2004.

[73] W. Withayachumnankul, B. M. Fischer, B. Ferguson, B. R. Davis, and D. Abbott, "A systemized view of superluminal wave propagation," *Proc. IEEE*, vol. 98, no. 10, pp. 1775–1786, 2010.

[74] J. Bechhoefer, "Kramers–kronig, bode, and the meaning of zero," *Amer. J. Phys.*, vol. 79, no. 10, pp. 1053–1059, 2011.

[75] D. Sievenpiper, M. Jacob, and J. Long, "Active electromagnetic structures, metamaterials, and antennas," in *IEEE Int. Workshop Antenna Techn. (iWAT)*.   IEEE, 2012, pp. 289–292.

[76] H. Mirzaei and G. V. Eleftheriades, "An active artificial transmission line for squint-free series-fed antenna array applications," in *Proc. European Microw. Conf. (EuMC)*.   IEEE, 2011, pp. 503–506.

[77] H. Mirzaei and G. Eleftheriades, "Arbitrary-angle squint-free beamforming in series-fed antenna arrays using non-foster elements synthesized by negative-group-delay networks," *IEEE Trans. Antennas Propag.*, vol. 63, no. 5, pp. 1997–2010, May 2015.

[78] P.-Y. Chen, C. Argyropoulos, and A. Alù, "Broadening the cloaking bandwidth with non-foster metasurfaces," *Phys. Rev. Lett.*, vol. 111, no. 23, p. 233001, 2013.

[79] J. Long and D. F. Sievenpiper, "Stable multiple non-foster circuits loaded waveguide for broadband non-dispersive fast-wave propagation," *Electron. Lett.*, vol. 50, no. 23, pp. 1708–1710, 2014.

[80] S. R. Rengarajan and C. R. White, "Stability analysis of superluminal waveguides periodically loaded with non-foster circuits," *IEEE Antennas Wireless Propag. Lett.*, vol. 12, pp. 1303–1306, 2013.

[81] L. Zhang, L. Zhan, K. Qian, J. Liu, Q. Shen, X. Hu, and S. Luo, "Superluminal propagation at negative group velocity in optical fibers based on brillouin lasing oscillation," *Phys. Rev. Lett.*, vol. 107, p. 093903, Aug 2011.

[82] R. Y. Chiao, "Tunneling times and superluminality: A tutorial," *arXiv preprint quant-ph/9811019*, 1998.

[83] U. Leonhardt, "Optical conformal mapping," *Science*, vol. 312, no. 5781, pp. 1777–1780, 2006.

[84] A. M. Steinberg, P. G. Kwiat, and R. Y. Chiao, "Measurement of the single-photon tunneling time," *Phys. Rev. Lett.*, vol. 71, pp. 708–711, Aug 1993.

[85] M. D. Stenner, D. J. Gauthier, and M. A. Neifeld, "The speed of information in a fast-lightoptical medium," *Nature*, vol. 425, no. 6959, pp. 695–698, 2003.

[86] R. W. Ziolkowski, "Superluminal transmission of information through an electromagnetic metamaterial," *Phys. Rev. E*, vol. 63, no. 4, p. 046604, 2001.

[87] C. G. B. Garrett and D. E. McCumber, "Propagation of a gaussian light pulse through an anomalous dispersion medium," *Phys. Rev. A*, vol. 1, pp. 305–313, Feb 1970.

[88] L. Brillouin, *Wave propagation and group velocity*. New York: Academic Press, 1960.

[89] L. J. Wang, A. Kuzmich, and A. Dogariu, "Gain-assisted superluminal light propagation," *Nature*, vol. 406, no. 6793, pp. 277–279, 2000.

[90] A. M. Steinberg and R. Y. Chiao, "Dispersionless, highly superluminal propagation in a medium with a gain doublet," *Phys. Rev. A*, vol. 49, pp. 2071–2075, Mar 1994.

[91] S. Longhi, M. Marano, P. Laporta, and M. Belmonte, "Superluminal optical pulse propagation at 1.5μm in periodic fiber bragg gratings," *Phys. Rev. E*, vol. 64, p. 055602, Oct 2001.

[92] G. M. Gehring, A. Schweinsberg, C. Barsi, N. Kostinski, and R. W. Boyd, "Observation of backward pulse propagation through a medium with a negative group velocity," *Science*, vol. 312, no. 5775, pp. 895–897, 2006.

[93] G. Dolling, C. Enkrich, M. Wegener, C. M. Soukoulis, and S. Linden, "Simultaneous negative phase and group velocity of light in a metamaterial," *Science*, vol. 312, no. 5775, pp. 892–894, 2006.

[94] D. Ye, Y. Salamin, J. Huangfu, S. Qiao, G. Zheng, and L. Ran, "Observation of wave packet distortion during a negative-group-velocity transmission," *Scientific Reports*, vol. 5, 2015.

[95] F. W. King, *Hilbert transforms*. Cambridge University Press Cambridge, UK, 2009, vol. 2.

[96] D. Sievenpiper, L. Zhang, R. F. J. Broas, N. G. Alexopolous, and E. Yablonovitch, "High-impedance electromagnetic surfaces with a forbidden frequency band," *IEEE Trans. Microw. Theory Techn.*, vol. 47, no. 11, pp. 2059–2074, 1999.

[97] R. G. Quarfoth and D. F. Sievenpiper, "Nonscattering waveguides based on tensor impedance surfaces," *IEEE Trans. Antennas Propag.*, vol. 63, no. 4, pp. 1746–1755, 2015.

[98] R. Quarfoth and D. Sievenpiper, "Surface wave scattering reduction using beam shifters," *IEEE Antennas Wireless Propag. Lett.*, vol. 13, pp. 963–966, 2014.

[99] Z. Luo, X. Chen, J. Long, R. Quarfoth, and D. Sievenpiper, "Self-focusing of electromagnetic surface waves on a nonlinear impedance surface," *Applied Physics Letters*, vol. 106, no. 21, p. 211102, 2015.

[100] D. Sievenpiper, J. Schaffner, R. Loo, G. Tangonan, S. Ontiveros, and R. Harold, "A tunable impedance surface performing as a reconfigurable beam steering reflector," *IEEE Trans. Antennas Propag.*, vol. 50, no. 3, pp. 384–390, 2002.

[101] S.-C. Chen, Y.-S. Wang, and S.-J. Chung, "A decoupling technique for increasing the port isolation between two strongly coupled antennas," *IEEE Trans. Antennas Propag.*, vol. 56, no. 12, pp. 3650–3658, 2008.

[102] Z. Luo, X. Chen, J. Long, R. Quarfoth, and D. Sievenpiper, "Nonlinear power-dependent impedance surface," *IEEE Trans. Antennas Propag.*, vol. 63, no. 4, pp. 1736–1745, 2015.

[103] F. Costa, S. Genovesi, and A. Monorchio, "On the bandwidth of high-impedance frequency selective surfaces," *IEEE Antennas Wireless Propag. Lett.*, vol. 8, pp. 1341–1344, 2009.

[104] F. Costa, A. Monorchio, and G. Manara, "Analysis and design of ultra thin electromagnetic absorbers comprising resistively loaded high impedance surfaces," *IEEE Trans. Antennas Propag.*, vol. 58, no. 5, pp. 1551–1558, 2010.

[105] H.-J. Lee, K. L. Ford, and R. J. Langley, "Independently tunable low-profile dual-band high-impedance surface antenna system for applications in uhf band," *IEEE Trans. Antennas Propag.*, vol. 60, no. 9, pp. 4092–4101, 2012.

[106] C. Mias and J. H. Yap, "A varactor-tunable high impedance surface with a resistive-lumped-element biasing grid," *IEEE Trans. Antennas Propag.*, vol. 55, no. 7, pp. 1955–1962, 2007.

[107] D. J. Gregoire, C. R. White, and J. S. Colburn, "Wideband artificial magnetic conductors loaded with non-foster negative inductors," *IEEE Antennas Wireless Propag. Lett.*, vol. 10, pp. 1586–1589, 2011.

[108] M. Barbuto, A. Monti, F. Bilotti, and A. Toscano, "Design of a non-foster actively loaded srr and application in metamaterial-inspired components," *IEEE Trans. Antennas Propag.*, vol. 61, no. 3, pp. 1219–1227, 2013.

[109] F. Gao, F. Zhang, J. Long, M. Jacob, and D. Sievenpiper, "Non-dispersive tunable reflection phase shifter based on non-foster circuits," *Electron. Lett.*, vol. 50, no. 22, pp. 1616–1618, 2014.